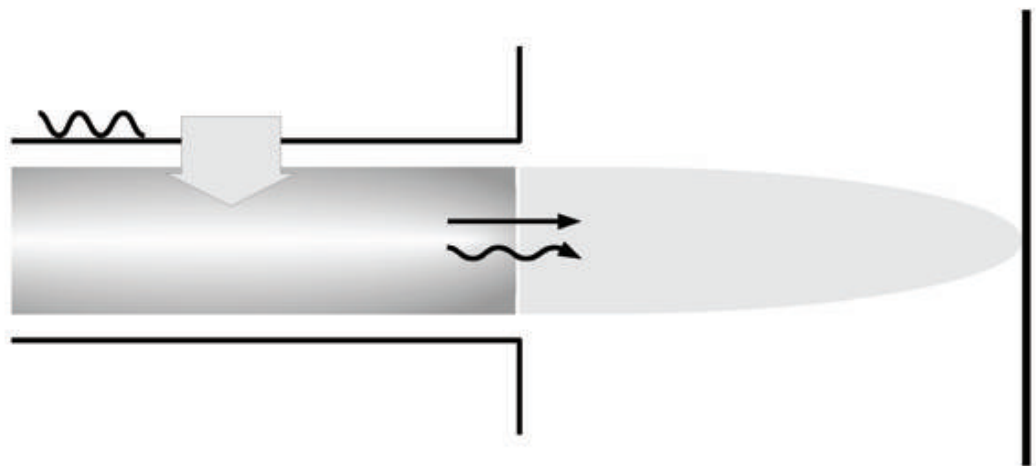


Formation Mechanisms of Atomic Oxygen in an Atmospheric Pressure Plasma Jet Characterised by Spectroscopic Methods



Formation Mechanisms of Atomic Oxygen in an Atmospheric Pressure Plasma Jet Characterised by Spectroscopic Methods

Inauguraldissertation

zur Erlangung des akademischen Grades

doctor rerum naturalium (Dr. rer. nat.)

vorgelegt dem Fachbereich Physik der Universität Duisburg-Essen

von

Stephan Reuter

geboren am 2. Oktober 1974

in Essen

Tag der Einreichung: 19. September 2007

Erster Gutachter: Prof. Dr. Hans-Friedrich Döbele

Zweiter Gutachter: Prof. Dr. Volker Buck

Prüfungsvorsitzender: Prof. Dr. Lothar Schäfer

Tag der Disputation: 31. Oktober 2007

Die vorliegende Arbeit entstand während meiner Tätigkeit als wissenschaftlicher Mitarbeiter der Arbeitsgruppe von Prof. Dr. H. F. Döbele am Institut für Laser- und Plasmaphysik der Universität Duisburg-Essen im Projekt „Verbund plasmagestützte Oberflächenmodifikation von medizin- und biotechnischer Bedeutung“, gefördert durch das Ministerium für Wissenschaft und Forschung NRW.

Bibliografische Information der Deutschen Nationalbibliothek

Die Deutsche Nationalbibliothek verzeichnet diese Publikation in der Deutschen Nationalbibliografie; detaillierte bibliografische Daten sind im Internet über <http://dnb.ddb.de> abrufbar.

1. Aufl. - Göttingen : Cuvillier, 2008

Zugl.: Duisburg-Essen, Univ., Diss., 2007

978-3-86727-539-2

© CUVILLIER VERLAG, Göttingen 2008

Nonnenstieg 8, 37075 Göttingen

Telefon: 0551-54724-0

Telefax: 0551-54724-21

www.cuvillier.de

Alle Rechte vorbehalten. Ohne ausdrückliche Genehmigung des Verlages ist es nicht gestattet, das Buch oder Teile daraus auf fotomechanischem Weg (Fotokopie, Mikrokopie) zu vervielfältigen.

1. Auflage, 2008

Gedruckt auf säurefreiem Papier

978-3-86727-539-2

Contents

1	Introduction	5
1.1	Plasma	5
1.2	Glow Discharges	6
1.2.1	Instabilities	8
1.3	Low Temperature Atmospheric Pressure Glow Plasmas	9
1.3.1	Common Plasma Sources in Comparison	10
2	Optical Plasma Diagnostics Applied in this Work	15
2.1	Optical Emission Spectroscopy (OES)	16
2.1.1	Atomic and Molecular Spectra	16
2.1.2	Excitation and De-Excitation Mechanisms	18
2.1.3	OES-Measurement Setup	19
2.2	Absorption Spectroscopy	20
2.3	Laser Induced Fluorescence Spectroscopy (LIF/ TALIF)	22
2.3.1	Two-Photon Excitation	24
2.3.2	TALIF Rate Equation Model	25
3	The Atmospheric Pressure Plasma Jet (APPJ)	31
3.1	Setup of the APPJ	31
3.1.1	Concentric APPJ	31
3.1.2	Planar APPJ	34
3.2	Working Principle of the APPJ	35
3.2.1	Discharge Region and Effluent	36
3.3	Characterisation of the Discharge Region	37
3.3.1	Current and Voltage Measurement Setup	37
3.3.2	Discharge Operation Modes (α - and γ -Mode)	38
3.3.3	Discharge of Planar APPJ versus Concentric APPJ	40
3.3.4	Operation in Helium and in Argon	40
3.3.5	Pulsed Operation Mode	46
3.4	Characterisation of the Effluent	47
3.4.1	Effluent of Planar APPJ versus Concentric APPJ	47
3.4.2	OES of the Effluent	49

4	Oxygen Radical Formation Processes in the APPJ's Effluent	51
4.1	Atomic Oxygen Ground State Density in the Effluent	52
4.1.1	Experimental Setup for Two-Photon Absorption Laser Induced Fluorescence (TALIF) Spectroscopy	52
4.1.2	TALIF-Calibration with Xenon	55
4.1.3	Atomic Oxygen Density Map of the Effluent	64
4.2	Energy Transport into the Effluent	66
4.2.1	Possible Energy Transport Mechanisms	66
4.2.2	(V)UV-Radiation	67
4.3	Oxygen Radical Chemistry in the Effluent	70
4.3.1	Chemical Kinetics Modelling	70
4.3.2	Adaption and Modification of the Model	72
4.3.3	Ozone and $O_2(b^1\Sigma_g^+)$ -Density Measurements in the Effluent .	78
4.3.4	Comparison of Measured Oxygen Radical Densities with Chemi- cal Model Calculations	82
4.3.5	Atomic Oxygen Production by (V)UV-Radiation	84
4.4	An Outlook to the μ -APPJ	86
4.5	Conclusion	87
5	Oxygen Radical Interaction Processes in APPJ Surface Treatment	89
5.1	Preliminary Investigations on Silicon Oxidation	90
5.2	Surface Functionalisation of Polymers	91
5.2.1	Hydrophilisation and Contact Angle Measurements	92
5.2.2	Experimental Setup for Polymer Treatment	94
5.2.3	Parameter Study on Hydrophilisation of Polystyrene Petri Dishes	96
5.3	Conclusion	111
6	Improving the APPJ's Atomic Oxygen Output	113
6.1	Atomic Oxygen Generation in the Plasma	113
6.1.1	Influence of the Electrode Surface Material	114
6.2	The Dielectric Barrier APPJ	115
6.2.1	Electrode Modification	116
6.2.2	Discharge Characteristics	117
6.2.3	Phase and Space Resolved Emission Imaging	118
6.2.4	Atomic Oxygen Production Efficiency	122
6.3	Conclusion	122
7	Conclusion and Outlook	123
	Bibliography	131

Kurzfassung

In dieser Arbeit wird ein 13,56 MHz RF-angeregter Atmosphärendruck Plasmajet (APPJ) untersucht. Der APPJ kann an Luft betrieben werden, mit Helium oder Argon als Arbeitsgas mit einer molekularen Beimischung (hier Sauerstoff) von bis zu einigen vol%. In der Entladungsregion zwischen den Elektroden wird eine homogene Glimmentladung erzeugt. Der Effluent, gebildet durch das aus der Entladung strömende Gas, hat eine Länge von einigen Zentimetern und eine Gastemperatur von weit unter 100°C. Im Wesentlichen besteht der Effluent aus Edelgasatomen und reaktiven Sauerstoffradikalen. Er enthält nur wenige bis gar keine geladenen Teilchen. Durch die hohe Sauerstoffradikalkonzentration bei gleichzeitig niedriger Gastemperatur ist der APPJ hervorragend für die Behandlung empfindlicher Oberflächen geeignet.

Für die Charakterisierung der im Effluent und in der Entladung ablaufenden Prozesse ist der ursprünglich konzentrische Aufbau des Jets für diese Arbeit einem planaren Aufbau gewichen, der einen optischen Zugriff auf die Entladungsregion erlaubt. Die Grundzustandsdichte atomaren Sauerstoffs im Effluent des planaren APPJ wird hier erstmals direkt mit Zweiphotonen laserinduzierter Fluoreszenzspektroskopie (TALIF) gemessen. Dabei zeigt sich, dass die atomare Sauerstoffdichte unmittelbar an der Düse einen Wert von 10^{16} cm^{-3} erreicht. Sogar in einem Abstand von einigen Zentimetern ist noch etwa 1 % der anfänglichen Sauerstoffdichte vorhanden.

Optische Emissionsspektroskopie (OES) bis zu einer Wellenlänge von 110 nm wird als weiteres diagnostisches Verfahren eingesetzt. Die Spektren zeigen Emissionslinien vom sichtbaren bis in den vakuumultravioletten (VUV) Spektralbereich (etwa von atomarem Sauerstoff bei $\sim 130 \text{ nm}$), die bis weit im Effluent nachweisbar sind. OES im sichtbaren Wellenlängenbereich weist angeregte Sauerstoffatome in einigen Zentimetern Entfernung von der Düse nach. Die Ursache für das bislang ungeklärte Vorkommen dieser extrem kurzlebigen Spezies im Effluent gilt es zu untersuchen.

Für ein besseres Verständnis der grundlegenden Mechanismen der Produktion und Vernichtung atomaren Sauerstoffs im Effluent, und um Erkenntnisse zu gewin-

nen über den Energietransport aus der Entladung in den Effluent, verantwortlich für die Erzeugung angeregter Sauerstoffatome weit entfernt von der Düse, werden die gemessenen Sauerstoffradikaldichten (O , O_3 , $\text{O}_2(\text{b}^1\Sigma_g^+)$) mit reaktionskinetischen Modellrechnungen verglichen. Die atomare Sauerstoffdichte ist tatsächlich höher als sich aus den Modellrechnungen ergibt. (V)UV-Emissionsspektroskopie und atomare Sauerstoffdichtemessungen mittels TALIF zeigen, dass (V)UV-Strahlung aus dem Plasma des APPJ atomaren Sauerstoff außerhalb der Entladungsregion erzeugt und somit eine Erklärung für die erhöhte atomare Sauerstoffdichte im Effluent bietet. Durch (V)UV-Photodissoziation von metastabilem molekularem $\text{O}_2(\text{a}^1\Delta_g)$, welches auch in größerer Entfernung von der Düse noch vorhanden ist, ist die Produktion von angeregtem atomaren Sauerstoff zu erklären.

Darüber hinaus wird die Wechselwirkung der reaktiven Sauerstoffradikale im APPJ-Effluent mit Oberflächen untersucht. Dabei wird die Hydrophilisierung von Polymeren durch Plasmabehandlung mit dem APPJ im Detail betrachtet. Die Benetzbarkeit der Oberflächen – bestimmt mittels Kontaktwinkelmessungen an Wasser – wird dazu mit den gemessenen Sauerstoffradikaldichten korreliert. Die Studie zeigt, dass sowohl atomarer Sauerstoff als auch metastabiler molekularer Sauerstoff einen wesentlichen Einfluss auf die Oberflächenfunktionalisierung von Polystyrol haben.

Die gewonnenen Erkenntnisse führen schließlich zu einer Modifikation des APPJ, durch welche die Effizienz der Produktion atomaren Sauerstoffs deutlich gesteigert wird: Um Verluste atomaren Sauerstoffs durch Rekombination an den Metalloberflächen der Elektroden zu vermindern, werden die Elektrodenoberflächen mit einer dünnen dielektrischen Barrierschicht (DB) aus SiO_2 versehen. Untersuchungen zeigen, dass dieser, hier DB-APPJ genannte, Jet dieselbe homogene Glimmentladung erzeugt wie der reguläre APPJ. Insbesondere in Hinsicht auf zukünftige Anwendungen stellt die Effizienzsteigerung der Produktion atomaren Sauerstoffs im modifizierten APPJ eine entscheidende Verbesserung dar.

Abstract

In this work a 13.56 MHz RF-excited atmospheric pressure plasma jet (APPJ) is diagnosed. The APPJ operates at ambient conditions with a feed gas of helium or argon and admixtures (about 1 vol%) of molecular gases, here oxygen. A homogeneous glow discharge is generated in the discharge region between the electrodes. The effluent leaving the discharge through the jet's nozzle extends several centimetres outside the jet with a temperature well below 100°C. The effluent contains mostly noble gas atoms and reactive oxygen radicals and few to no charged species. Its high oxygen radical output together with its low temperature makes the APPJ an excellent plasma tool for treatment of sensitive surfaces.

For a characterisation of the processes occurring in discharge and effluent of the APPJ, the originally concentric version of the jet in this work gives way to a planar setup, which allows optical diagnostics also of the discharge region. The ground state atomic oxygen density in the planar APPJ's effluent is for the first time measured space resolved with two-photon absorption laser induced fluorescence (TALIF) spectroscopy. The atomic oxygen density close to the nozzle reaches a value of 10^{16} cm^{-3} . Even at several centimetres distance still 1% of the initial atomic oxygen density can be detected. Optical emission spectroscopy (OES) down to 110 nm is carried out in free air. These spectra demonstrate vacuum ultraviolet (VUV) emission lines e.g. of oxygen at $\sim 130 \text{ nm}$, reaching far into the effluent. OES in the visible range performed perpendicular to the effluent unexpectedly reveals presence of excited oxygen atoms at several centimetres distance from the jet's nozzle, making further investigations of the origin of these short living excited atomic oxygen states necessary.

For better understanding the underlying mechanisms of atomic oxygen production and annihilation in the effluent as well as the energy transport from the discharge region into the effluent, responsible for generation of excited atomic oxygen far away from the jet's nozzle, the measured oxygen radical densities (O , O_3 , $\text{O}_2(\text{b}^1\Sigma_g^+)$) are compared with chemical model calculations. The actual atomic oxygen density is

higher than predicted by modelling. (V)UV-emission spectroscopy and O-density measurements reveal that (V)UV-radiation from the APPJ's core plasma generates atomic oxygen outside the discharge region, thus giving an explanation for the high atomic oxygen density in the effluent. (V)UV-photodissociation of singlet metastable molecular oxygen $O_2(a^1\Delta_g)$ – still present at several centimetres distance from the jet's nozzle – can produce the excited atomic oxygen found in the effluent.

In order to analyse the interaction processes of the APPJ's effluent with surfaces, a pilot study of surface treatment applications is performed, concentrating on hydrophilisation of polymers. The polymer's wettability – determined by water contact angle measurements – is correlated with the oxygen radical densities measured in the effluent. The study shows that both atomic oxygen and metastable molecular oxygen play a vital role in polystyrene surface functionalisation.

The acquired knowledge is applied to enhance the jet's atomic oxygen generation efficiency. In order to reduce the loss of atomic oxygen due to interactions with the electrodes' metal surfaces, the electrodes are coated with a thin quartz layer, constituting a dielectric barrier (DB). Investigations show that this here called DB-APPJ exhibits the same homogeneous glow discharge as the regular APPJ. The resulting increase of the modified jet's atomic oxygen output is considered to be of major importance for possible applications of the APPJ in the future.

Chapter 1

Introduction

This chapter introduces glow discharges as an important section of plasma physics, with the focus set on plasma at atmospheric pressure. The conditions under which a glow discharge at atmospheric pressure can be obtained are described, taking into account instability issues. A brief depiction of comparable low temperature atmospheric pressure glow discharge plasma sources will help to categorise the plasma source investigated in this work.

1.1 Plasma

Plasma is frequently referred to as the fourth state of matter. In nature, plasmas are perceptible for example as lightning, as aurora borealis, as the sun's fusion plasma, and also as astronomical plasmas. A precise definition goes beyond the mere statement that a plasma consists of charged particles: A plasma is a quasi neutral gas of charged and neutral particles which exhibit collective behaviour [Chen74].

Man-made plasmas play a role in material science, for pollution control, for decontamination and sterilisation, as well as in semiconductor and display technology, to name but a few key applications. Most plasma processes require low pressure for operation. Materials to be plasma treated are therefore placed in vacuum chambers. Loadlocks and robotic assemblies are needed in order to load and unload the material. The size of the objects to be processed is limited by the size of the vacuum chamber. The use of vacuum equipment is expensive and requires high maintenance. The desire to reduce costs and effort makes atmospheric pressure plasmas increasingly important in the growing field of plasma applications.

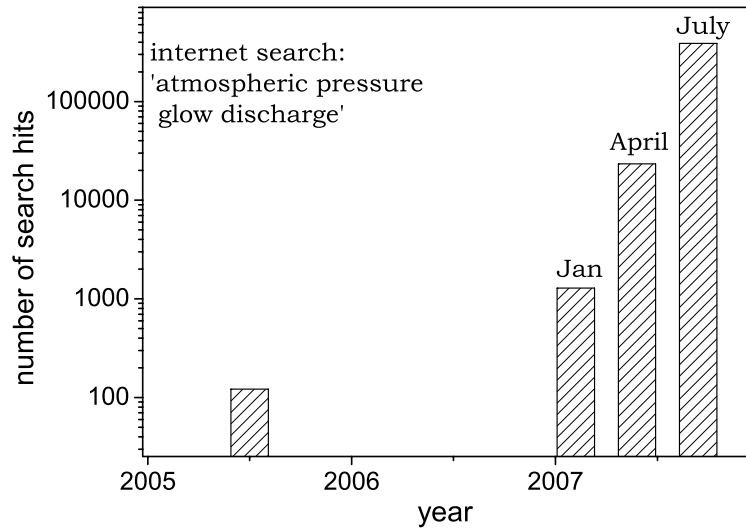


Figure 1.1: Internet search hits for ‘atmospheric pressure glow discharge’ (note the logarithmic y-axis)

Low temperature plasma sources operating at atmospheric pressure with a gas temperature only slightly higher than room temperature are sought after, especially for treatment of temperature sensitive surfaces such as e.g. polymers or skin. Discharges with these properties have been known for some decades now in form of dielectric barrier discharges (DBD). Dielectric barrier discharges, however, produce an inhomogeneous plasma bearing the risk of damaging the treated surface. Recent developments starting only about ten years ago provide new ways to create homogeneous low temperature atmospheric pressure glow discharges. An internet search of ‘atmospheric pressure glow discharge’ shows that the scientific interest in these glow discharges has grown rapidly (see figure 1.1¹).

In the following, the key properties of glow discharges are presented and the difficulties of producing low temperature glow discharges at atmospheric pressure are described. The most popular low temperature atmospheric pressure glow plasma sources are presented together with a brief explanation of their underlying principles.

1.2 Glow Discharges

A glow discharge can be obtained in a gas atmosphere by applying a voltage between two electrodes. Electrons emitted from the cathode are accelerated in the potential

¹The numbers represent no statistical survey, but rather a snapshot of the situation.

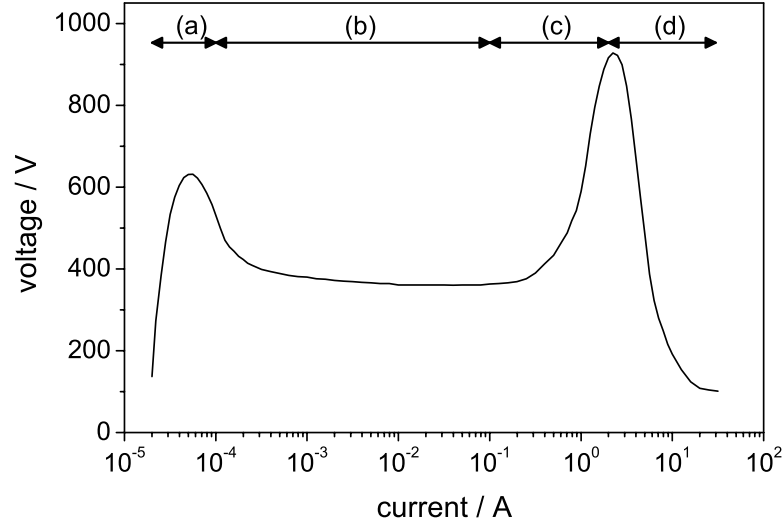


Figure 1.2: VI-characteristic of a DC-glow discharge [Francis56, Raizer01]: (a) Townsend discharge (b) normal glow discharge (c) abnormal glow discharge (d) transition to arc and arc discharge

drop at the cathode (cathode fall). The potential remains constant in the central region of the discharge gap where the electrons generate ions and excited species by collisions, thus producing the observable luminous glow. The second potential drop at the anode decelerates the electrons which subsequently get transferred to the outside electric circuit.

For the ignition of a direct current (DC) glow discharge, the electron impact ionisation and the secondary electron emission of the cathode are essential. In order to initiate a self-sustaining steady glow discharge, the following relation has to be fulfilled:

$$\gamma [e^{\alpha d} - 1] \geq 1 \quad (1.1)$$

α is the Townsend ionisation coefficient indicating the number of ionisation events per centimetre initiated by an electron along the electric field, d is the discharge gap, and γ is the effective secondary emission coefficient for the cathode. γ characterises the electron emission caused by particles that appear as a result of the primary process of electron impact ionisation [Raizer01].

Figure 1.2 presents an exemplary voltage/current (VI) characteristic of a DC-glow discharge with the designated regions (a) for Townsend discharge, (b) for normal glow discharge, (c) for abnormal glow discharge, and (d) for transition to arc and arc discharge. Adjustment of the current allows to control the regime in which the glow

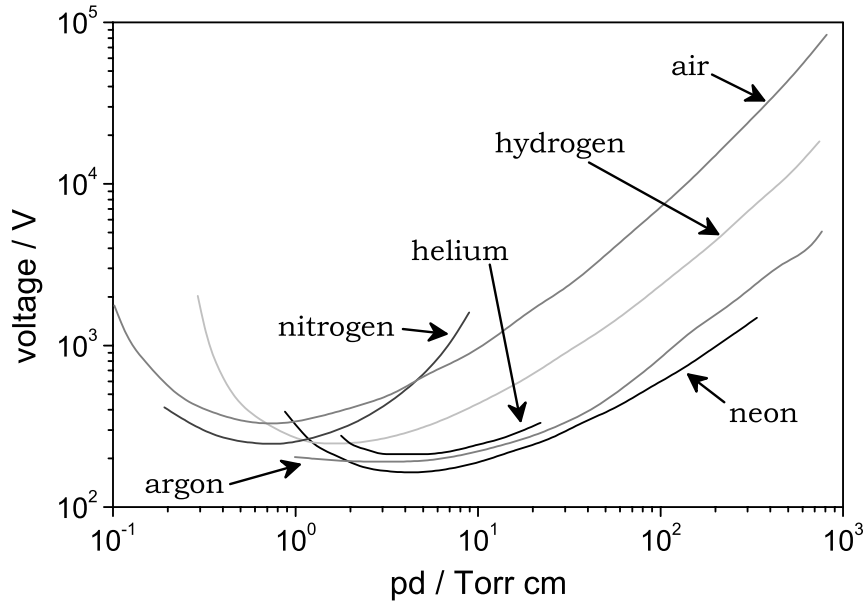


Figure 1.3: Breakdown potentials in various gases over a wide range of pd -values (Paschen curves) for iron as electrode material [Raizer01]

discharge is operated. To prevent arcing, the discharge current has to be limited. At the end of region (a) in figure 1.2 breakdown occurs and in case a strong enough current can be supplied, the discharge will proceed into the normal glow discharge regime. The voltage at which breakdown occurs for a particular gas and electrode material – influencing α and γ respectively – is a function of pressure (p) and distance between the electrodes (d), as shown in figure 1.3. The dependence of the breakdown voltage on the product of $p \cdot d$ is expressed in the Paschen law found in 1889.

A glow discharge can not only be produced by applying a direct current but also by applying radio frequency (RF) power. In an RF-glow discharge, the processes are more complex. The electrons are not travelling along a path, but oscillate in the RF-field, thus making it problematic to refer to α as number of ionisations per path. However, the fundamental processes of RF-glow discharges accord to the processes in DC-glow discharges. [Levitskii57]

1.2.1 Instabilities

Sustainment of a glow discharge is far from trivial. Several mechanisms can lead to instabilities which transfer the discharge from the glow regime to an arc. Thermal instability, for example, can be described as follows: A rising temperature T_G of the

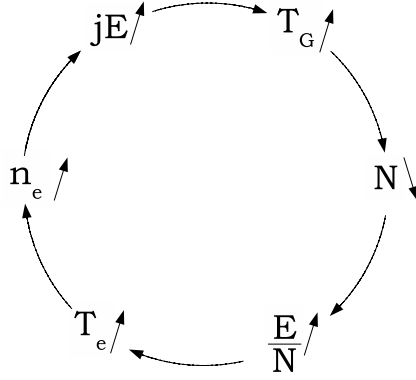


Figure 1.4: Schematic of thermal instability processes. The upward (downward) directed arrows symbolise an increase (decrease) in quantity.

discharge results in a decrease of particle density N , and thus in a rising ratio of $\frac{E}{N}$ at constant electric field E , which subsequently increases the electron temperature T_e . An increase of T_e results in an increased electron density n_e , and thus in an increased product of current density and electric field $j \cdot E$, which again leads to an increased gas temperature [Raizer01]. This vicious circle (see figure 1.4), can be counteracted by keeping the gas temperature constant. Apart from thermal instabilities, attachment instability, instability due to stepwise ionisation, and others can occur.

1.3 Low Temperature Atmospheric Pressure Glow Plasmas

As can be seen, for example, in arc welding, in high current arc electric switches, and in plasma torches for deposition or nanopowder generation, it is fairly simple to ignite a plasma at atmospheric pressure [Kogelschatz04]. These plasmas all operate close to local thermal equilibrium (LTE), where the electron temperature is the same as the ion and gas temperature of several thousand Kelvin.

In contrast to these plasmas in equilibrium, low temperature atmospheric pressure plasmas (e.g. glow discharges) operate far away from LTE, with the ion temperature and the electron temperature differing by orders of magnitude. The processes are driven by electrons, while the heavy particles remain at low temperature. Despite their low gas temperature, non-equilibrium plasmas show the same effective plasma chemistry as plasmas in equilibrium. The occurrence of instabilities, however, is

more likely so that non-equilibrium plasmas require a more sophisticated approach to achieve stable operation.

The probably first atmospheric pressure glow discharge was reported in 1915. W. Grotrian investigated the behaviour of a nitrogen DC-arc and found a parameter regime at which a normal glow discharge could be obtained [Grotrian15], p.155. In 1933, A. von Engel et al. specifically investigated atmospheric pressure glow discharges [Engel33]: To achieve an atmospheric pressure glow discharge, the plasma had to be initiated under vacuum conditions and subsequently the pressure had to be increased gradually to one atmosphere. Also, an excessive cooling of the cathode was required in order to suppress the glow to arc transition.

One of the first successful approaches in obtaining a low temperature atmospheric pressure glow discharge was the development of dielectric barrier discharges (DBD) (a review on the topic can be found in [Becker04]). The concept of dielectric barrier discharges is to obtain a quasi-glow discharge by placing one or several dielectrics between the electrodes, thus preventing the development of an arc. Steep flanked alternating current (AC) high voltage is applied and results in arbitrarily distributed streamer development. These streamers, however, only appear to be a homogeneous glow discharge. Time resolved observation identifies the discharge to consist of many single filaments. Further and more recent glow discharge concepts will be discussed in the following.

1.3.1 Common Plasma Sources in Comparison

The field of applications for low temperature atmospheric pressure glow discharges is continuously growing. In the medical sector, atmospheric pressure plasmas are used e.g. for treatment of tissue [Stoffels06], disinfection or coagulation of wounds [Raiser06] or treatment of dental caries [Sladek03]. Furthermore, atmospheric pressure plasmas are commonly used for surface treatment such as polymer treatment [Sarra-Bournet06, Bhoj05, Dockery07, Sira05, Strobel03], treatment of wood [Rehn03], surface functionalisation [Yonson06], as well as treatment of woven [Rombola06] and non woven fabrics [Roth01b]. Atmospheric pressure plasmas are also used as plasma actuators [Roth04] for the control of air flow in aeronautics [Moreau07]. In thin film technology, atmospheric pressure plasma sources are applied increasingly e.g. for thin film deposition [Paulussen05] or for generation of carbon nanotubes [Kuceroval06] in order to reduce high production costs due to expensive vacuum equipment.

1.3. LOW TEMPERATURE ATMOSPHERIC PRESSURE GLOW PLASMAS 11

Here (see the schematics in figure 1.5), a selection of atmospheric pressure plasma sources is presented, sharing the following essential characteristics:

- low temperature (from room temperature to $\sim 10^2$ °C)
- electron temperature capable of dissociating molecules (1-5 eV)
- high radical densities resulting in efficient plasma chemistry
- homogeneous glow discharge
- low breakdown voltage

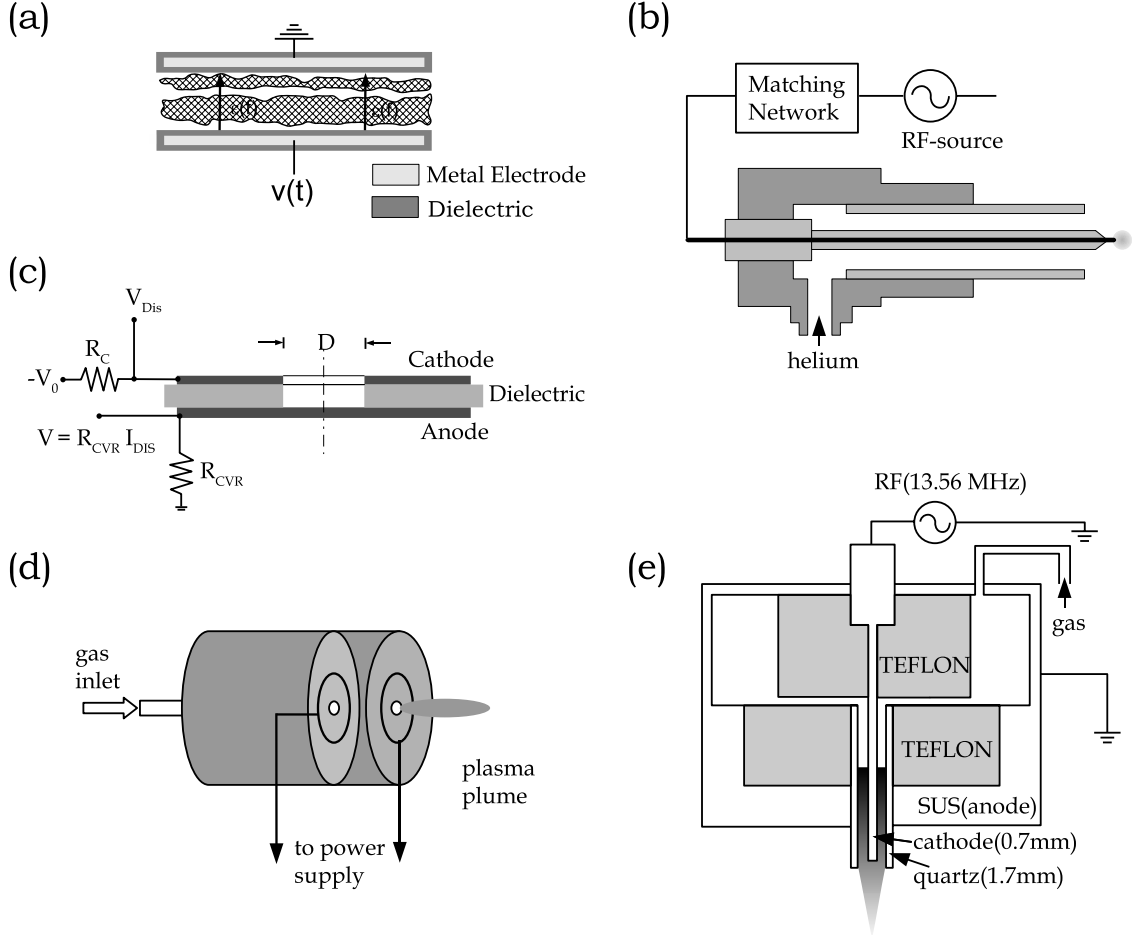


Figure 1.5: Low temperature atmospheric pressure glow discharges. (a) OUAPGDTM [Roth05], (b) plasma needle [Kieft04], (c) microhollow cathode [Schoenbach97], (d) plasma pencil [Laroussi05], (e) plasma torch [Koinuma92]

APGD/OAUGDP

The one atmosphere uniform glow discharge plasma (OAUGDPTM) was developed at the University of Tennessee in 1995 [Roth95]. It is basically a dielectric barrier discharge in setup and operating conditions, though J. Roth et al. operate it in a normal glow discharge mode in air. This discharge mode was achieved earlier by Massines et al. [Massines98b] and Kanazawa et al. [Kanazawa88] for helium, nitrogen and argon discharges with a dielectric, called atmospheric pressure glow discharges (APGD). Like all normal glow discharges, the OAUGDPTM operates at the so called Stoletow point, where the generation of an electron ion pair at one atmosphere is the most effective [Roth01a, Raizer01]. It operates at frequencies of 2 to 6 kHz and power densities of 6 to 80 mW/cm². For applications it can be used in direct mode, where the plasma is in contact with the samples [Roth05] or in remote mode, where the plasma is not in contact with the treated samples [Roth07].

Plasma Needle

The Plasma Needle is a small atmospheric pressure plasma device developed at the TU Eindhoven [Stoffels02], consisting of a quartz tube with a centered electrode. It is operated with 13.56 MHz radio frequency power and helium, argon, nitrogen or helium/air feed gas. The glow plasma is ignited at the tip of the electrode. The diameter of the plasma is in the submillimetre region. The discharge voltage is 200 to 500 V peak-to-peak. A remarkable property of the plasma needle is that its surroundings function as counter electrode. The size of the plasma ball forming around the tip of the RF-electrode is determined by the discharge power. At low and moderate power input the discharge is at room temperature plus $\sim 10^\circ\text{C}$. Due to its radical formation the plasma needle is well suited for treatment of living tissue and biomaterials. As a point source it is only applicable for local treatment and not suited for large area treatment.

Microhollow cathode discharge

The microhollow cathode discharge (MHCD) was investigated for the first time by White [White59] and rediscovered later by Schoenbach [Schoenbach97]. Microhollow cathodes avail the Paschen curve (see figure 1.3). Since the breakdown voltage of a glow discharge is proportional to pressure p times electrode distance or, in this case, cathode hole diameter d , the distance between the electrodes has to be sufficiently

small, in order to ignite a glow discharge at atmospheric pressure. The MHCD can be operated in three types of discharge: Up to pd -values of approximately 6 mbar cm, and at sub-mA currents, a glow discharge (predischARGE) is observed with a shape which is determined by the vacuum electric field. In the same pd -range, but at higher currents of up to approximately 4 mA, the discharge is of the hollow cathode discharge type. At pd -values exceeding 6 mbar cm, the predischARGE turns into a surface discharge along the dielectric between the electrodes [Schoenbach97].

The concept of using a discharge gap sufficiently small for sustaining a stable glow discharge is also applied in discharges with microstructured electrodes (see e.g. [Gericke02] or [Baars-Hibbe05]).

Plasma Pencil/Plasma Plume

The plasma pencil is a very recent development of Laroussi et al. at the University of Norfolk [Laroussi05]. Two electrodes, both made of a thin copper ring, are attached to the surface of a centrally perforated quartz disc. Both electrodes are inserted in a dielectric cylindrical tube of about the same diameter as the quartz discs and they are separated by a gap, the distance of which can be varied from 0.5 to 1 cm (see figure 1.5(d)). The operating gas consists of helium and is fed through a hole in the centre of the quartz disc through the two ring electrodes. The plasma source is operated by applying submicrosecond high voltage pulses at repetition rates in the 1 to 10 kHz range to the ring electrodes. Thus, the gas can be kept at room temperature while the energy introduced into the plasma can be raised considerably. Similar to the plasma needle, the plasma pencil can be used for localised surface treatment.

Cold Plasma Torch

The cold plasma torch as proposed by Koinuma already in 1992 [Koinuma92] is quite similar to the plasma needle. It consists of a steel needle to which a 13.56 MHz radio frequency is applied and which is centred in a quartz tube. In contrast to the plasma needle, the plasma torch's RF-electrode is centred in a ground reference electrode. The plasma torch is operated at 70 to 120 Watt and a feed gas flux of about 70 sccm. The operating gases are helium or argon with small molecular admixtures. The plasma beam has a length of 2 mm. In [Koinuma92], the plasma source is used e.g. for silicon etching.

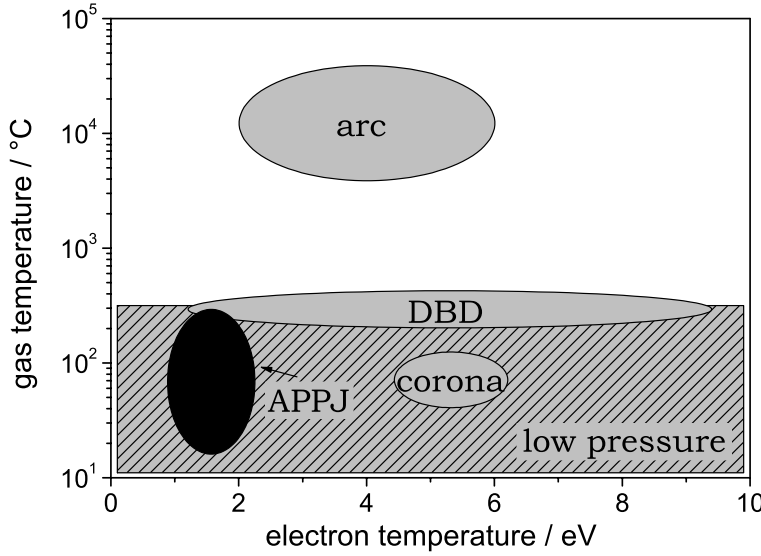


Figure 1.6: Gas temperature versus electron temperature for different discharges. [Schütze98]

APPJ

The atmospheric pressure plasma jet, developed in 1999 [Selwyn99], the plasma source investigated in the present work, has several advantages over other low temperature atmospheric pressure glow discharge sources. In figure 1.6, a comparison to other discharges plotting the gas temperature versus the electron temperature is presented. It can be seen that the APPJ reaches a regime typical for low pressure discharges. The APPJ can be used in a remote mode, so that the sample to be treated is not in contact to charged species, while radicals cause the desired surface chemistry [Babayan01a, Babayan01b, Hicks99]. The APPJ can be scaled up [Laimer05] for large area treatment, and it can be scaled down [Reuter07] for localised treatment. In contrast to, for example, the OAUGDPTM, the APPJ does not depend on a stationary setup and in addition to large area treatment, it is suitable also for hand-held operation. Like most low temperature atmospheric pressure glow discharge sources, the APPJ is operated with helium or argon feed gas with small molecular admixtures. A detailed description of the APPJ is presented in chapter 3.

Chapter 2

Optical Plasma Diagnostics Applied in this Work

To gain control over a plasma, an insight into its composition and its immanent processes is mandatory. Optical plasma diagnostic techniques have the advantage over other common plasma diagnostic methods that under optimum conditions the discharge remains undisturbed. In this chapter the optical plasma diagnostic methods applied in the present work are introduced and fundamentals and their underlying principles are briefly depicted, taking into account the circumstances of low temperature non equilibrium plasmas. Chapter 2.1 describes optical emission spectroscopy (OES). OES serves as a plasma diagnostic method to characterise the emitted plasma radiation and to determine the species present in discharge and effluent. In chapter 2.2 basics of absorption spectroscopy are presented. UV-absorption spectroscopy in the present work is applied to determine the ozone density in the plasma jet's effluent. Chapter 2.3 gives an overview on two-photon absorption laser induced fluorescence spectroscopy (TALIF). TALIF-spectroscopy represents the main diagnostic technique used throughout this work and is applied to determine atomic oxygen ground state densities. Since only a condensed presentation is possible, the following literature is suggested for further, more detailed study: A short introduction to the basics of OES is given in [Fantz06]. A detailed view on plasma spectroscopy can be found e.g. in [Döbele95], [Griem97], and [Demtröder04]. Common plasma diagnostic techniques are described in [Huddelstone65], [Lochte-Holtgreven68] and [Hutchinson87]. Elementary processes that determine the radiation of atoms and molecules in plasmas can be found e.g. in [Goldston95, Lieberman94].

2.1 Optical Emission Spectroscopy (OES)

Excited atoms and molecules emit light when an electronic transition from a higher state to a lower state of the energy levels of the atomic or molecular system occurs. The emission intensity of a spectral line is determined by the population of the respective levels and by their transition probabilities, stated by the Einstein coefficients. Optical emission spectroscopy (OES) yields information about excited species present in the plasma. In a low temperature non equilibrium plasma, the density of excited states typically lies five to six orders of magnitudes lower than the respective ground states. In order to gain quantitative results about the ground state densities, several techniques can be applied (e.g. actinometry [Francis97], [Lieberman94]). In most cases, a complex collision radiation model of approximative character – including all excitation and de-excitation channels – as well as a detailed knowledge of the electron energy distribution function is necessary, to evaluate the results of OES quantitatively.

2.1.1 Atomic and Molecular Spectra

For a correlation of optical emission spectra to atomic (or molecular) structures, atoms (and molecules) usually are depicted in an energy level diagram. The central wavelength λ_0 of an emission line of a transition from a higher energy state $|i\rangle$ to a lower energy state $|k\rangle$ is connected with the photon energy ΔE via:

$$\lambda_0 = hc/\Delta E = hc/(E_k - E_i) \quad (2.1)$$

h is the Planck constant and c the speed of light. The intensity of the emission line is proportional to the population density of the higher energy state, if other de-excitation mechanisms prove negligible. The spectroscopic notation of the energy states yields information about the respective quantum numbers. For light atoms, LS-coupling is valid and the corresponding notation is used [Fantz06]:

$$nl^w 2S+1 L_{L+S} \quad (2.2)$$

n denotes the main quantum number, l is the orbital angular momentum, w is the number of electrons in the atomic shell, s denotes the angular momentum, the so-called spin. Upper-case letters (L; S) represent the sum of the respective momenta.

$L + S = J$ is the total angular momentum. A corresponding notation is applied for diatomic molecules [ibid.]:

$$nl^w 2S+1 \Lambda_{\Lambda+\Sigma}^{+,-}_{g,u} \quad (2.3)$$

the Greek letters denote the projection of the corresponding vectors onto the molecular axis, and $+$, $-$ and g , u show the symmetry of the electronic wavefunction.

The transition from one energy state to another has to follow the dipole selection rules. Table 2.1 shows the allowed changes of S , L , and J for one-photon transitions of an atom. Selection rules for molecular transitions can be found in e.g. [Svanberg01].

angular momentum	one-photon selection rules
ΔS	0
ΔL	± 1
ΔJ	± 1

Table 2.1: Allowed changes for one-photon transitions of an atom

Figure 2.1 presents an energy level diagram for helium, the main feed gas of the plasma diagnosed in this work. Helium is an atom with two electrons. The total spin $S = s_1 + s_2$ is composed of the respective electron spins s_1 and s_2 . It can adopt the values 1 and 0. The energy level diagram is thus divided into singlet states and

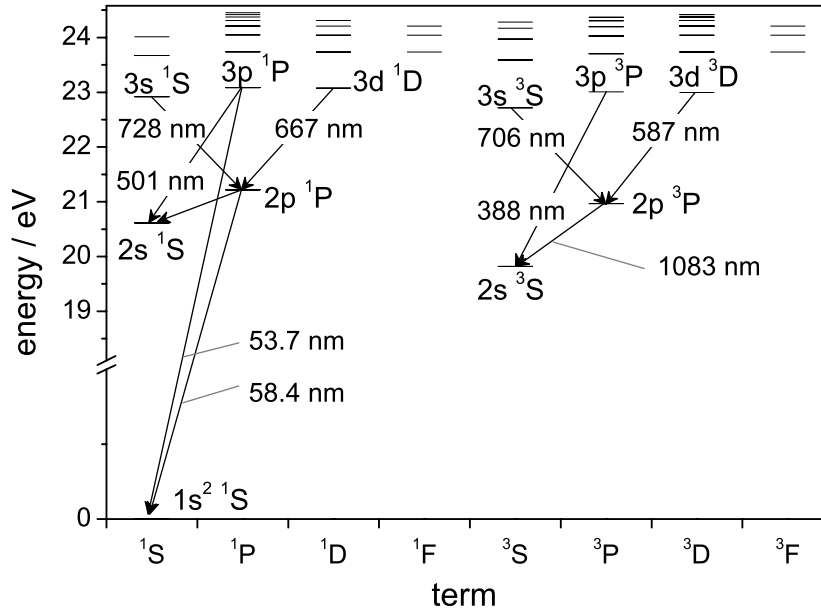


Figure 2.1: Energy level diagram for helium. The energy states are labelled according to notation (2.2). The main radiative transitions are indicated by arrows labelled with their respective wavelength.

triplet states that do not interact via radiative transitions. For $S = 1$ the three triplet states are $|\uparrow\uparrow\rangle$, $\frac{1}{\sqrt{2}}(|\uparrow\downarrow\rangle + |\downarrow\uparrow\rangle)$, and $|\downarrow\downarrow\rangle$. The singlet state for $S = 0$ is $\frac{1}{\sqrt{2}}(|\uparrow\downarrow\rangle - |\downarrow\uparrow\rangle)$ [Schwabl05].

The first excited state in the singlet system has a very high excitation energy of ~ 20 eV. Thus, radiative transitions in the visible spectral range are transitions between excited states. Transitions from an excited state to the ground state (e.g. $3p^1P$ to $1s^2^1S$ with $\lambda = 53.7$ nm) are called resonance transitions. Excited states that have no allowed radiative transition are called metastable states (e.g. $2s^3S$). Compared to radiative states, the metastable states' lifetime is higher by orders of magnitude.

2.1.2 Excitation and De-Excitation Mechanisms

For a plasma in thermal equilibrium, the population density of excited states is described by the Boltzmann distribution. Low temperature atmospheric pressure plasmas are far from (local) thermal equilibrium. Thus, their population densities do not necessarily follow the Boltzmann distribution and further populating and depopulating processes have to be taken into account, such as e.g. electron or heavy particle impact excitation and de-excitation, radiation absorption, spontaneous emission, or radiative recombination. The population densities in low temperature atmospheric pressure plasmas, therefore, depend on a variety of plasma parameters such as electron density and temperature, radiation field, and molecular and atomic species densities. The excitation processes are described by their probabilities, which are the Einstein transition probabilities for radiative transitions, and cross sections for collision induced transitions. The corresponding rate coefficients can be obtained by convoluting the cross section with the energy distribution function of the impact particle. In order to derive information about plasma parameters and particle densities from optical emission spectra, population models are required, which consider populating and depopulating processes for each individual level of a particle [Fantz06]. A commonly applied model is the so-called corona model¹, which is based on the assumption that excitation occurs only from the ground state and only due to electron impact. According to the model, de-excitation only occurs by radiative transitions, allowed by the selection rules. The model can be extended by incorporating additional processes, such as further population processes from higher states,

¹The model applies to plasmas which have a low electron density, a high electron temperature, and negligible radiation, such as the solar corona, the eponym for the model.

by considering excitation from energy states other than the ground state, by taking into account the radiation field and reabsorption of emitted light, and also energy state transitions due to collisions can be considered. Taking all these processes into account leads to the more general collisional radiative (CR) model. In this model, rate equations for each state of the respective particle together with the coupling to other particles is set up. Results from CR-calculations can now be correlated to line intensity measurements, and thus information about plasma parameters and particle densities can be derived. At atmospheric pressure, however, collisional de-excitation processes prevail and at ambient conditions it becomes quite complicated to identify all involved species, rate coefficients, and cross sections². In the present work, OES serves to gain rough information about relative particle density distributions and, more importantly, to identify species present in the plasma.

2.1.3 OES-Measurement Setup

Excited species in the effluent of the atmospheric pressure plasma jet (APPJ), which is to be investigated in this study, are detected via optical emission spectroscopy (OES). Figure 2.2 shows a schematic of the setup. The light emitted from the discharge region and from the effluent of the jet is recorded perpendicular to the jet's axis with an optical fibre (Polymicro Technologies Inc., attenuation of 4 dB/km at 800 nm). The light is focused into the fibre by a gradient index (GRIN) lens³ (Newport Corporation). A second GRIN lens collimates the light on the entrance slit of a BM 50 Czerny Turner monochromator (B & M Spectronic, 0.5 m). The spectra are recorded with an optical spectroscopy multichannel analyser (OSMA) from Spectroscopy Instruments GmbH. The analyser has a silicon photo diode array with 1024 elements and an overall length of 25.6 mm. The quantum efficiency is 0.7 at 660 nm. The detector head is cooled to a temperature of approximately 250 K by a water cooled Peltier element. This setup has a resolution of 0.161 nm per pixel and a total single shot wavelength range of 165 nm.

²Quenching rate coefficients can be determined by RF-phase resolved observation of emission lines. According investigations by phase resolved optical emission spectroscopy (PROES) in laboratories of the Ruhr-University Bochum already showed first results (L. Schaper, *Charakterisierung eines Plasmajets zur Oberflächenbehandlung mit Hilfe von optischer Emissionsspektroskopie*, diploma thesis, University of Duisburg-Essen, submitted July 2007 [Schaper07]).

³GRIN lenses focus the light through a precisely adjusted radial variation of the refractive index of the lens material from the centre of the lens to the edge.

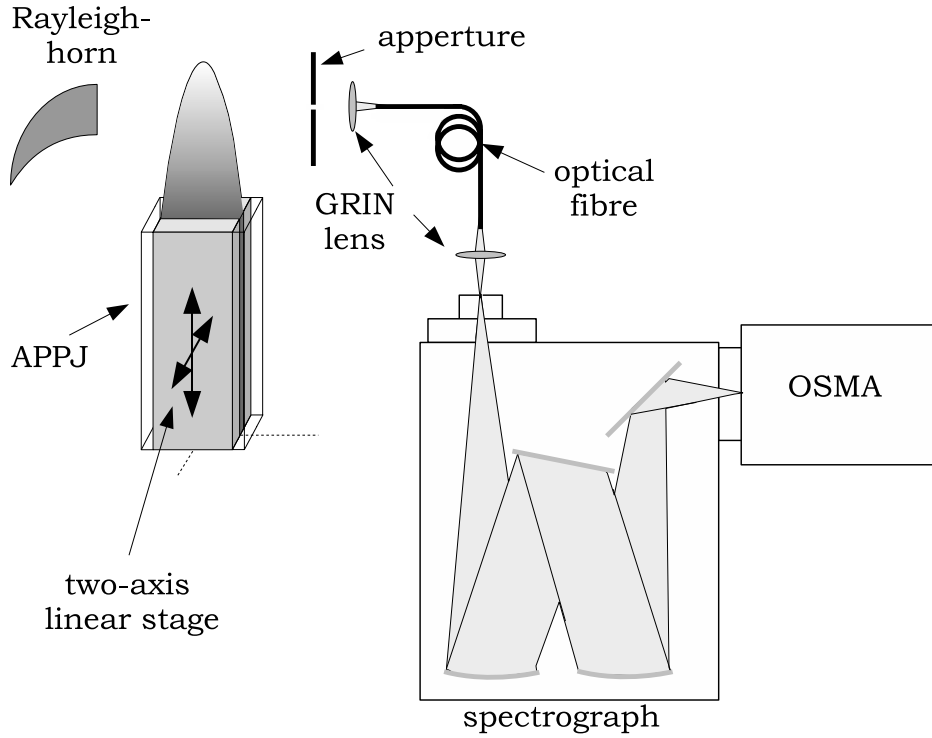


Figure 2.2: Experimental setup of the optical emission spectroscopy measurements on the atmospheric pressure plasma jet

2.2 Absorption Spectroscopy

In contrast to optical emission spectroscopy, absorption spectroscopy yields direct quantitative information about ground state atom and molecule densities. For absorption measurements, the plasma is transilluminated with probe radiation and the consequent change in the probe radiation intensity is recorded. An advantage of absorption spectroscopy is that the disturbing influence of plasma radiation can be almost entirely excluded: The plasma radiation decreases quadratically with the distance, whereas the probe radiation is concentrated in a beam of small divergence. Plasma radiation and probe radiation can thus easily be separated [Döbele95]. Like OES, absorption spectroscopic methods only provide line of sight integrated information, unless tomographic methods are applied. For a homogeneous plasma of the length L , the reduced probe radiation intensity is described by Beer's law:

$$I_\nu(L) = I_\nu(0) \cdot e^{\frac{h\nu_{21}}{c} \cdot (B_{21}n_{1g}(\nu) - B_{12}n_{2g}(\nu)) \cdot L} = I_\nu(0) \cdot e^{\kappa'_\nu L} \quad (2.4)$$

where $\kappa'_\nu(\nu)$ is the absorption coefficient including stimulated emission, and $B_{21} = \frac{c^3}{8\pi h \nu^3} \cdot A_{21}$ is the Einstein coefficient of induced emission with A_{21} being the Einstein coefficient of spontaneous emission. $g(\nu)$ is the normalised line profile. The population density of energy state i is given by n_i . $I_\nu(0)$ is the initial intensity of the probe radiation, and $I_\nu(L)$ is the intensity of the probe radiation with absorption after it transirradiated the plasma. With

$$g_1 B_{21} = g_2 B_{12} \quad \text{and} \quad \frac{n_2}{n_1} = \frac{g_2}{g_1} \cdot e^{-\frac{E_2-E_1}{kT}}$$

$\kappa'_\nu(\nu)$ can be written as:

$$\kappa'_\nu(\nu) = \frac{h\nu_{21}}{c} g(\nu) B_{12} \cdot n_1 \left(1 - \frac{g_1}{g_2} \frac{g_2}{g_1} e^{-\frac{h\nu_{21}}{kT}} \right) \quad (2.5)$$

$$\Rightarrow \kappa'_\nu(\nu) = \kappa_\nu \left(1 - e^{-\frac{h\nu_{21}}{kT}} \right) \quad (2.6)$$

g_1 and g_2 are the statistical weights of the respective energy states.

Is $\frac{h\nu}{kT} \gg 1$, or $n_1 \gg n_2$, stimulated emission is negligible and thus equation 2.4 reduces to:

$$\frac{I_\nu(L)}{I_\nu(0)} = e^{\kappa_\nu L} \quad (2.7)$$

with $\kappa_\nu = \frac{h\nu_{21}}{c} \cdot g(\nu) \cdot B_{12} \cdot n_1$ follows

$$\ln \frac{I_\nu(L)}{I_\nu(0)} = \frac{h\nu_{21}}{c} \cdot g(\nu) \cdot B_{12} \cdot n_1 \cdot L \quad (2.8)$$

Is the probe radiation spectrally small compared to the absorption profile⁴, $g(\nu)$ can be measured and the line of sight averaged ground state atom density $n_1 \cdot L$ can be calculated:

$$n_1 \cdot L = 8\pi\nu_0^2 c \cdot \frac{g_1}{g_2 A_{21}} \cdot \int \ln \left(\frac{I_\nu(L)}{I_\nu(0)} \right) d\nu \quad (2.9)$$

To achieve space resolved densities from the line of sight integrated densities, several approaches are possible [Hughey82]. Tomography is the most precise method, only it necessitates very high experimental effort. For plasmas with cylindrical symmetry, Abel inversion, which leads to line of sight density as a function of radius, is a well known method [Walsh00, Luque98]. For rectangularly shaped plasmas, an

⁴In this work, the width of a line profile is given as full width at half maximum (FWHM).

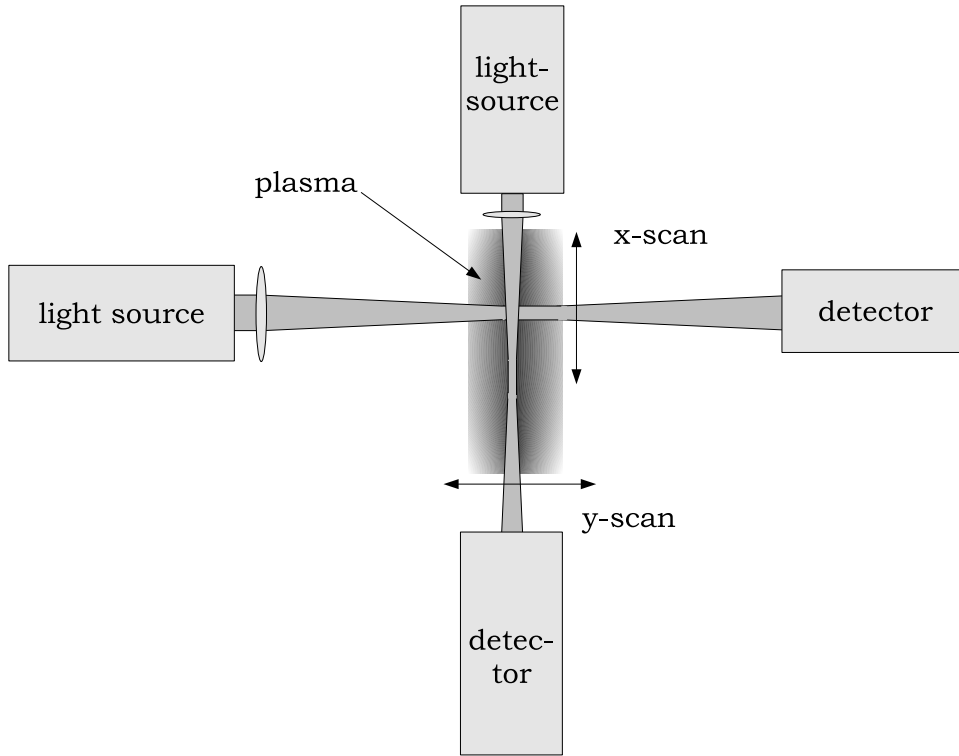


Figure 2.3: x- and y-scan for a tomographic approximation of the space resolved density measurement

estimate of the space resolved ground state density can be derived by the following tomographical approximation. From two transversal scans of the plasma (see figure 2.3), the local density in the section plane can be determined via:

$$n(x, y) \approx \frac{\int n dx \cdot \int n dy}{\iint n dx dy} \quad (2.10)$$

2.3 Laser Induced Fluorescence Spectroscopy (LIF/TALIF)

Laser induced fluorescence (LIF) spectroscopy is based on the following principle: by narrow-bandwidth tunable laser radiation, atoms⁵ are transferred from the ground state to an excited, bound state. From this state, the atom passes to a lower energy

⁵LIF spectroscopy can also be carried out on molecules. For simplicity reasons, the text will only mention atoms in the following.

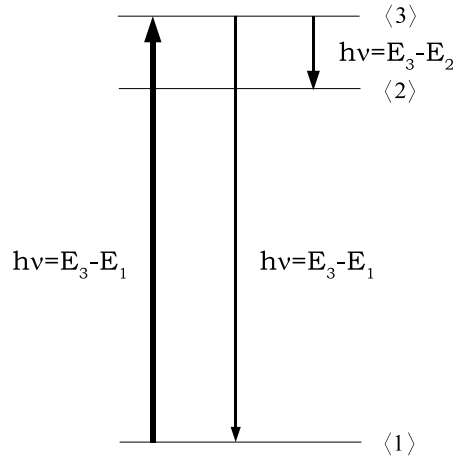


Figure 2.4: Energy diagram of laser induced fluorescence (LIF) interaction in atoms: Spectrally tuned laser radiation is absorbed by the atom which in the following emits fluorescence radiation by spontaneous emission.

state by spontaneous emission (see figure 2.4). The resulting fluorescence radiation is observed. Under optimum experimental conditions, the fluorescence radiation yields information about time and space resolved density and energy distribution of the atom's ground state. Space resolution results from the specific setup (see figure 2.5), where the volume of observation is determined by the overlap of the focal region of the laser beam with the detection region, imaged onto the detector. Time resolution is based on probing of the atoms by pulsed laser radiation; it is given by the pulse length of the laser.

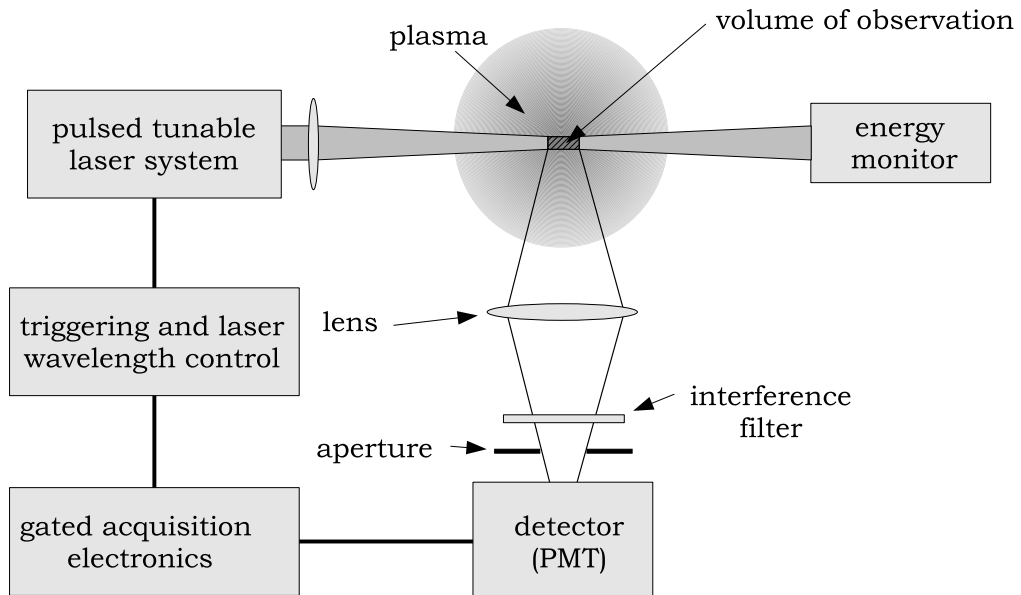


Figure 2.5: Schematic setup of laser induced fluorescence (LIF) experiments

For one-photon LIF measurements the following disadvantages need to be taken into account: Firstly, in an optically thick plasma the fluorescence radiation emitted by the probed atoms can be reabsorbed, obscuring the measurements. Secondly, light atoms such as hydrogen, carbon, oxygen, have their first excited levels, optically connected to the ground state, at energies above 6.5 eV. For these species one-photon excitation can only be achieved with vacuum-ultraviolet (VUV) photons, i.e. with wavelengths shorter than 190 nm [Amorim00]. This makes it experimentally challenging to determine these species' ground state densities.

The problems of one-photon LIF can be overcome by exciting the atom with two photons in the ultraviolet spectral range instead of excitation by a single VUV-photon (see e.g. [Döbele05]). This diagnostic technique is called two-photon absorption laser induced fluorescence (TALIF) spectroscopy. The resulting fluorescence radiation is emitted at a different wavelength, because the selection rules prohibit a de-excitation directly back to the ground state. A distortion of the measurement by laser stray light or by reabsorption of the fluorescence radiation can thus be avoided. This diagnostic technique has been successfully applied for density measurements on, for example, fluorine [Francis03], oxygen [Niemi03a], or hydrogen [Thomson99]. In the following, an introduction to the fundamentals of TALIF will be given.

2.3.1 Two-Photon Excitation

Two-photon absorption, although experimentally achieved not until 1961 [Kaiser61]⁶, was already theoretically described by perturbation theory thirty years earlier in 1931 [Goeppert-Mayer31]. Two-photon excitation of an atom from state $\langle 1 \rangle$ to state $\langle 3 \rangle$ is accomplished by simultaneous absorption of two photons through a virtual intermediate state⁷ $\langle i \rangle$ (see figure 2.6).

De-excitation of the excited state can take place by spontaneous emission – this being the desired case, because it produces the detectable fluorescence radiation –, as well as through absorption of a third photon and subsequent photoionisation, or by collisional quenching, which forms a considerable part of the de-excitation processes at atmospheric pressure. In case the major part of the atoms remains in ground state, and the laser intensity is low enough so that no Stark splitting occurs, the TALIF process can be described by a simple rate model.

⁶Kaiser et al. used a pulsed ruby laser for TALIF-spectroscopy on a $\text{CaF}_2:\text{Eu}^{2+}$ -crystal.

⁷The virtual state is not a solution of Schrödinger's equation.

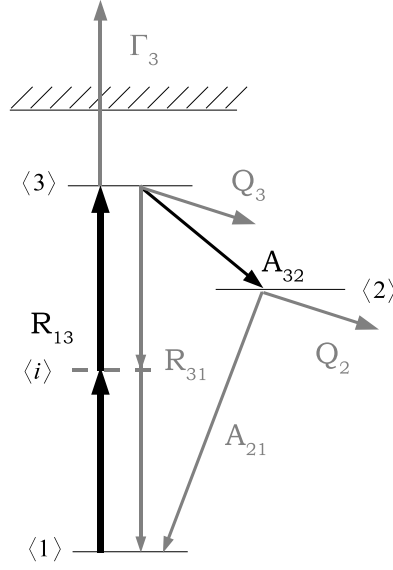


Figure 2.6: Excitation and de-excitation processes in TALIF-spectroscopy. R_{13} denotes the induced two-photon excitation rate, R_{31} is the rate of stimulated two-photon emission, A_{32} and A_{21} are the spontaneous emission rates, Q_3 and Q_2 are the effective quenching coefficients, and Γ_3 is the photoionisation rate.

2.3.2 TALIF Rate Equation Model

The following two rate equations describe the population n_1 of the atom's ground state and n_3 of the two-photon excited state:

$$\frac{d}{dt}n_1(t) = -R_{13}(t)n_1(t) \quad (2.11a)$$

$$\frac{d}{dt}n_3(t) = R_{13}(t)n_1(t) - (A_3 + Q_3 + \Gamma_3(t))n_3(t) \quad (2.11b)$$

$R(t)$ is the two-photon excitation rate. A_3 is the spontaneous emission rate of the upper state, Q_3 is the collisional quenching rate, and $\Gamma_3(t)$ is the photoionisation rate. Each will be described in detail in the following.

2.3.2.1 The Two-Photon Excitation Rate $R(t)$

The two-photon excitation rate $R(t)$ can be described by the two-photon excitation cross section $\sigma^{(2)}$ [Goehlich98]:

$$R(t) = G^{(2)}\sigma^{(2)}g(\nu)\left(\frac{I_0}{h\nu}\right)^2 \quad (2.12)$$

here, $G^{(2)}$ is the photon statistic factor, $g(\nu)$ describes the normalised line profile ($\int g(\nu)d\nu = 1$) of the two-photon excitation, and I_0 is the intensity (in W/cm^2) of

the laser beam with the central frequency ν . The quadratic dependency on the laser intensity is a result of the simultaneous absorption of two photons.

The photon statistic factor $G^{(2)}$ accounts for statistical fluctuations of the laser intensity and is defined as [Loudon83]:

$$G^{(2)} = \frac{\langle I(t)^2 \rangle}{\langle I(t) \rangle^2} \quad (2.13)$$

Since the coherence time of a pulsed dye laser, as used in this work, is in the order of picoseconds and detecting systems usually are slower by orders of magnitude, the respective measurements resemble an average over several phase-uncorrelated laser modes. In this case, $\langle I(t)^2 \rangle$ and $\langle I(t) \rangle^2$ differ by the factor $G^{(2)} = 2$ [Payne81].

The two-photon excitation cross section $\sigma^{(2)}$ follows from the perturbation theory [Goeppert-Mayer31]:

$$\sigma^{(2)} = \left(\frac{\pi \nu_L}{c \epsilon_0 \hbar} \right) \left| \sum_i \frac{\langle m | \mathcal{H} | i \rangle \langle i | \mathcal{H} | g \rangle}{\nu_{gi} - \nu_L} \right|^2 \quad (2.14)$$

It is a measure for the probability that the atom is excited from ground state $|g\rangle$ to the excited state $|m\rangle$ in the radiation field with the frequency ν_L by simultaneous absorption of two photons. The sum is over all virtual intermediate states $|i\rangle$ the atom can adopt during the two-photon transition. $\mathcal{H} = \hat{\boldsymbol{\mu}} \mathbf{e}$ is the interaction Hamiltonian for a polarisation \mathbf{e} of the laser beam [Marx78]. $\hat{\boldsymbol{\mu}} = -e \sum_i \mathbf{r}_i$ is the dipole operator with the space operator \mathbf{r}_i of the i^{th} electron. Equation 2.14 is valid for excitation by two photons originating from the same laser.

The transition from $|g\rangle$ to $|m\rangle$ has to follow the dipole selection rules, which can be derived from the matrix element $|M_{gm}^{(2)}| = (\epsilon_0 \hbar)^{-1/2} \langle m | \mathcal{H} | i \rangle \langle i | \mathcal{H} | g \rangle$ [Bonin84, Flusberg76]. $|M_{gm}^{(2)}|$ is composed of two subsequent one-photon matrix elements, thus the optical selection rules are a combination of two one-photon steps. Accordingly, the selection rules for the allowed changes of spin S , orbital angular momentum L , and total angular momentum J for two-photon transitions (see table 2.2) follow directly from the selection rules for one-photon transitions (see table 2.1). A comparison of both selection rules shows that with two-photon absorption, states can be reached, which are unobtainable by one-photon absorption. Not all shown transitions are allowed for arbitrary polarisations: For example, $\Delta J = 1$ is forbidden for photons of equal energy.

angular momentum	two-photon selection rules
ΔS	0
ΔL	0, ± 2
ΔJ	0, $\pm 1, \pm 2$

Table 2.2: Allowed changes for two-photon transitions of an atom. S = spin, L = orbital angular momentum, and J = total angular momentum.

The normalised line profile $g(\nu)$ results from the convolution of the absorption profile and the effective two-photon laser line profile $g_L(\nu)$ (see equation 2.15). The absorption profile of the two-photon transition itself is a convolution of the natural homogeneous line profile $g_h(\nu, \vec{v})$, the Doppler broadened line profile due to the velocity distribution of the atoms $g_D(\vec{v})$, and the pressure broadened line profile due to collisions $g_P(\nu)$, where all respective line profiles are area normalised.

$$g(\nu) = g_h(\nu, \vec{v}) \star g_D(\nu, \vec{v}) \star g_P(\nu) \star g_L(\nu) \quad (2.15)$$

The homogeneous line profile is broadened due to the finite lifetime τ_i of excited states. From this finite lifetime results that the energy of the excited state can only be determined with the accuracy given by Heisenberg's uncertainty principle $E_i \geq h/(2\pi\tau_i)$. τ_i is the inverse of the Einstein coefficients A_i . The resulting Lorentz-shaped line profile is given by:

$$g(\nu, \vec{v}) = \frac{1}{\pi} \frac{A_i/4\pi}{(2\nu_L - \nu_{gi} + k\vec{v}/\pi)^2 + (A_i/4\pi)^2} \quad (2.16)$$

Because the atom moves with the velocity \vec{v} , the frequency $\nu/2\pi$ in the moving system is shifted to $(\nu - k\vec{v})/2\pi$. k is the wave vector of the laser beam, and $A_i/2\pi$ is the homogeneous line width. The Doppler broadening results from the movement of the atoms with respect to the laser beam. In thermodynamic equilibrium, the velocity distribution is Maxwellian:

$$g_D(\vec{v}) = \pi^{-3/2} v_0^{-3} e^{-(|\vec{v}|/v_0)^2} \text{ with } v_0 = \sqrt{2kT \ln 2 / m} \quad (2.17)$$

v_0 is the mean velocity of the atoms, T the gas temperature, m the atom's mass, and here k is the Boltzmann coefficient.

In the present study, TALIF is performed at atmospheric pressure, which means that a significant part of the line broadening can be attributed to collisional broad-

ening. Collisional broadening is caused by elastic and inelastic collisions between the absorbing atom and a foreign atom. During an elastic collision, the two collision partners form a temporary quasi molecule [Mitchell71] with shifted energy levels compared to the single atoms, statistically leading to absorption line broadening. During inelastic collisions, the excitation energy E_m is transferred in part or completely to the collider or into translatory energy of both collision partners. These quenching collisions reduce the effective lifetime τ_m of the excited state E_m and therefore lead to a further broadening of the absorption line [Demtröder04].

The overall resulting line profile $g(\nu)$ is a convolution of above described line profiles (see equation 2.15). Under the assumption that the laser line profile is Gaussian, and the homogeneous line profile can be neglected with respect to all other line widths [Marx78], and the pressure broadened line profile is Lorentzian, a Voigt profile results from the line profile convolution [Wells99, Armstrong67].

2.3.2.2 The Fluorescence Photon Yield

Two conditions concerning the laser intensity have to be fulfilled for the rate equation system 2.11a and 2.11b: The laser intensity has to be kept low enough to leave the ground state density practically unchanged so that $n_1(t) \approx n_0$. For a rectangular laser pulse of duration T , and the solution for equation 2.11a: $n_1(t) = n_0 e^{-\int_0^t R_{13}(t') dt'}$, the laser intensity has to be much lower than the saturation intensity derived from the criterion $\int_0^T R_{13}(t') dt' = 1$:

$$I_s^{(2)} = \frac{h\nu}{\sqrt{\sigma^{(2)}T}} \quad (2.18)$$

The second condition regarding the laser intensity concerns photoionisation. The ionisation rate can be expressed by the ionisation cross section of the upper state [Goehlich98]:

$$\Gamma(t) = \frac{\sigma_i}{h\nu} I_0(t) \quad (2.19)$$

For a laser pulse of duration T , where T is significantly smaller than the effective lifetime τ of the excited state, the criterion for ionisation saturation can be defined as $\int_0^T \Gamma(t') dt' = 1$ and it follows for the laser intensity:

$$I \ll I_s^i = \frac{h\nu}{\sigma_i T} \quad (2.20)$$

In the unsaturated case ($I \ll I_S^{(2)}; I_S^i$), equation 2.11b can be written as:

$$\frac{d}{dt}n_3(t) = R_{13}(t)n_0 - (A_3 + Q_3)n_3(t) \quad (2.21)$$

From this, the density of the excited atoms can be derived:

$$n_3(t) = n_0 \int_0^t R(t') e^{-(A_3+Q_3)(t-t')} dt' \quad (2.22)$$

The number of generated fluorescence photons is given by:

$$\begin{aligned} n_f &= A_{32} \int_0^\infty dt n_3(t) = n_0 A_{32} \int_0^\infty dt e^{-(A_3+Q_3)t} \int_0^t dt' e^{(A_3+Q_3)t'} R(t') \\ &= n_0 a_{32} \int_0^\infty R(t') dt' \end{aligned} \quad (2.23)$$

introducing $a_{32} = \frac{A_{32}}{A_3+Q_3}$ as the reduced optical branching ratio. Inserting $R(t)$ from equation 2.12 yields:

$$n_f = \frac{A_{32}}{A_3 + Q_3} \frac{\sigma^{(2)}}{(h\nu)^2} G^{(2)} g(\nu) n_0 \int_0^\infty I_0^2 dt \quad (2.24)$$

where A_{32} denotes the Einstein coefficient for the observed fluorescence channel, $A_3 = \sum_{m<3} A_{3m} g_{3k}$ is the total transition probability of the upper state, and $Q_3 = \sum_q k_q^{(3)} n_q$ is the effective quenching rate, constituted by the quench coefficients k_q of the excited state with the collision partner densities n_q . The radiation reabsorption in optically thick media is accounted for by the escape factor g_{3k} [McWhirter65, Holstein47, Holstein51].

For the determination of absolute ground state densities of atomic oxygen in the present study, also the following considerations need to be taken into account:

A measurement of the fluorescence radiation pattern as a function of the polarisation angle of the linear polarised laser beam shows that the fluorescence radiation of the TALIF transitions studied in this work exhibits an isotropic distribution [Niemi04].

Three effects can alter the fluorescence photon yield and, therefore, have to be prevented. Each of these processes is a result of too high laser intensity:

Even though the cross section is small, stimulated two-photon emission might occur (analogous to one-photon stimulated emission). Figure 2.6 shows that the

stimulated two-photon emission rate is given by R_{31} . When condition 2.18 is met, then $n_3/n_1 \ll 1$ and reoccupation by cascade transitions can be neglected ($R_{31} \approx R_{13} \Rightarrow R_{31}n_3 \ll R_{13}n_1$) [Niemi03a].

Amplified spontaneous emission (ASE) can occur as a result of the possible population inversion of the excited state to the thermally not occupied intermediate state. Is the excited state populated more quickly than it is depopulated by fluorescence or quenching, the spontaneous fluorescence emission is amplified. Due to the geometry of the excitation, the amplification mainly occurs along the laser beam and is therefore lost for detection.

Furthermore, photodissociation might influence the measured fluorescence radiation. This process leads to a higher TALIF-signal, since it generates a surplus of the probed atoms. In the present work, a cylindrical lens is used to avoid such artificial particle generation (here generation of O-atoms by photodissociation of O_3 or O_2). This lens yields a horizontal focal line of the laser so that – at the cost of a larger excitation volume – a smaller local laser intensity can be gained.

Chapter 3

The Atmospheric Pressure Plasma Jet (APPJ)

In this chapter, the atmospheric pressure plasma jet (APPJ) is presented. Following a description of the classical setup, consisting of two concentric electrodes, the modified planar APPJ, developed for this study, is introduced. The jet's working principle as well as characterising thermal, electrical, and spectroscopic measurements are presented, distinguishing its two substantial sections: discharge and effluent.

3.1 Setup of the APPJ

The atmospheric pressure plasma jet (APPJ) is a capacitively coupled radio frequency discharge usually operated at 13.56 MHz. The original setup of the APPJ, developed by Selwyn, Hicks, and coworkers [Selwyn99], was modified during the course of this study. In this chapter, a description of the classical (concentric) APPJ setup is followed by the presentation of the modified (planar) setup, developed to allow insight into the jet's glow discharge region.

3.1.1 Concentric APPJ

A schematic of the APPJ is shown in figure 3.1. The jet consists of two concentric stainless steel electrodes with an interjacent polytetrafluoroethylene (PTFE) spacer. The spacer aligns the inner electrode so that a uniform electrode gap along the entire electrode length is ensured. Furthermore, the PTFE-spacer insulates the outer electrode from the inner one, and it also functions as diffuser and stopper for the feed

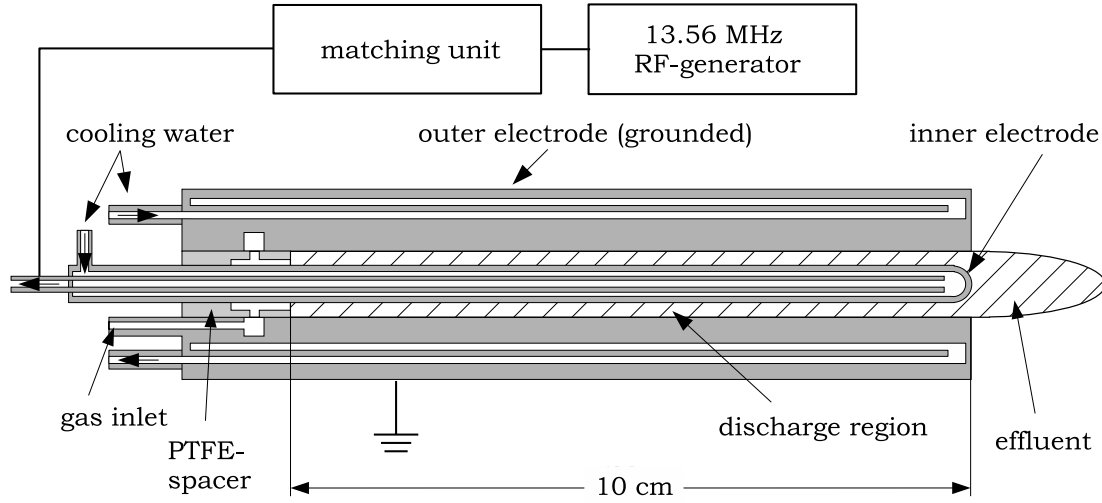


Figure 3.1: Schematic of the concentric APPJ

gas. The outer electrode's inner diameter measures 14 mm. Two exchangeable inner electrodes allow an electrode gap of 2 mm and 1.1 mm respectively. The effective electrode length is 10 cm. To ensure an even and smooth surface, the electrodes are electropolished. Each electrode is double-walled and water cooled, having a water in- and outlet at the rear side of the jet. The cooling water flux is 140 l h^{-1} . Inner and outer electrode have a parallel cooling circuit to inhibit parasitic resistances through the cooling water. The outer electrode is grounded while the inner electrode is connected to an L-type matching network and a 13.56 MHz RF-generator. The L-network prevents reflection of the RF-power by impedance matching of the dis-

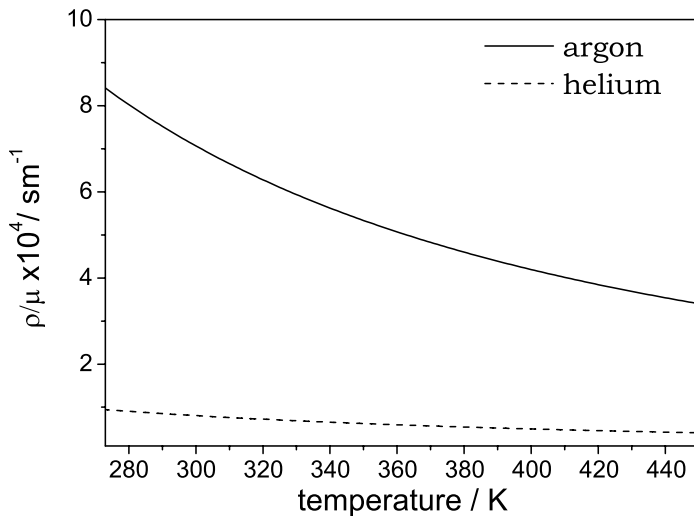


Figure 3.2: $q = \frac{p}{\mu}$ as a function of gas temperature (values for viscosities and densities are taken from [Lemmon05])

charge to the RF-generator [Norström79]. The jet can be operated at powers ranging from 20 to about 200 Watt. In the low power regime, the discharge runs unsteady or is not ignited, in the high power regime, the glow discharge constricts to an arclike- or γ -mode discharge [Yang05b, Wang03].

The electric, water, and gas connections of the jet are shielded by a brazen casing. The feed gas consists of 0.5 to 4 m³h⁻¹ noble gas (helium or argon with a purity of 99.999%) with an admixture of oxygen in the order of 1 vol% (99.999% purity), controlled by flowrators. A laminar gas flow can be assumed at these flow rates, since approximations of the Reynolds number for the setup and parameters used in this work are all below the critical Reynolds number of 2100 [Rott90]. The Reynolds number can be calculated by equation 3.1:

$$Re = \frac{d\rho\bar{v}}{\mu} = d\bar{v}q \quad (3.1)$$

with $q = \frac{\rho}{\mu}$, a dynamic viscosity for argon of $\mu_{Ar}(300\text{ K}) = 2.2613 \cdot 10^{-5}\text{ Pa}$, a dynamic viscosity for helium of $\mu_{He}(300\text{ K}) = 1.993 \cdot 10^{-5}\text{ Pa}$, an argon density of $\rho_{Ar} = 1.6025\text{ kg}\cdot\text{m}^{-3}$, and a helium density of $\rho_{He} = 0.1604\text{ kg}\cdot\text{m}^{-3}$ [Lemmon05, Macrossan03]. \bar{v} is calculated from the gas flux in kg·m⁻³ and a cross sectional area of the jet of $A_{d=1.1\text{ mm}} \approx 0.45\text{ cm}^2$ and $A_{d=2\text{ mm}} \approx 0.75\text{ cm}^2$ respectively. Figure 3.2 shows that $Re \propto q$ decreases with gas temperature. In figure 3.3 the Reynolds numbers are plotted versus the gas flux for helium and argon at 300 K. Since the APPJ's gas temperature never subsides below 300 K, these are the maximal Reynolds numbers to be expected.

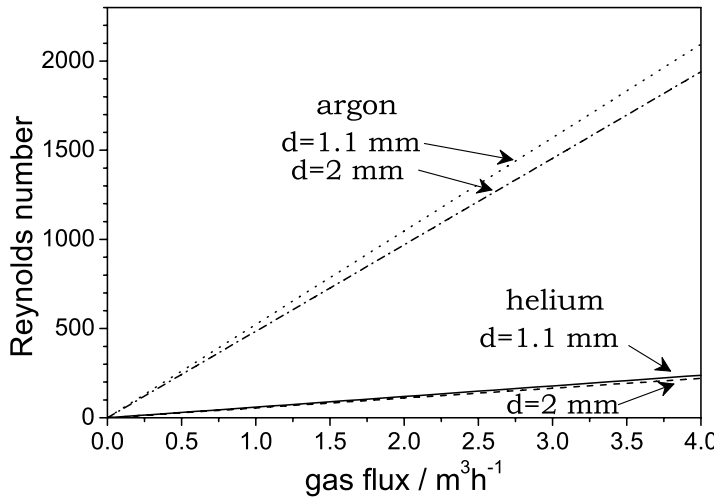


Figure 3.3: Reynolds number at 300 K for helium and argon base gas and for two different electrode gaps of 1.1 mm and 2 mm respectively

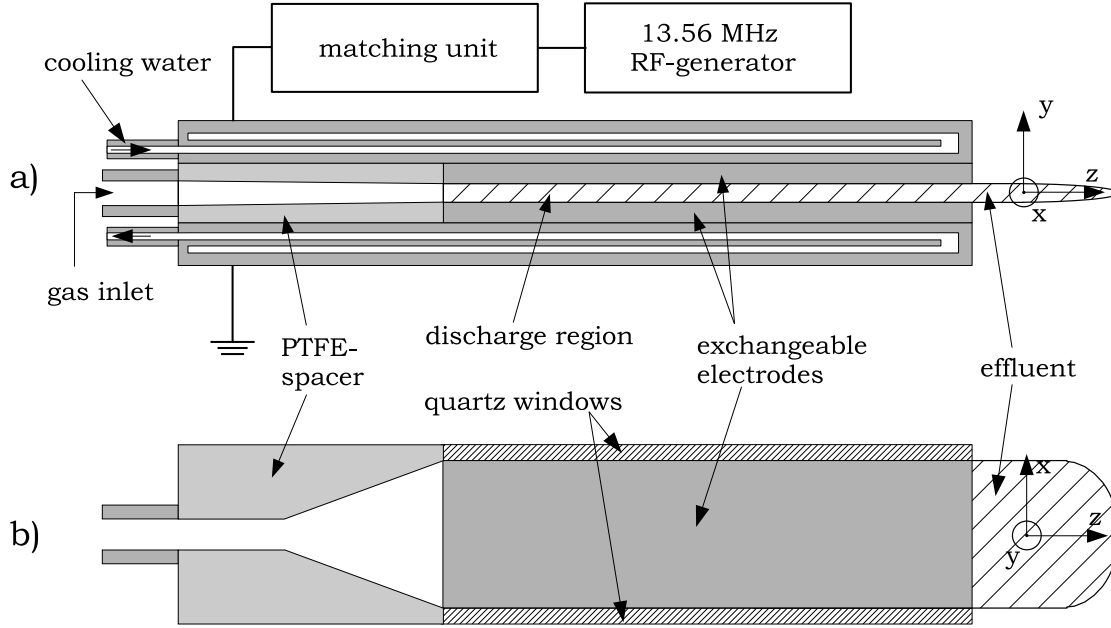


Figure 3.4: Sideview (a) and topview (b) schematics of the planar APPJ

3.1.2 Planar APPJ

In this work, a new APPJ setup was developed. Since the classical concentric setup allows no full insight into the discharge region, the new jet is set up in a plane parallel version, so that a free line of sight through the plasma is now possible. Figure 3.4 shows a schematic of this planar APPJ. Width and cross sectional area of the electrode gap are the same as in the concentric setup, so that the operating conditions of planar and concentric jet are very much alike. In contrast to the classical APPJ setup, the planar APPJ, however, is constructed modular so that it can be operated with electrodes differing in material or thickness, which allows setups with varying electrode gap widths. Comparing measurements on the APPJ with gap widths of 1.1 mm and 2 mm respectively are described in chapter 6.1.1. The exchangeable electrodes are screwed to the upper and lower water cooled (140 l h^{-1}) electrode mount. The upper electrode is connected to a 13.56 MHz RF-generator via an L-type matching unit, while the lower electrode is grounded. The high voltage electrode is additionally shielded by a grounded copper shielding, to reduce RF-interferences and to ensure a secure operation. The gas is fed in at the back of the jet through a PTFE-spacer. The cross section of the gas channel in the PTFE-spacer is largely kept constant, forming a transition from the circular profile of the gas conduct to the rectangular profile of the electrode gap. Apart from serving as a gas

supply, the spacer acts as an insulator between the ‘hot’ electrode and the grounded electrode. The electrode surfaces are electropolished. The sides of the jet are capped with glass (BK7) or quartz windows, to confine the gas flux. Operating the jet in arcing mode can damage the windows. Hence, the planar APPJ is constructed to allow a simple exchange of the windows. As defined in figure 3.4 and used throughout this work, the x-axis denotes the axis perpendicular to the gas flow and parallel to the discharge gap, the y-axis is perpendicular to the gas flow and perpendicular to the discharge gap, and the z-axis is in direction of the gas-flow.

3.2 Working Principle of the APPJ

The APPJ shows a distinct non-thermal behaviour: It has a very low gas temperature ($< 100\text{ }^{\circ}\text{C}$) and physical model calculations [Park00] estimate an electron temperature of 2 to 4 eV. The electron density is approximately 0.2 to $2 \cdot 10^{11}\text{ cm}^{-3}$ [ibid.]. As already mentioned in chapter 1.3, stabilisation of a glow discharge at atmospheric pressure is by no means trivial. The APPJ’s glow discharge stability is established by the following mechanisms: First of all, there is the stabilising effect of radio frequency by ion trapping [Roth07]. Secondly, arcing is prevented by the use of helium as main feed gas which limits ionisation, and by the use of high gas flow rates which reduce the conductivity of the plasma [Raizer01]. Thirdly, active cooling of the electrodes (enhanced by a high gas flux) keeps the gas temperature constant and prevents thermal instability of the glow discharge. A special design of the electrodes is listed as a further stabilisation mechanism in the APPJ patent by Selwyn et al. [Selwyn99]. The stabilising principle is described as follows: There is evidence that indicates that electron density required for plasma sustenance is increased by minimising electron losses by electron trapping by means of the hollow cathode effect; that is, by sheath repulsion at all surfaces along the cavity, except in the axial flow direction [Selwyn99]. This design, however, is only of minor importance for a stable glow discharge mode. It is omitted in the layout of the APPJ used in this study.

Previous works by the AG Döbele¹ proved that the APPJ can be operated in argon [Wang03], although the higher breakdown voltage may cause a rapid multiplication of electrons after breakdown and lead to the formation of streamers or of a filamentary arc [Park01].

¹Institute of Laser and Plasma Physics, University of Essen (now Duisburg-Essen) – Prof. Dr. H. F. Döbele (www.ilp.physik.uni-essen.de/doebele).

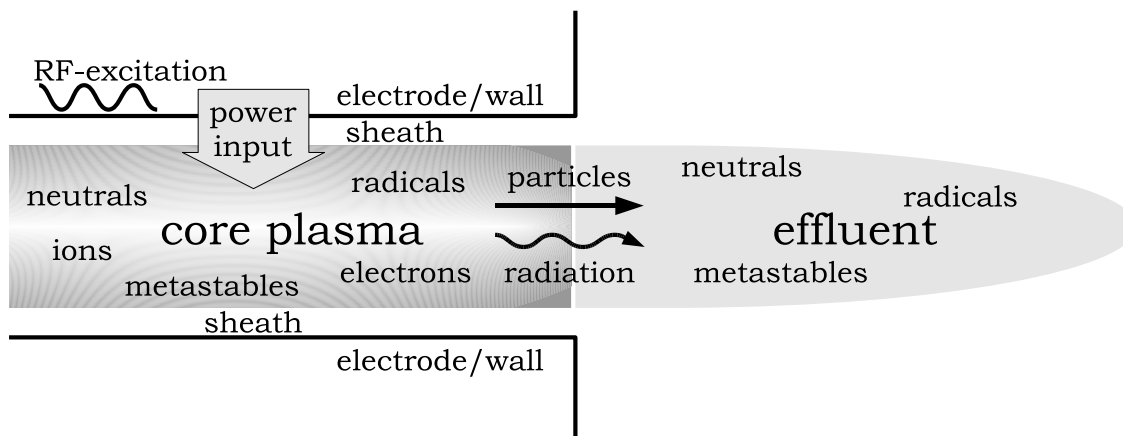


Figure 3.5: Schematic of discharge region, effluent, and processes in the APPJ

3.2.1 Discharge Region and Effluent

Two substantial sections of the atmospheric pressure plasma jet need to be distinguished (see figure 3.5): The discharge region in between the electrodes consists of the core plasma in the centre and two plasma sheaths near the electrodes. Here the discharge is ignited and sustained by RF-power input. The plasma sheaths are regions where, due to their higher velocity only the electrons leave the plasma towards the electrodes, while the positive ions remain at their position. Thus, it is a positively charged region free of electrons. Due to the potential and charge distribution, the plasma sheaths represent capacitors [Raizer95]. Their thickness lies in the order of a few hundred μm [Shi05]. The discharge contains neutrals, radicals, metastables, electrons and ions, and radiation. The species can interact with the electrode walls.

The second substantial region is the effluent, leaving the jet through the nozzle. Here the particle distribution differs significantly from the discharge region. Already at a distance of a tenth of a millimetre, at a flow rate of 12.5 ms^{-1} , one can neglect the influence of the charged species on the reaction chemistry: The recombination coefficient for ions and electrons at atmospheric pressure is approximately $10^{-6}\text{ cm}^3\text{s}^{-1}$, yielding a charged particle density of only 10^{11} cm^{-3} after $10\text{ }\mu\text{s}$ [Jeong00]. This value is well below the concentrations of the reactive neutral species, which are in the range of 10^{15} cm^{-3} (see chapter 4). Species expected to be present in the effluent are therefore neutrals, oxygen radicals, and metastables. Also the radiation in the effluent needs to be considered. Discharge and effluent will be characterised in the following.

3.3 Characterisation of the Discharge Region

To characterise the APPJ's discharge region, current and voltage measurements as well as optical emission spectroscopic measurements are performed. Subsequently, operation with helium as main feed gas is compared to operation with argon.

3.3.1 Current and Voltage Measurement Setup

The RF-voltage is measured with a capacitive probe and the RF-current is detected with an inductive probe, as developed for the so-called GEC reference cell in [Hargis et al.94]. Construction details are shown in figure 3.6. These probes are known to have exceptional bandwidth and linearity. If the probes are small and set up close together, they provide excellent frequency response, as well as voltage and current information at a common point [Hargis et al.94].

The pick-up system needs to be calibrated at the given frequency by comparing the signal amplitudes to reference values. In the present work, calibration was performed by replacing the discharge by a beryllium $50\ \Omega$ power resistor and by calculating voltage and current from the resistor and the known input power. Figure 3.7 shows the resulting calibration curves for 13.56 MHz. The waveforms are recorded with a Tektronix storage oscilloscope TDS210 with $50\ \Omega$ termination resistors.

A complete electric analysis of the plasma source also including the absolute phase information between current and voltage signal and further determination of active and reactive power would have exceeded the extent of this work. The current/voltage measurements nonetheless yield valuable information on e.g. the plasma sheaths and the discharge mode.

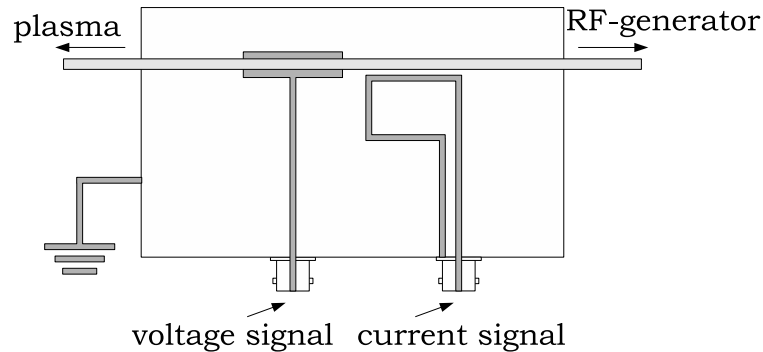


Figure 3.6: Current and voltage pick-up [Hargis et al.94]

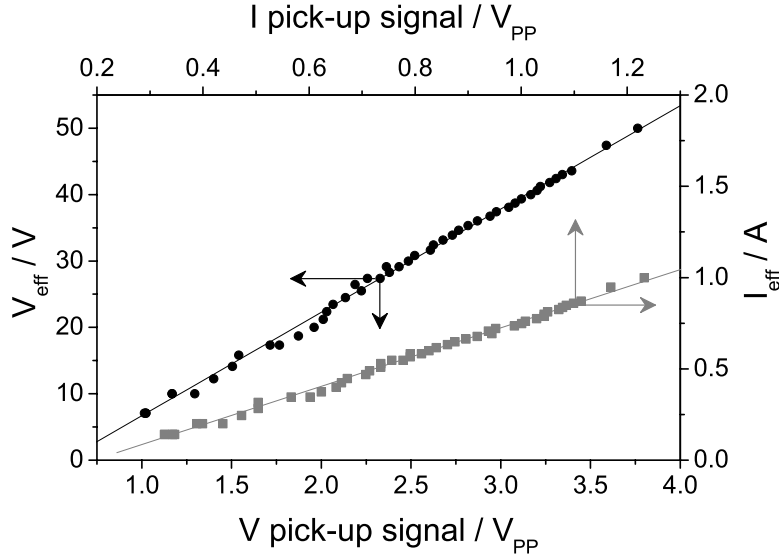


Figure 3.7: Calibration curve of the VI-pick-up

3.3.2 Discharge Operation Modes (α - and γ -Mode)

In figure 3.8 a VI-characteristic of the planar APPJ operated with $2\text{ m}^3/\text{h}$ helium and an oxygen admixture of 0.5 vol% is presented. The breakdown occurs at $\sim 160\text{ V}$ at point A. From that point onwards, the voltage rises proportionally to the discharge current. This proves that the APPJ is operated in the abnormal glow discharge regime (see chapter 1.2) as was already reported for atmospheric pressure RF-discharges with gaps smaller than 2 mm in [Moon06]. In some cases, the normal glow regime – where the voltage remains constant with increasing current – can be observed when the discharge does not immediately spread over the entire electrodes' area [Moon06]. With increasing power, the discharge area increases, explaining the constant voltage at increasing current. In the present case, the VI-characteristic correlates well with the observation that instantly after breakdown the discharge covers the total area of the electrodes. From point A to point B the APPJ is operated in α -mode, meaning that the plasma is sustained by bulk ionisation in the same way as is the case for low pressure RF-discharges [Raizer95]. At point B in the VI-characteristic, a further power increase results in an abrupt decrease of discharge voltage and transition from α - to γ -mode. The γ -mode is characterised by sheath breakdown, because the dominating ionisation process is ionisation near the electrodes due to secondary electrons emitted from the electrodes surface. Due to this breakdown of the plasma sheaths, the discharge becomes more resistive and the capacitive part decreases. This becomes evident when current and voltage waveforms are observed during the transition from α - to γ -mode (see figure 3.9). The phase

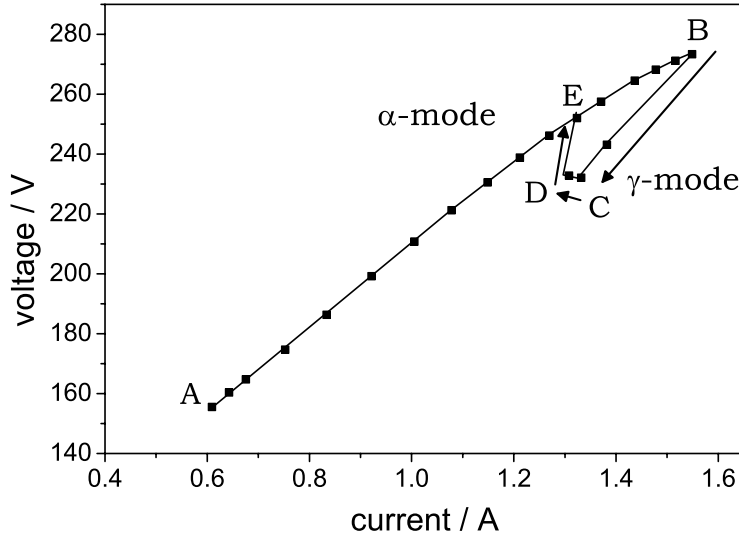


Figure 3.8:
VI-characteristic of the
APPJ exhibiting α - to
 γ -mode transition

between voltage and current signal decreases due to the decrease of the capacitive portion of the discharge. While in α -mode the discharge covers the whole electrode area, in γ -mode the discharge area is significantly smaller and very localised. Due to the smaller size, a power density increase of up to two orders of magnitude can be observed [Yang05a]. This discharge mode leads to a heating up of the discharge (and the effluent) and might alter the electrodes' surface, which has to be avoided. When decreasing the power at point C in the VI-characteristic, the discharge remains in γ -mode, the current decreases while the voltage remains constant. At point D, the discharge reverts to α -mode, reaching point E. At further decrease of the RF-power,

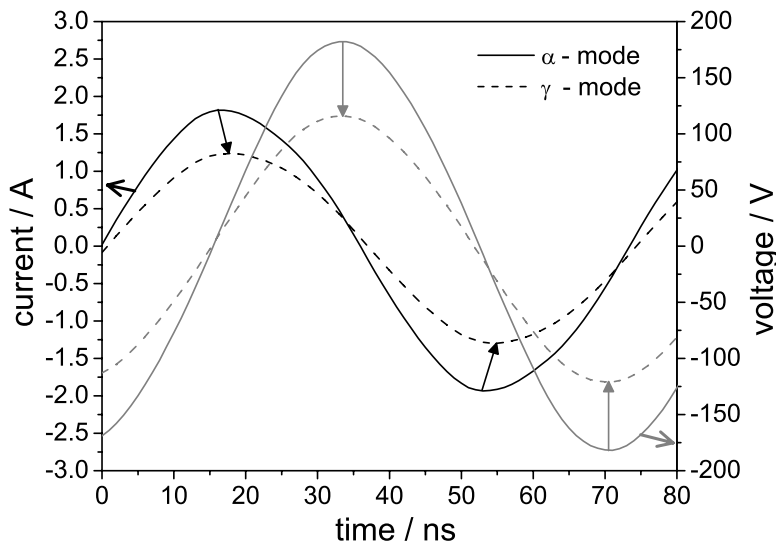


Figure 3.9: Transition
from α - to γ -mode ob-
served in the phase shift
of the current to voltage
signal

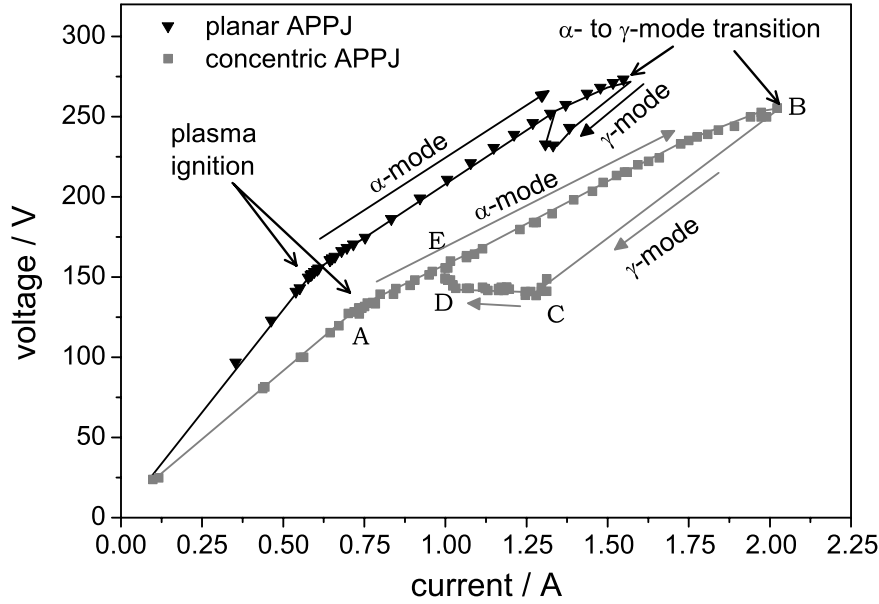


Figure 3.10: Comparing VI-characteristic of concentric APPJ and planar APPJ

the original VI-characteristic down to point A is traced. Increasing the voltage at point E results in the original progression from point E over B and C to D.

3.3.3 Discharge of Planar APPJ versus Concentric APPJ

Figure 3.10 shows that concentric version and planar version of the APPJ exhibit the same characteristic progression of discharge current and voltage. The absolute position of the curves is not accurate, due to the different matching points of the automatic matching network. Interesting to note is that the γ -mode seems to be more stable in the concentric version. To recover to α -mode, the RF-power has to be reduced much further than for the planar jet. This can be explained by the electric field enhancement at the inner (smaller) electrode in the concentric setup, stabilising the arc-like γ -mode discharge.

3.3.4 Operation in Helium and in Argon

Figures 3.11 and 3.12 show exemplary optical emission spectra of the APPJ operated in air with helium feed gas, and with argon feed gas. In the argon discharge, the overall plasma intensity in the visual spectral region is much brighter, as measurements of the spectrograph's zeroth order prove.

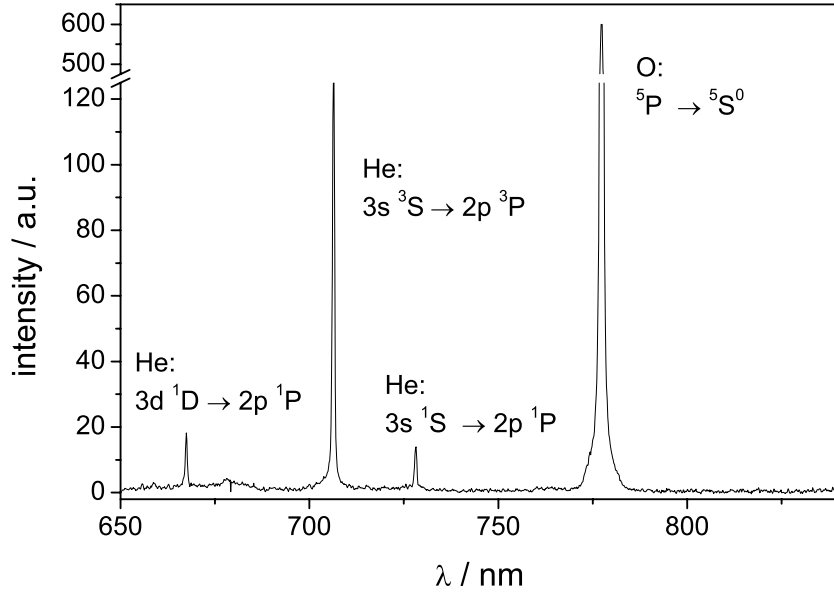


Figure 3.11: OES on the helium discharge with 0.25 vol% O₂-admixture

When operated in argon, the APPJ does not self-ignite in α -mode, so that an ignition cycle is necessary. The argon jet can be ignited by a separate plasma discharge, such as, for example, a spark generator, which is held in front of the nozzle

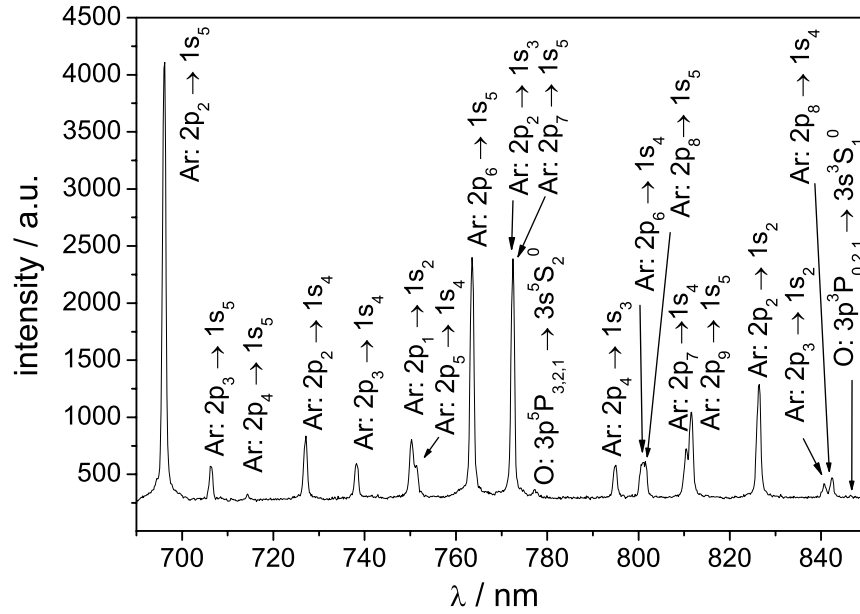


Figure 3.12: OES on the argon discharge showing the main observable visual emission lines. Level information from [Boffard04], [Stüttzle06], and [Norlen73].

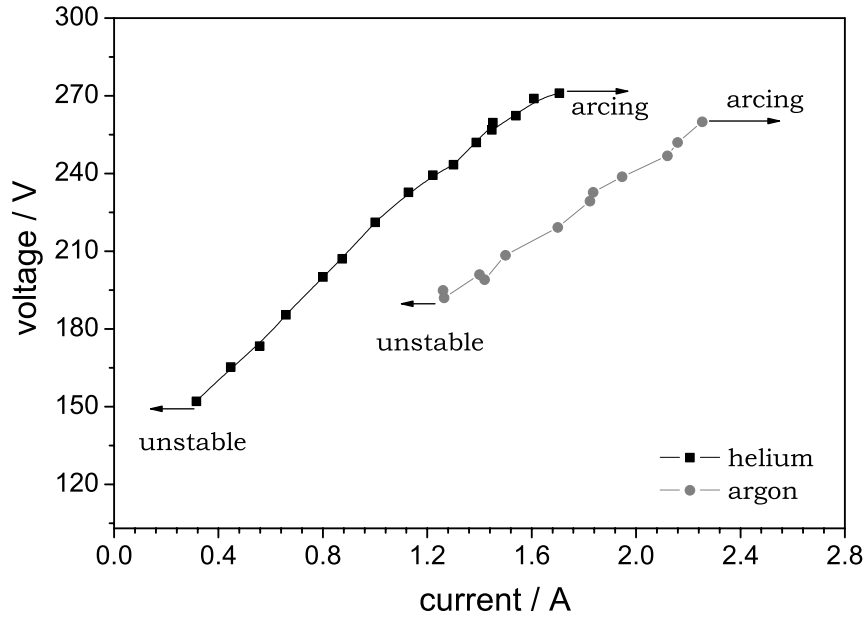


Figure 3.13: VI-characteristic of the concentric APPJ operated in helium and in argon respectively [Wang03]

of the jet. The disadvantage of this method is a possible damage imposed on the electrodes. Alternatively, the APPJ can be ignited using helium feed gas with a small admixture of argon which is then gradually increased. Unfortunately, the matching points of the matching unit differ significantly for the helium and the argon discharge so that during the transition from helium to argon discharge, α - to γ -mode transition can occur. Due to the complex ignition procedure of an argon glow discharge, a homogeneous electrode surface is vital.

In the VI-characteristic (figure 3.13) of the concentric jet operated in helium and in argon it can be observed that the discharge is stable over a wider range in helium [Wang03]. The α -mode operating regime is much smaller for the argon discharge, which is, however, operated at higher currents before transforming into a γ -mode discharge. It can also be seen that the breakdown voltage for argon is higher than for helium.

(V)UV-spectra of the discharge operated in helium (figure 3.14) and operated in argon (figure 3.15) with varying O_2 -admixture give information about the molecular and atomic species present in the plasma. For these OES-measurements, the APPJ is pointed directly towards the entrance slit of a monochromator, which is sealed with an MgF_2 -window. MgF_2 is transparent down to the vacuum ultraviolet. The monochromator is evacuated and the emitted radiation is recorded with a photomul-

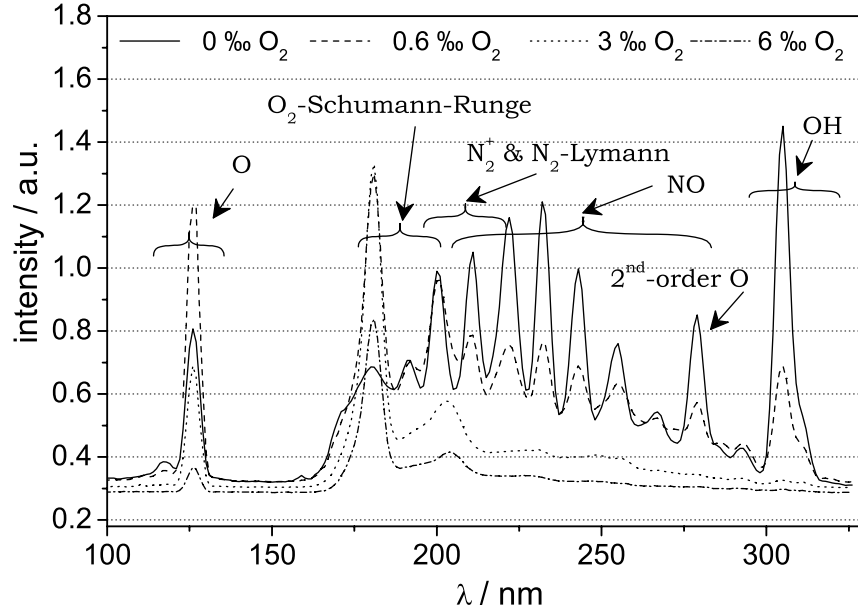


Figure 3.14: OES on the helium discharge

tiplier (EMI G-26H315 with a CsTe-photocathode). A schematic of the experimental setup for the planar APPJ and a detailed description is given in chapter 4.2.2 and in figure 4.14.

At 130 nm the OI-transition line from $^3S \rightarrow ^3P$ can be observed in both spectra. The upper state of this transition lies at about 9.5 eV. With rising oxygen admixture, the relative intensity of this line increases. In the argon spectrum (figure 3.15) along with the oxygen line an overlying peak of the argon excimer line, also peaked at 130 nm, can be observed. Due to a rapid change of the transmittance of the MgF_2 -window between 125 and 130 nm (53 % and 60 %, respectively), the actual peak might be at slightly shorter wavelength, as reported for this emission line in [Schoenbach97]. This uncertainty is reflected in data of other groups, who report the maximum argon excimer emission in the range of 126 to 130 nm [Kogelschatz90, Gellert91, Rhodes74]. Admixture of oxygen to the discharge reduces the high energy tail of the electron energy distribution due to electron impact excitation and dissociation of the oxygen [Müller97]. The dissociation of oxygen requires energy, now lost for noble gas excitation. This can clearly be seen in figure 3.15, where the argon excimer radiation at 130 nm diminishes with rising O_2 -admixture. The energy necessary for this excitation by electrons is ~ 15 eV [Schoenbach97]. The excitation cross section for many oxygen states lies exactly in this energy regime [Lieberman94], p. 253 f. Although

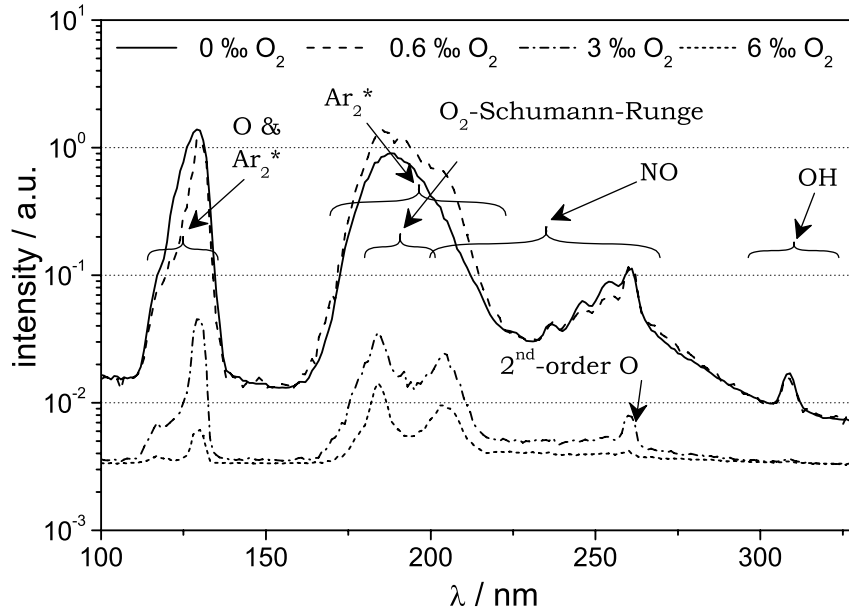


Figure 3.15: OES on the argon discharge

the processes in an oxygen RF-discharge are very complex, the presence of argon excimer emission indicates the presence of high energy electrons [Schoenbach97].

At 180nm in both spectra (helium and argon) the Schumann-Runge band of molecular oxygen can be seen. In the same way as for the OI-line at 130 nm, the intensity of the 180 nm line rises with increasing O₂-admixture.

Since the APPJ is operated at ambient conditions, many features in the (V)UV-spectra of both discharges can be attributed to atmospheric species, being either excited directly at the nozzle, or being introduced by feed gas impurities, or by back diffusion of atmosphere into the discharge as reported by [Sun07]. The periodic bands starting around 190 nm can be attributed to NO. Spectral features at around 200 nm can be attributed to N₂⁺ and the N₂-Lyman band. At around 310 nm the OH-emission band of the A ²Σ⁺ → X ²Π transition is detected.

Optical emission spectroscopy in the visible spectral range shows similar results to the ones gained from OES in the (V)UV-spectral range. With increasing molecular oxygen admixture the intensity of helium emission lines decreases, whereas the intensity of the atomic oxygen lines increases (see figure 3.16), while the total emission intensity decreases.

Measurements of the electric signals show a phase shift between current and voltage signal (see figure 3.17). When molecular oxygen is added to the discharge,

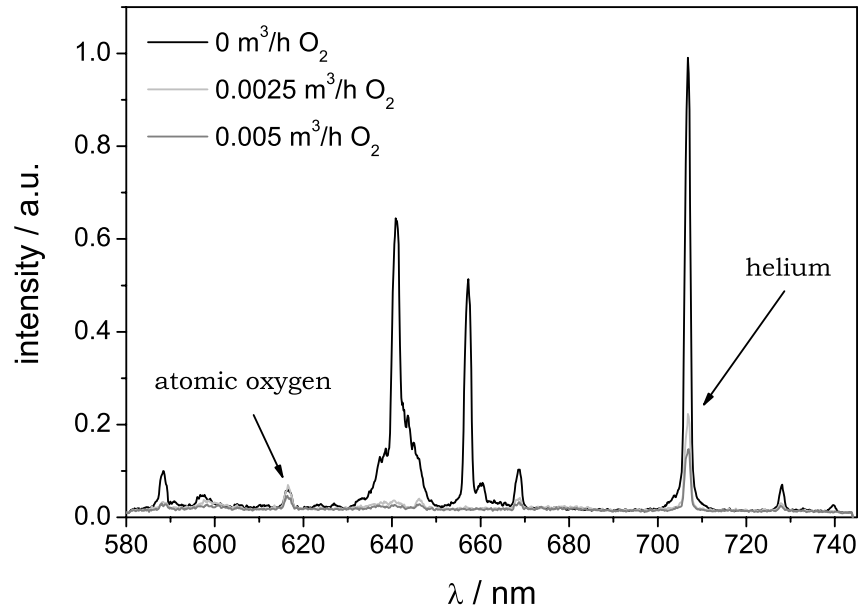


Figure 3.16: OES on the helium discharge as a function of O_2 -admixture

the capacitive part of the impedance increases, observable in a larger phase between voltage and current. According to an electric circuit model of the discharge [Moon06, Shi03, Yang05a, Raizer95], consisting of a resistor representing the core plasma, and

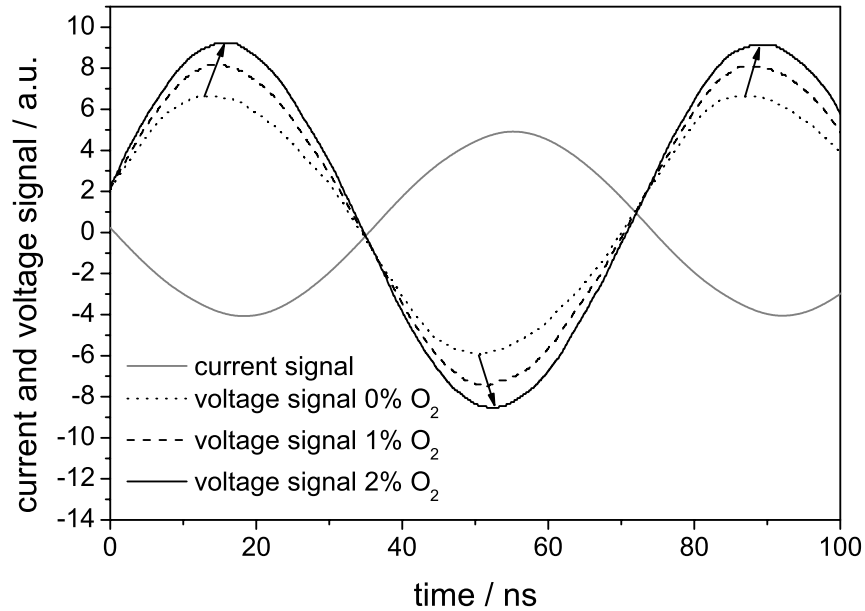


Figure 3.17: Current and voltage signal of the helium discharge as a function of O_2 -admixture

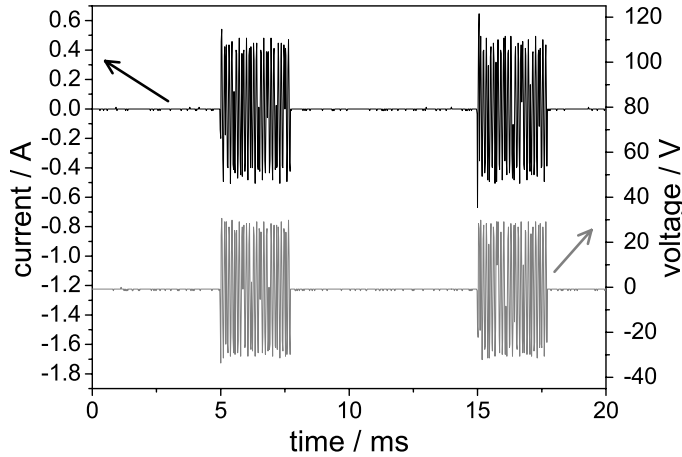


Figure 3.18: APPJ operated in pulsed mode with $2\text{ m}^3\text{h}^{-1}$ helium at 10 Watt

capacitors representing the plasma sheath's capacitances, it can be concluded from the current and voltage signal that the plasma sheaths' thickness decreases with molecular oxygen admixture. A more detailed view on the discharge region will be taken in future investigations at the Center for Plasma Science and Technology of the Ruhr-University Bochum².

3.3.5 Pulsed Operation Mode

In this study, the APPJ was successfully operated in a pulsed discharge mode in helium (see figure 3.18). This operation mode is useful especially for applications where a low power input and a low gas temperature are crucial. Reducing the power input into the discharge by pulsing results in a lower gas temperature, while it does not change the peak to peak voltage and current, thus the plasma chemistry can be kept constant. This mode will be essential for future diagnostic studies of fundamental plasma processes such as breakdown mechanisms.

Due to the complicated plasma initiation (see chapter 3.3.4), pulsing of the discharge in argon is prohibited. However, the APPJ was successfully operated in argon in a beat mode, where the RF-power self-modulates (see figure 3.19). This mode might prove helpful in future plasma diagnostics on the discharge.

²Institute for Experimental Physics II, Ruhr-University Bochum – Prof. Dr. J. Winter / Dr. V. Schulz-von der Gathen (www.ep2.ruhr-uni-bochum.de).

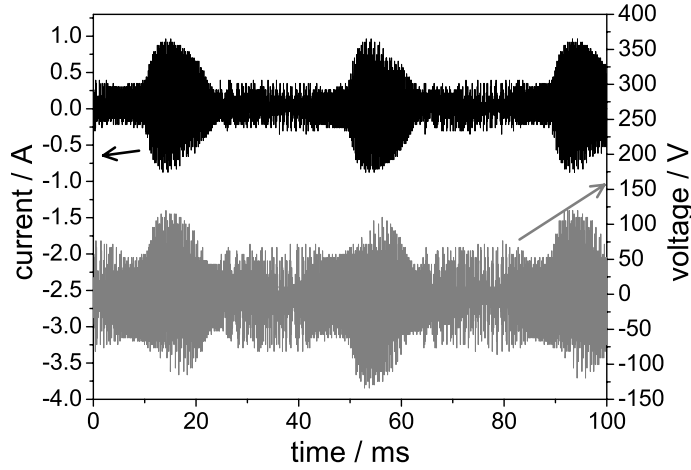


Figure 3.19: APPJ operated in beat mode with $2\text{ m}^3\text{h}^{-1}$ argon at 40 Watt

3.4 Characterisation of the Effluent

Prior to detailed studies of the APPJ's effluent in chapter 4 and 5 of this work, in this chapter preliminary investigations such as temperature and optical emission spectroscopic measurements on the APPJ operated with helium/oxygen feed gas are described.

3.4.1 Effluent of Planar APPJ versus Concentric APPJ

A temperature map of the concentric APPJ recorded with a thermocouple shows the jet's effluent to extend up to several centimetres distance from the nozzle (see figure 3.20). The thermocouple used here is a K-type thermocouple of submillimetre

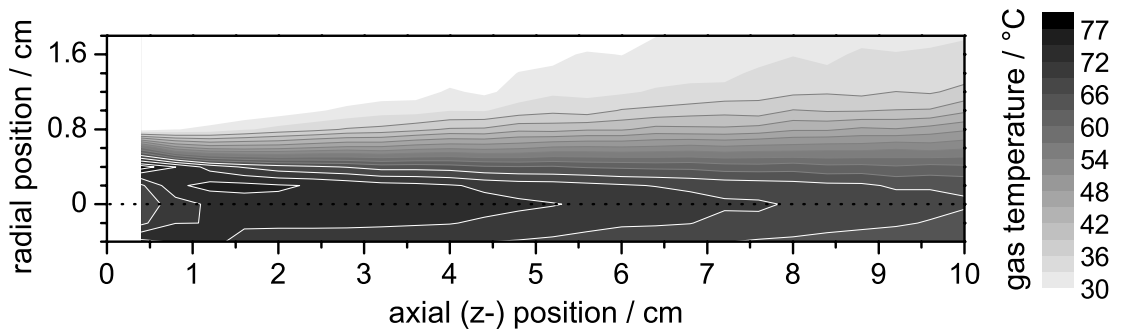


Figure 3.20: Temperature map of the effluent of the concentric APPJ operated at 150 Watt RF-power, a helium gas flux of $2\text{ m}^3/\text{h}$, and 0.5 vol% O_2 -admixture [Niemi07]

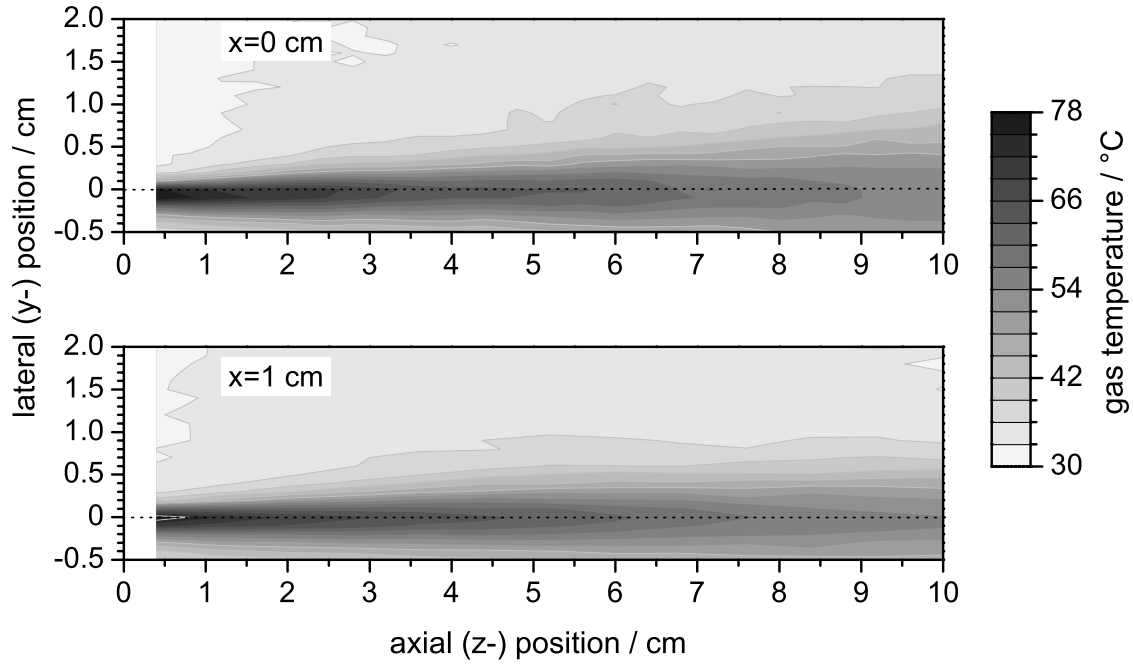


Figure 3.21: Temperature map of the effluent of the planar APPJ at two different positions of the jet's discharge gap. The jet is operated at 150 Watt RF-power, a helium gas flux of $2\text{ m}^3/\text{h}$, and 0.5 vol% O_2 -admixture.

dimensions and it is operated ungrounded. It is inserted through an inclined top port (45° with respect to the chamber axis, and perpendicular to the direction of the lateral displacement of the jet); the cable connection to the thermocouple is guided in a quartz glass tube except for the last 4 cm. In this configuration, the perturbation of the gas flow is minimal. Indications for an interference by the RF-field were not found [Niemi04]. The map is measured with the APPJ operated in a recipient with a controlled helium atmosphere at 1000 mbar. The effluent is very confined and the temperature is below 80°C .

The planar APPJ exhibits similar features: An extension of the effluent for several centimetres, and a confined flow can be observed. Two temperature maps (figure 3.21) taken at different x-positions of the jet's nozzle show the homogeneity of the planar APPJ's effluent over the length of the discharge gap.

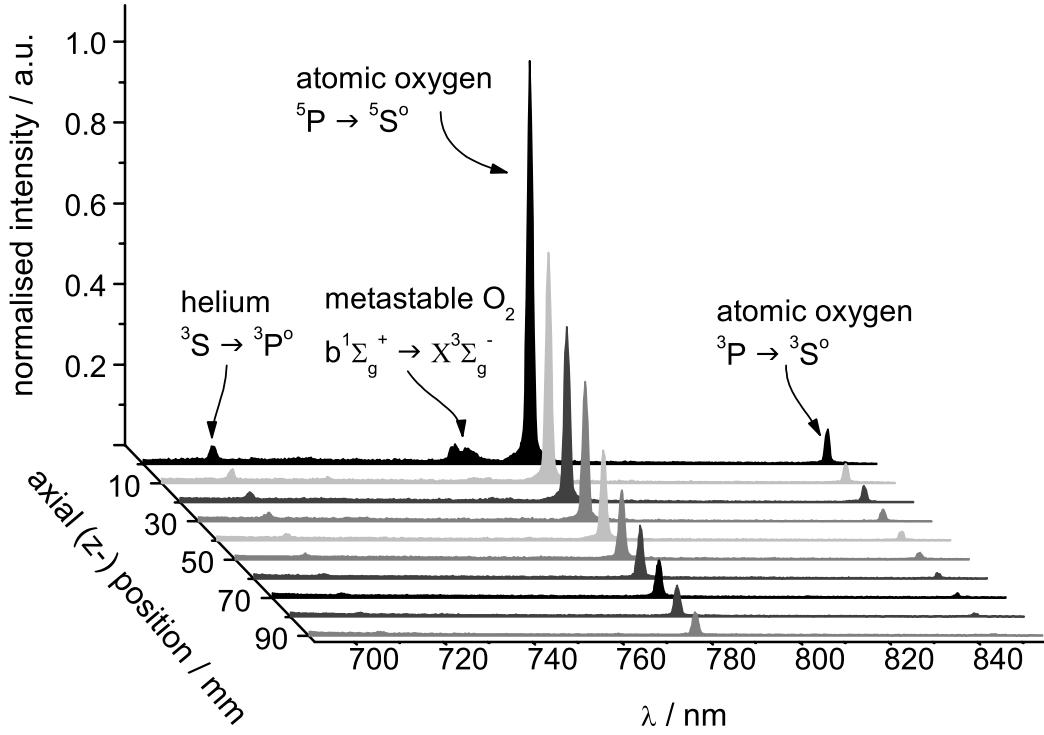


Figure 3.22: Optical emission spectra as a function of distance (z) to the jet's nozzle

3.4.2 OES of the Effluent

Optical emission spectroscopy is applied to receive first information about the APPJ's effluent. The spectra are recorded with the setup as described in chapter 2.1 and depicted in figure 2.2. The spectra are measured as a function of distance to the nozzle. The line of sight is perpendicular to the gas flow and parallel to the discharge gap. Figure 3.22 shows emission lines of the helium transition $^3S \rightarrow ^3P^0$ at 706 nm and of the atomic oxygen transitions $^5P \rightarrow ^5S^0$ at 777 nm and $^3P \rightarrow ^3S^0$ at 844 nm. Directly at the nozzle (axial position $z = 0$ mm), the emission band of singlet metastable molecular oxygen at around 759 and 764 nm can be detected. Very remarkable about these measurements is that still at 10 cm distance to the nozzle excited atomic oxygen states are present. At a gas flow rate of $1 \text{ m}^3/\text{h}$ the mean gas velocity is about 9 m/s. At this gas velocity it is impossible for excited atomic oxygen states – with a natural lifetime³ of $\sim 30 \text{ ns}$ – to reach a distance of 10 cm. Thus, an

³At atmospheric pressure the lifetime of excited atomic oxygen states is even shorter due to quenching processes.

energy transport from the APPJ's discharge region to the effluent, responsible for generation of excited atomic oxygen this far into the effluent, has to be presumed.

In the following, the atomic oxygen generation and destruction mechanisms in the effluent as well as the mechanisms for an energy transport from the discharge region into the effluent will be examined. Since the results from OES-measurements indicate ground state atomic oxygen to be present even at several centimetres distance to the nozzle, in chapter 4 of this work, the atomic oxygen ground state density in the APPJ's effluent will be determined by two-photon absorption laser induced fluorescence (TALIF) spectroscopy measurements. Furthermore, the mechanisms leading not only to generation but also to excitation of atomic oxygen will be investigated.

Chapter 4

Oxygen Radical Formation Processes in the APPJ's Effluent

The present study aims at a better understanding of atomic oxygen production and annihilation processes in the APPJ's effluent. Atomic oxygen is essential for most atmospheric pressure plasma surface treatment applications. By optical emission spectroscopic (OES) measurements, described in the previous chapter, the occurrence of excited atomic oxygen in the effluent was detected. From this, it can be presumed that a greater amount of ground state atomic oxygen is to be found in the effluent still at a considerable distance from the jet's nozzle.

For the first time, therefore, the absolute atomic oxygen ground state density in the effluent of the planar APPJ will be experimentally determined: The density distribution is measured by two-photon absorption laser induced fluorescence (TALIF) spectroscopy. These TALIF-measurements are calibrated with separate TALIF-measurements in xenon. Furthermore, the ozone density in the effluent is determined by UV-absorption measurements of the Hg-line at 253 nm. (V)UV-OES down to 110 nm and OES on metastable molecular oxygen in the visual range are performed. Following these investigations, the energy transport from the APPJ's discharge region into the effluent, responsible for a generation of excited oxygen atoms outside the discharge, is investigated by comparing results of (V)UV-OES and radical density measurements in the effluent (O , O_3 , $\text{O}_2(\text{b}^1\Sigma_g^+)$) to chemical model calculations, also considering $\text{O}_2(\text{a}^1\Delta_g)$.

4.1 Atomic Oxygen Ground State Density in the Effluent

In the following, absolute atomic oxygen ground state density in the APPJ's effluent is measured space resolved by two-photon absorption laser induced fluorescence (TALIF) spectroscopy. These TALIF-measurements are calibrated with separate TALIF-measurements in xenon.

4.1.1 Experimental Setup for Two-Photon Absorption Laser Induced Fluorescence (TALIF) Spectroscopy

For space resolved TALIF-measurements the APPJ is placed on an x-y-z- φ manipulator in the centre of a vacuum recipient that allows three-dimensional movement with respect to the fixed optical diagnostic beam. The recipient is 45 cm high and has a diameter of 51 cm, its purpose is to provide controlled operating conditions regarding the atmosphere constitution and the gas flux conditions. The experimental setup is shown in figure 4.1. All connections inside the vacuum chamber are designed flexible, to allow for the APPJ to be moved inside the chamber. The manipulator stage provides a moving range of the jet of ~ 110 mm in axial direction and ~ 37 mm in both lateral directions. The jet can be rotated by 360° , provided the supply lines permit this.

The chamber's pumping system, consisting of an oil free turbomolecular pump and a membrane fore pump, can be shut off by a plate valve. Cooling water and gas connections of the APPJ are connected to feed throughs in the base flange of the recipient. RF-power connection is accomplished via an electric feed through at the side of the recipient, with the recipient serving as common ground. The gas flux is controlled by flowrators.

The noble gas flux ranges up to $4\text{ m}^3\text{h}^{-1}$. The flux of the oxygen admixture can be adjusted by two different flowrators, one ranging up to $0.2\text{ m}^3\text{h}^{-1}$, the other ranging up to $1\text{ m}^3\text{h}^{-1}$, guaranteeing a wide range of adjustable gas flux and a precise adjustment in regimes of low oxygen flux. The gas is extracted via a large flange at the top of the vacuum chamber, which is connected to the laboratory exhaust. Prior to the TALIF-measurements, the recipient is pumped down to several 10^{-4} Pa, subsequently the pumping system is shut off by the plate valve and the recipient is filled with one atmosphere of noble gas.

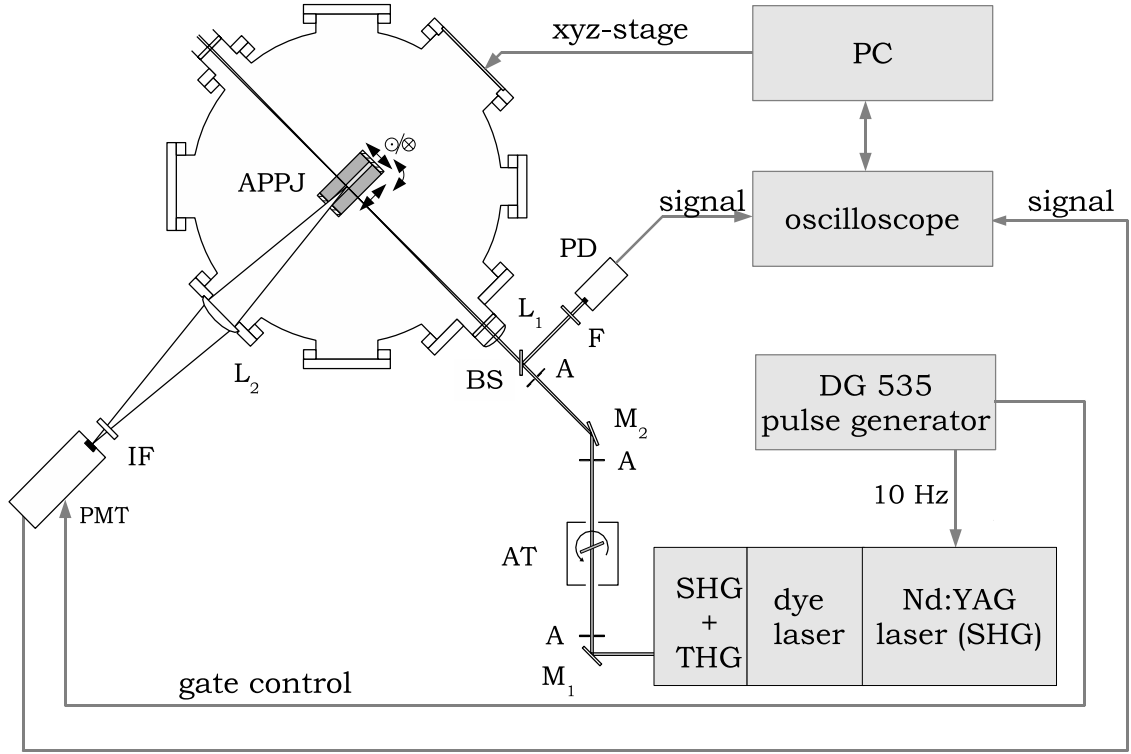


Figure 4.1: TALIF setup

For two-photon excitation of oxygen and xenon (xenon is used for calibration of the TALIF-measurements, see chapter 4.1.2), UV-laser radiation is required. A UV-laser beam is guided into the recipient by two dielectric mirrors M_1 and M_2 . The three apertures A ensure a fixed size and positioning of the laser beam and reduce stray light. The attenuator AT consists of a Suprasil plate which is coated with a thin dielectric layer. The transmission capability of the dielectric coating strongly depends on the incident angle of the laser beam. The intensity of the laser beam can be adjusted by setting the attenuator at a certain angle with respect to the beam. The attenuator's angle is set via a computer controlled stepping motor device. The lateral off-set and change in direction of the beam can be neglected, since the total working range of the attenuator lies within 6° .

A beam splitter BS guides one part of the laser beam onto a fast UV-photo diode PD to monitor the actual laser output energy. Stray signals are suppressed by filter F . The transmitted part of the laser beam is focused by the cylindrical lens L_1 (Suprasil, $f = 32$ cm) onto the centre of the recipient, where the APPJ is placed. The

laser beam exits the recipient through a Suprasil window at the opposite side, fixed at the Brewster angle, to prevent reflection and stray radiation inside the chamber. The laser beam ends in a beam dump outside the recipient. The fluorescent radiation produced by the UV-laser beam is focused on a red sensitive photomultiplier PMT (Burle C31034A, modified for pulsed operation) by lens L_2 (BK7, $f=12.5$ cm, and $\varnothing=8.7$ cm). An interference filter IF ($\lambda_0=842$ nm, $\lambda_{FWHM}=19$ nm) reduces stray light and plasma radiation onto the photomultiplier.

The trigger for the 10 Hz laser repetition frequency is provided by a DG535 digital delay/pulse generator (Scientific Instruments). It triggers a ND:YAG laser's flash lamps and the Q-switch, as well as the gate of the photomultiplier. The fluorescence radiation and the reference signal of the fast photo diode are recorded simultaneously with a digital storage oscilloscope (Tektronix TDS 380, 400 MHz, $2\text{ GS}\cdot\text{s}^{-1}$) and stored in a PC, which also controls the dye laser wavelength, the laser beam attenuation, and the positioning of the manipulator stage.

In order to generate the UV-radiation, the dye laser (Powerlite 8000, Continuum) is pumped by the frequency doubled Nd:YAG laser (ND6000, Continuum) at a wavelength of $\lambda=532$ nm. The Nd:YAG laser is operated at a reduced output energy of 400 mJ at a repetition rate of 10 Hz and a pulse length of 6 ns. The dye laser is equipped with dual 2400 grooves mm^{-1} gratings, and the dye consists of a mixture¹ of Pyridin1 and DCM in methanol (for a detailed overview of dyes and solvents see [Brackmann94]).

The desired output wavelength of the dye laser lies between 672 and 677 nm in the centre of the dye mixture's broad tuning curve (see figure 4.2). The dye laser radiation is frequency doubled through second harmonic generation (SHG) by a KD*P-crystal (KD_2PO_4) and is subsequently tripled (third harmonic generation, THG) by a BBO-crystal ($\beta\text{-Ba}_2\text{B}_4$). The crystals are tracked automatically during scanning of the laser wavelength. The resulting UV-laser radiation with tunable wavelengths between 224 and 226 nm has a pulse length of 5 ns at an energy of about 4 mJ. As part of the start-up procedure, the dye laser performs a wavelength calibration process with a wavelength accuracy of ± 0.002 nm.

¹The used dyes are $\text{C}_{19}\text{H}_{17}\text{N}_3\text{O}$ (DCM) and $\text{C}_{19}\text{H}_{23}\text{N}_2\text{O}_4\text{Cl}$ (Pyridin 1).

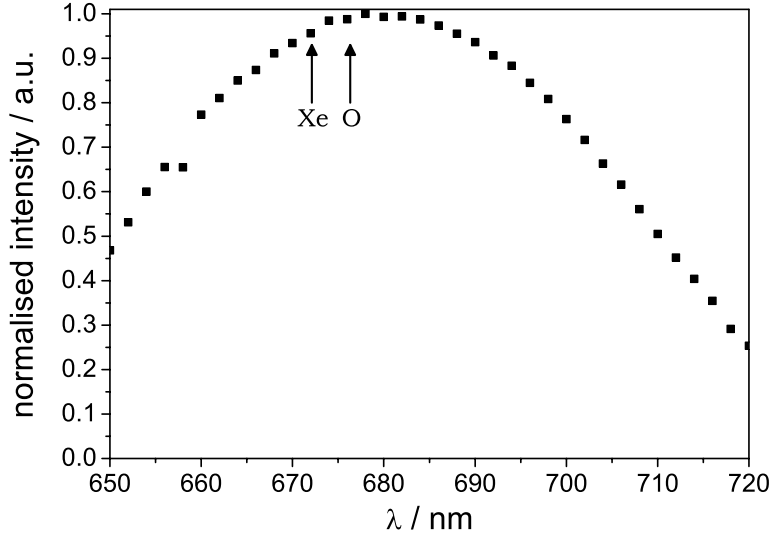


Figure 4.2: Tuning curve of the dye laser. The dye consists of a mixture of DCM and Pyridin 1 dissolved in methanol. Arrows indicate the dye-laser wavelengths relevant for the present investigations on xenon and atomic oxygen.

4.1.2 TALIF-Calibration with Xenon

Measurement of absolute values for ground state atom densities by TALIF requires a signal calibration. The calibration method used in this work is based on noble gas TALIF-measurements, developed at the University of Essen [Goehlich98]. Noble gas calibration, in contrast to other common TALIF-calibrations, does not require a change of experimental setup.

It is vital that for excitation of the ground state atoms the resonance transition of the reference species is sufficiently close to the resonance transition of the probed species, so that identical excitation conditions, concerning the spacial, spectral, and temporal intensity distribution of the laser radiation, can be assumed. Furthermore, the parameter regime the measurements are performed in has to be chosen so that the signal intensity as a function of laser energy obeys the same (quadratic) scaling laws for both the reference resonance transition and the probed resonance transition. The excitation must not be subject to saturation. When these conditions are met, the unknown atomic ground state density n_x can then be derived from the reference gas density n_R by:

$$n_x = \frac{T_R \eta_R}{T_X \eta_X} \cdot \frac{\sigma_R^{(2)}}{\sigma_X^{(2)}} \cdot \frac{a_R}{a_X} \cdot \frac{S_X}{S_R} \cdot n_R \quad (4.1)$$

with the fluorescence signal S (wavelength integrated and normalised to the squared laser pulse energy), the two-photon excitation cross sections $\sigma^{(2)}$, the branching ratio a of the observed fluorescence transition, and the optical parameters of the detection

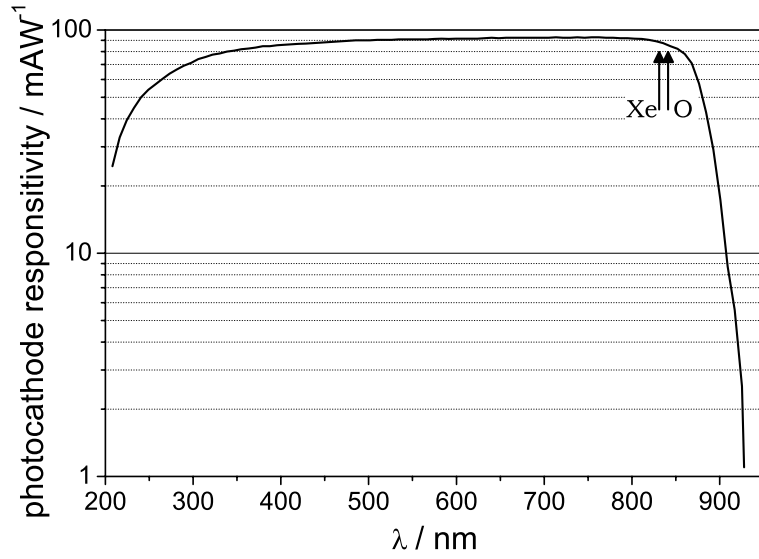


Figure 4.3: Photocathode responsivity of Burle C31034A photomultiplier tube [Burle Industries Inc.07]. Arrows indicate the wavelengths of the investigated fluorescence radiation for xenon and atomic oxygen.

system (transmission of the optics T and quantum efficiency of the photomultiplier η (see figure 4.3) for the respective wavelength of the fluorescence radiation). [Döbele05]

A new two-photon excitation scheme of xenon proposed by Niemi and coworkers in [Niemi04] has a sufficiently close resonance transition $\text{Xe}(5p^6\ ^1S_0 \rightarrow 6p'[3/2]_2)$ to the two-photon excitation transition $\text{O}(2p^4\ ^3P_2 \rightarrow 3s\ ^3S)$ of oxygen (see figure 4.4). A major advantage of this xenon resonance transition over earlier reference resonance transitions [Goehlich98] is that the resulting fluorescence radiation spectrally is extremely close to the investigated oxygen fluorescence radiation. The conditions for

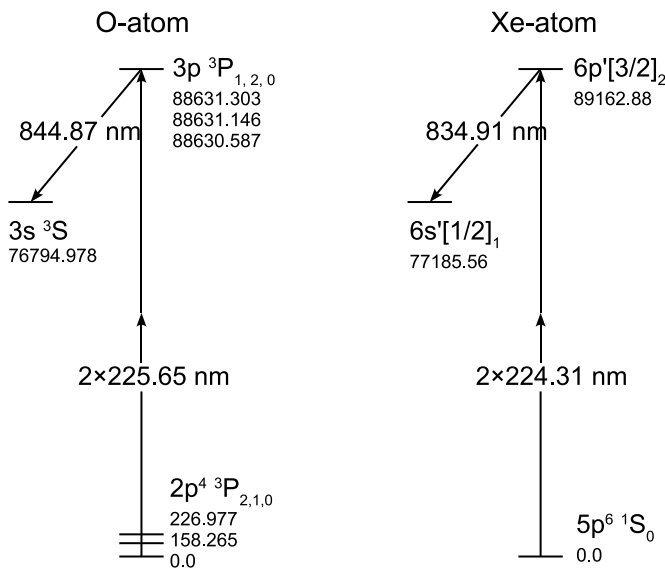


Figure 4.4: Simplified two-photon excitation schemes for atomic oxygen and xenon (energies given in cm^{-1} , J-values listed from lowest to highest energy)

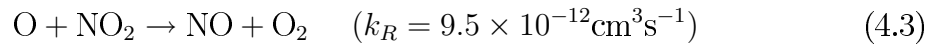
fluorescence detection are therefore almost identical, making a switching of optical components (optical filters or even the photomultiplier tube) obsolete. This means that the ratio of the optical constants $T_R\eta_R/T_X\eta_X$ is close to unity, improving the calibration accuracy.

4.1.2.1 Two-Photon Excitation Cross Section

The two-photon excitation cross section for the new xenon two-photon excitation scheme (see figure 4.4) is determined by the relation found in equation 4.1. This relation not only allows to determine the density of an atomic species at known cross section ratios, but vice versa also allows to derive cross section ratios from known atomic densities:

$$\frac{\sigma_R^{(2)}}{\sigma_X^{(2)}} = \frac{T_X\eta_X}{T_R\eta_R} \cdot \frac{a_x}{a_R} \cdot \frac{S_X}{S_R} \cdot \frac{n_R}{n_X} \quad (4.2)$$

The experiments are performed and presented in [Niemi04, Niemi05]. The procedure is as follows: First, a density of the required atomic species is generated with a so-called flow tube reactor, a commonly used microwave plasma source first described by Kaufman et al. [Kaufman58]. The atom density is then determined by the titration method, where – in the case of atomic oxygen – a known amount of NO_2 is added to the afterglow of the microwave discharge. The TALIF-signal is measured at that point in the afterglow, where the chemical reactions of O and NO_2 are assumed to be completed: For each reactive NO_2 -molecule one oxygen atom is annihilated according to reaction 4.3:



A linear decrease of the TALIF-signal with increasing titration gas flux is expected until the fluorescence signal vanishes at the so-called titration end point. Here the particle flux of the reactive titration molecules matches the particle flux of the atomic species, and the atomic density can be derived. For a detailed explanation see e.g. [Niemi03a, Niemi03b], or [Clyne79].

Figure 4.5 shows TALIF-signals of xenon and oxygen plotted against the squared laser energy [Niemi04]. The measured signals for lower laser energy clearly exhibit a quadratic dependency. The solid lines are linear fits for these signals through the zero crossing of the axes. The ratios of the slopes of the fits yield the ratio of the normalised fluorescence signals S_X/S_R . The ratio of the two-photon excitation cross

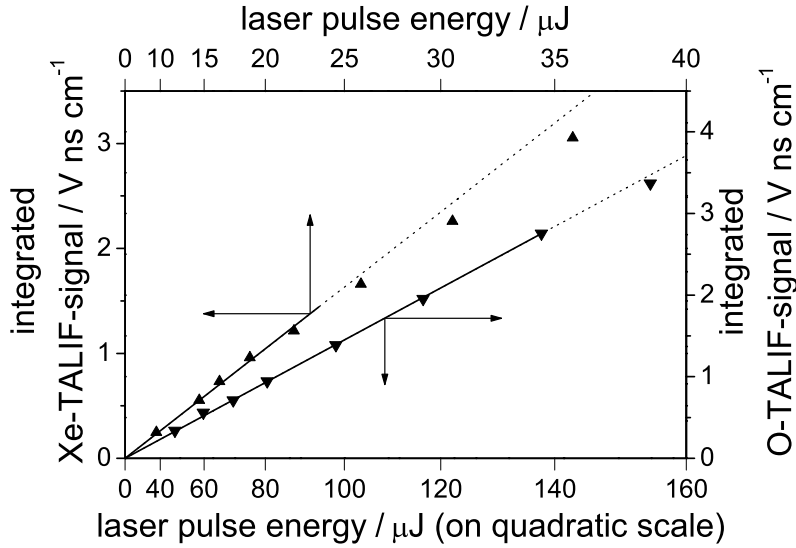


Figure 4.5: Comparison of xenon and atomic oxygen TALIF-signal dependencies [Niemi04]

section of xenon to oxygen $\sigma^{(2)}(Xe)/\sigma^{(2)}(O)$ can be determined by the measured ratio of the normalised fluorescence signals (figure 4.5) and the calibration factor in equation 4.1 – with known atomic densities, detection sensitivities for the two wavelengths (the ratio is unity in the present case), and (collisionless) branching ratios. By this a value of $\sigma^{(2)}(Xe)/\sigma^{(2)}(O) = 1.9$ is determined for the new xenon resonance transition with an estimated overall uncertainty of $\sim 20\%$.

4.1.2.2 Quenching

At atmospheric pressure, de-excitation of two-photon excited atomic states by collisional quenching needs to be taken into account, since quenching affects the branching ratio a of the observed fluorescence transition, according to:

$$a_{ik} = \frac{A_{ik}}{\sum_{k < i} A_{ik} + \sum_q k_q^i n_q} \quad (4.4)$$

where $\sum_{k < i} A_{ik}$ denotes the total spontaneous emission rate of the upper level, which is equal to its reciprocal radiative lifetime τ_i . n_q are the collision partner densities with the corresponding quenching coefficients k_q^i [Niemi07]. For a calibration of the fluorescence signal, the quenching coefficients have to be determined. In order to limit the number of quenching coefficients to be measured, the APPJ is operated in a recipient filled with one atmosphere of helium, reducing the collision partners to only helium and (atomic and molecular) oxygen. For the xenon calibration additionally the self-quenching coefficient of xenon needs to be determined.

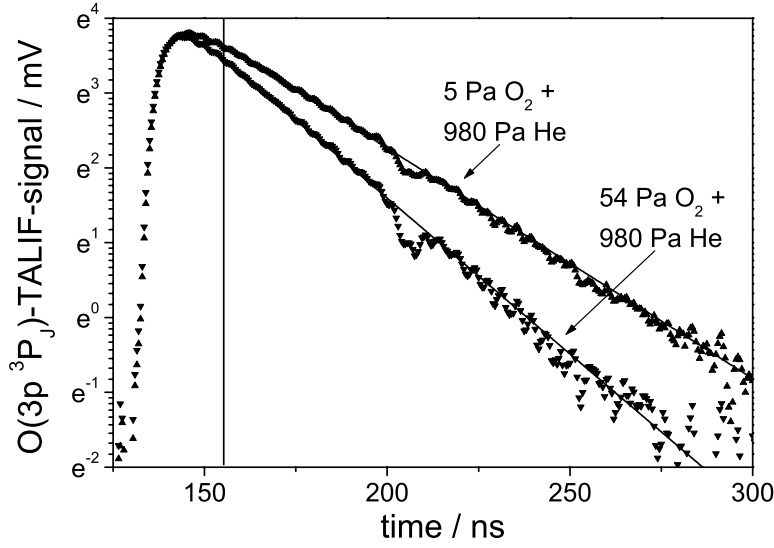


Figure 4.6: Time resolved $O(3p\ ^3P_J)$ -TALIF-signal obtained with different O_2 -admixtures [Niemi04]. The vertical line indicates the beginning of the exponential decay 10 ns after termination of the laser pulse. The dip at ~ 200 ns is an artefact of the PMT response.

For measurement of the quenching coefficients and the radiative lifetimes of the two-photon excited oxygen atoms, O-atoms are generated in the flow tube reactor (see above chapter) at a constant feed gas flux, while a variable flux of an additional quencher (helium or O_2) is introduced downstream through the titration tube [Niemi04, Niemi05]. Figure 4.6 shows two exemplary photomultiplier signals with and without additional O_2 -admixture. The corresponding decay rates are derived by an unweighted exponential fitting procedure.

Figure 4.7 shows a so-called Stern-Vollmer plot of the decay rates A^* plotted versus the partial pressure of the admixed quenching gas. From the slope, the quenching

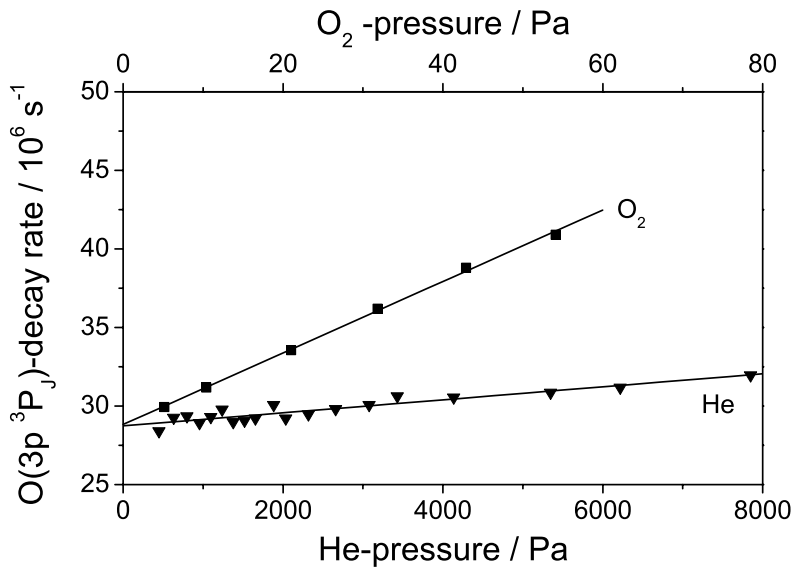


Figure 4.7: Decay rates of $O(3p\ ^3P_J)$ -fluorescence signal versus quenching gas partial pressure [Niemi04].

coefficients k are derived, and from the zero crossing the radiative lifetimes τ are deduced according to equation 4.5:

$$A^* = \frac{1}{\tau} + k_{O_2}n_{O_2} + k_{He}n_{He} \quad (4.5)$$

The values for the radiative lifetimes used for this work are 34.7 ± 1.7 ns for $O(3p^3P_J)$ and 40.8 ± 2.0 ns for $Xe(6p'[3/2]_2)$. The quenching coefficients are $9.4 \pm 0.5 \times 10^{-10} \text{ cm}^3\text{s}^{-1}$ for O_2 , $(0.017 \pm 0.002) \times 10^{-10} \text{ cm}^3\text{s}^{-1}$ for He and the self-quenching coefficient of xenon is $(3.6 \pm 0.4) \times 10^{-10} \text{ cm}^3\text{s}^{-1}$ [Niemi04]. The self-quenching coefficient for atomic oxygen needs not be taken into account, since atomic oxygen is in this case a minority species and also a rather inefficient quencher according to Dilecce et al. [Dilecce00] who derived an upper limit of $(0.82 \pm 0.4) \times 10^{-10} \text{ cm}^3\text{s}^{-1}$ for the self-quenching coefficient.

4.1.2.3 Two-Photon Excitation Line Shape Considerations

Figure 4.8 shows the two-photon excitation line profile of the $Xe(5p^6^1S_0 \rightarrow 6p'[3/2]_2)$ resonance transition. The solid line is a Voigt profile adapted to the measuring points. For the following spectral line shape analysis, numerical methods for atmospheric line by line calculations of the Voigt function [Wells99] together with a Marquart fit algorithm are applied, as used in [Niemi04, Niemi05]. A Gaussian width of 0.096 cm^{-1} , derived from the Doppler broadening of xenon at room temperature, and a Lorentzian width of 0.15 cm^{-1} results in the best fit, shown in figure 4.8. From

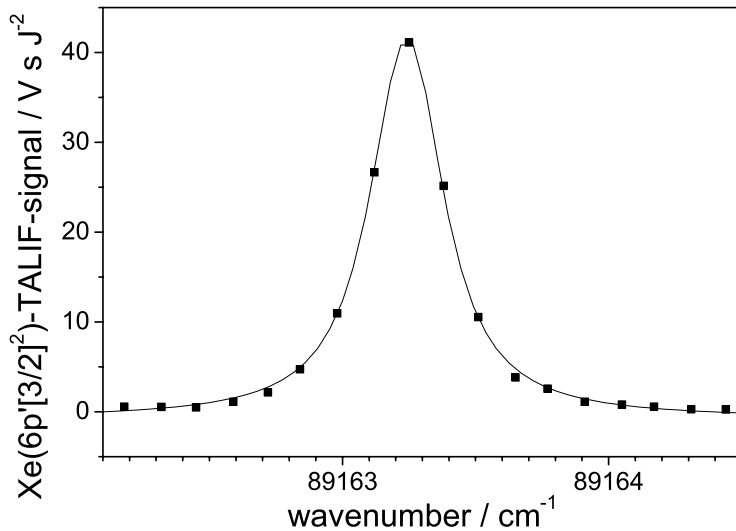


Figure 4.8: Two-photon excitation line profile of the $Xe(5p^6^1S_0 \rightarrow 6p'[3/2]_2)$ resonance transition

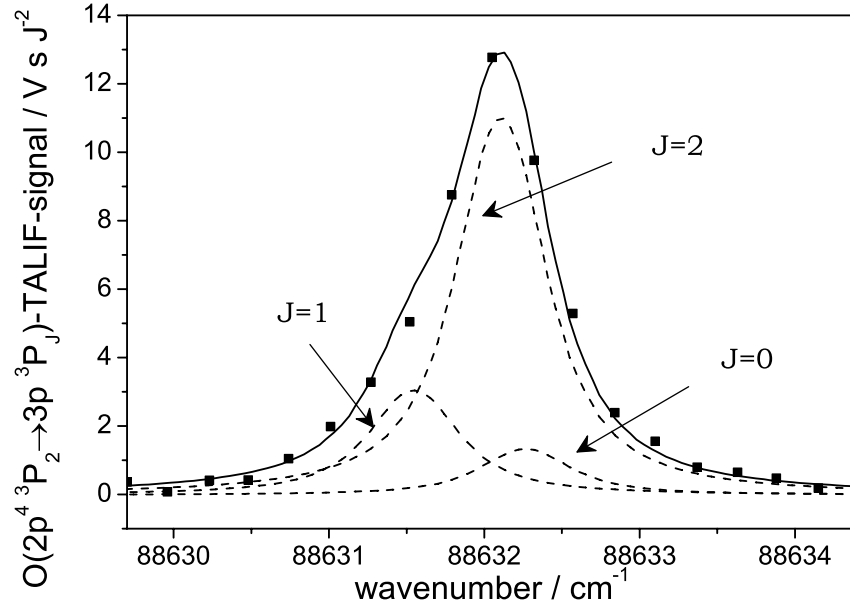


Figure 4.9: Two-photon excitation line profile of the $O(2p^4 3P_2 \rightarrow 3p^3 P_J)$ resonance transition measured in the APPJ's effluent

the good agreement between fit and measuring points, it can be concluded that the Lorentzian contribution represents the effective two-photon excitation laser line profile, resulting in a laser bandwidth of 0.75 cm^{-1} .

Figure 4.9 shows the two-photon excitation line profile of the $O(2p^4 3P_2 \rightarrow 3p^3 P_J)$ resonance transition measured in the APPJ's effluent. The black solid line is a superposition of the Voigt profiles of the three finestructure levels of the excited state. The finestructure components are adapted for their theoretical weight according to their relative cross sections (see table 4.1) and relative spectral positions. The respective

J'_{final}	J_{initial}	cross sections
0	0	0.561
1	0	
2	0	0.439
0	1	
1	1	0.671
2	1	0.329
0	2	0.088
1	2	0.198
2	2	0.714

Table 4.1: Relative cross sections for $2p^4 3P_J \rightarrow 3p^3 P_{J'}$ transition [Saxon86]

spectral lines are composed of a Gaussian contribution (Doppler width of oxygen $w_G = 0.293 \text{ cm}^{-1}$ at 343 K, measured with a thermocouple) and a Lorentzian contribution. The Lorentzian contribution with a width of 0.31 cm^{-1} is much broader than the laser line profile width derived from the xenon measurements. It can therefore be concluded that the $O(2p^4^3P_2 \rightarrow 3p^3P_J)$ resonance transition is effected by significant pressure broadening of $\sim 0.16 \text{ cm}^{-1}$ in the jet's effluent. Since the pressure broadening is due to both elastic and inelastic collision processes, no effective quenching rates can be determined from the line widths.

4.1.2.4 Temperature Corrections

The gas temperature in the effluent of the jet varies with the distance from the nozzle by up to almost 50°C (see figure 3.21). Temperature dependencies, therefore, have to be taken into account in the evaluation of the TALIF-measurements. The feed gases helium and oxygen are dominantly responsible for the strong quenching of two-photon excited oxygen atoms. From their measured room temperature quenching coefficients (see chapter 4.1.2.2) together with the temperature map in figure 3.21, the temperature corrected quenching coefficients can be determined according to:

$$k_q = \sigma_q \langle v \rangle = \sigma_q \sqrt{\frac{8k_B T_G}{\pi \mu}} \quad (4.6)$$

$\langle v \rangle$ is the mean collision velocity, k_B is the Boltzmann constant, μ the reduced mass of the colliders, and σ_q the collision cross section which generally exhibits a modest temperature dependency [Faist76].

The ground state of atomic oxygen is a triplet state. It can be resolved by TALIF-measurements, because the substantial ground state splitting of 227 cm^{-1} is considerably larger than the room temperature Doppler width (0.274 cm^{-1}). Since the ground state exhibits thermal population distribution [Niemi05], only one ground state sub-level has to be probed. The total ground state population of atomic oxygen can then be derived by considering the corresponding – temperature dependent – Boltzmann population fraction:

$$\frac{n_J}{\sum_j n_j} = \frac{(2J+1) \cdot e^{(-E_J/k_B T_G)}}{\sum_J (2J+1) \cdot e^{(-E_J/k_B T_G)}} \quad (4.7)$$

with the total angular momentum quantum number J and energy E_J . For a measure-

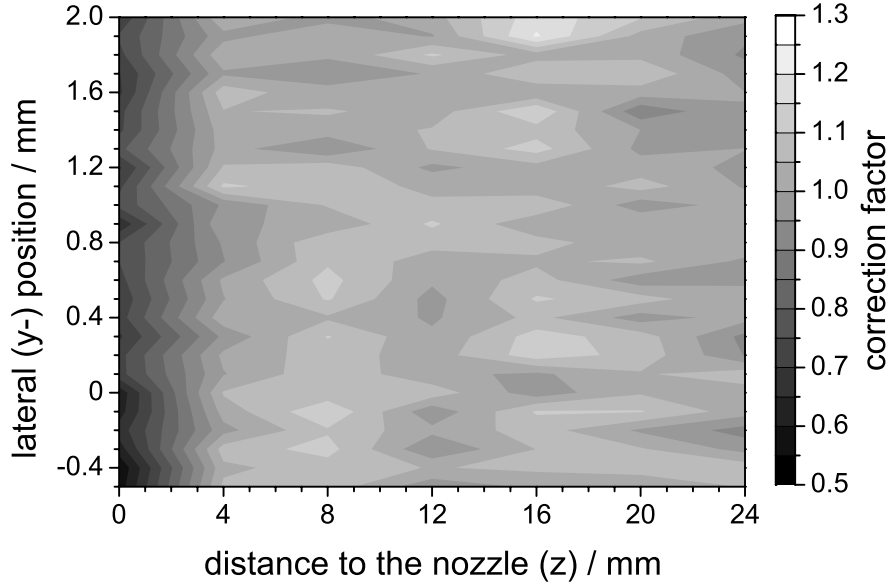


Figure 4.10: Vignetting and reflection effects of the APPJ, measured by recording a map of the TALIF-signal of the xenon transition

ment of the atomic oxygen ground state density above two temperature dependent equations need to be taken into account.

4.1.2.5 Vignetting and Reflection

The solid angle of detection is partially shadowed by the APPJ's electrodes when fluorescence is measured close to the jet's nozzle. Vignetting and reflections both influence the yield of the fluorescence radiation signal. This influence can be measured by filling the recipient, in which the APPJ is placed, with xenon to establish a homogeneous particle density.

A map of the xenon fluorescence is recorded at constant laser energy. The measurement is shown in figure 4.10. The zero position in lateral (y-) direction refers to the centre of the APPJ, the zero position in axial (z-) direction refers to the point where the laser beam is not cut off by the APPJ's nozzle. The symmetry of the xenon signal map reflects the rectangular shape of the jet. Directly at the nozzle the correction factor is 0.6, and beginning at 4mm distance from the nozzle the correction factor is one. After this point no vignetting influence of the APPJ on the fluorescence signal can be detected.

4.1.3 Atomic Oxygen Density Map of the Effluent

The absolute atomic oxygen ground state density distribution in the APPJ's effluent is determined as described in the following: First, a two-dimensional fluorescence signal map of the jet's effluent is recorded. For this, the on-resonance fluorescence signal of the $O(2p^4\ ^3P_2 \rightarrow 3p^3\ ^3P_J)$ resonance transition is measured as a function of lateral position and distance to the nozzle in 4 mm and 2 mm steps respectively. A calibration of the TALIF-measurements is performed with the $Xe(5p^6\ ^1S_0 \rightarrow 6p'[3/2]_2)$ resonance transition according to chapter 4.1.2 on-axis at 12 mm distance from the nozzle in the effluent. The spectrally and temporally integrated oxygen fluorescence signals are measured as a function of laser pulse energy, as is subsequently done for the xenon transition in a xenon filled recipient (see figure 4.11). With these two measurements and with equation 4.1 the on-axis atomic oxygen density at 12 mm distance from the nozzle is determined as $n_O = 4.1 \times 10^{15} \text{ cm}^{-3}$.

Using the measured temperature distribution of the effluent (figure 3.21), the oxygen fluorescence data recorded on-resonance can be converted to spectrally integrated data. Subsequently, the remaining corrections for collisional quenching, Boltzmann population fraction, and vignetting and reflection (see above chapters) have to be applied to all measuring points.

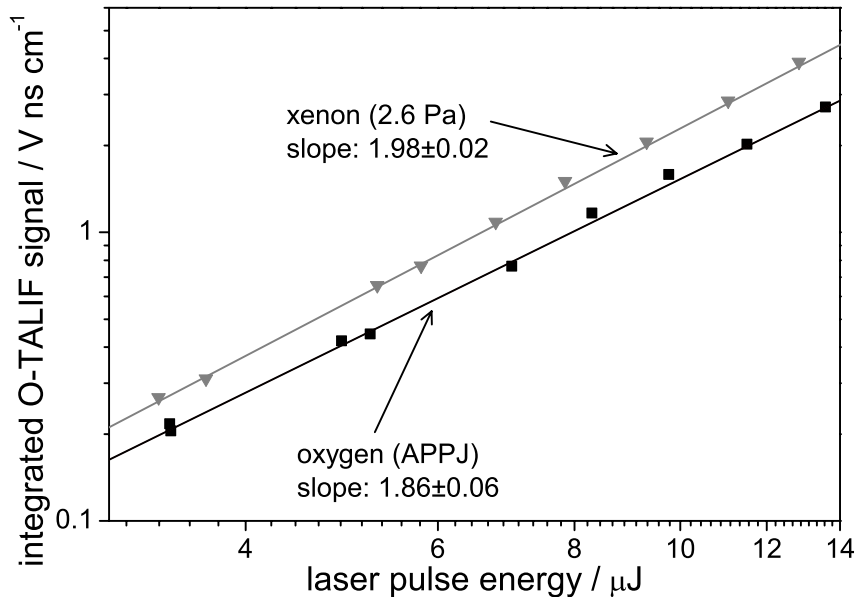


Figure 4.11: TALIF-calibration measurements. Xe- and O-TALIF-signal as a function of laser pulse energy (on a quadratic x-axis) show the unsaturated TALIF-signals.

A measurement of the oxygen resonance line at three different distances from the nozzle (12mm, 52mm, and 92mm) shows that pressure broadening is space independent. Figure 4.12 shows the resulting atomic oxygen ground state density distribution in the effluent of the APPJ for a helium flux of 2 m³/h, 0.5 vol% O₂-admixture and an RF-power of 150 Watt. The atomic oxygen ground state density is $\sim 1 \cdot 10^{16}$ cm⁻³ directly at the APPJ's nozzle. The TALIF-measurements show that at 10 cm distance from the nozzle still $\sim 1\%$ of the initial atomic oxygen density remains.

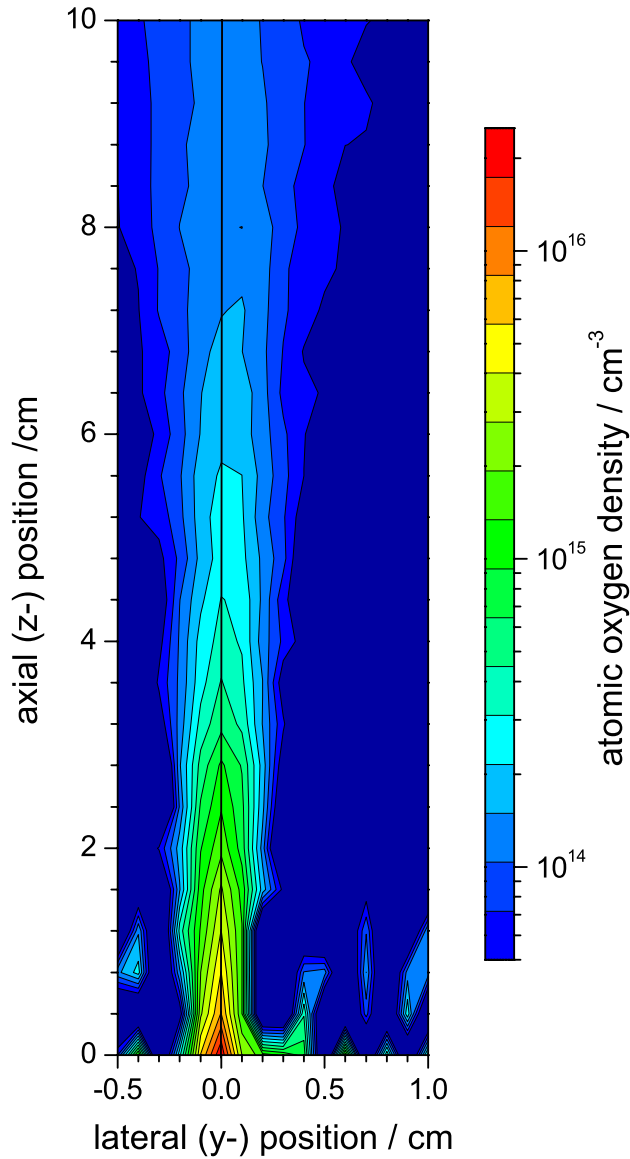


Figure 4.12: Atomic oxygen density map of the APPJ's effluent, measured perpendicular to the electrode gap at the centre of the jet. The lateral (y-) position is depicted stretched by a factor of two.

4.2 Energy Transport into the Effluent

A high density of ground state atomic oxygen in the effluent of the planar atmospheric pressure plasma jet was for the first time experimentally determined by the performed TALIF-measurements. Even at 10 cm distance from the nozzle, atomic oxygen is present. These results agree with the optical emission spectroscopic measurements described in chapter 3.4.2, which already detected excited atomic oxygen at several centimetres distance from the nozzle in the effluent. Since the excited atomic oxygen states' lifetime, however, is much too short for reaching the considerable distance of several centimetres at the given gas velocities, meaning that these excited species can only be generated outside the discharge region, this chapter will investigate mechanisms for an energy transport from the APPJ's discharge region into the effluent.

4.2.1 Possible Energy Transport Mechanisms

It is presumed that an energy transfer from the discharge is responsible for generation of excited atomic oxygen in the APPJ's effluent. The excited oxygen states from which the optical emission lines at 777 nm and at 844 nm origin (see figure 3.22) have an energy of > 10 eV. Because of their specific properties, metastable species are assumed to be suitable for an energy transport. Metastables are an excited species with a long natural lifetime, due to the fact that resonant radiative transitions into the ground state are prohibited. The majority species in the atmospheric pressure plasma jet is helium. Metastable helium atoms (He^*) carry an energy of over 19 eV, and accordingly would have more than sufficient energy for excitation of ground state atomic oxygen. Measurements at atmospheric pressure, however, show that even in a pure helium plasma, the effective He^* -lifetime is as short as $6.7 \mu\text{s}$ due to collisions with helium ground state atoms and formation of helium excimers [Kurunczi01, Tachibana05]. In the presence of impurities, e.g. N_2 , their lifetime is further reduced to $2.4 \mu\text{s}$ [Nersisyan04]. Also the presence of oxygen rapidly de-excites metastable helium states [Cardoso06], so that the effective lifetime falls to below $0.1 \mu\text{s}$ [Jeong00]. Thus, it can be concluded that helium metastables are not responsible for generation of excited atomic oxygen outside the discharge.²

Also ions and electrons are considered as possible means for an energy transport.

²Results from preliminary investigations on helium metastables were presented at the Gaseous Electronics Conference 2006 [Reuter06].

The recombination coefficient for ions and electrons at atmospheric pressure, however, is approximately $10^{-6} \text{ cm}^3 \text{ s}^{-1}$ [Biondi76, Bicchi97, Jeong00]. Thus, the ion and electron density decreases too rapidly, to have an influence on excited atomic oxygen generation in the effluent.

As can be seen in figure 3.14, high energy (V)UV-radiation is emitted from the discharge region of the APPJ. In the following, the spacial distribution of this (V)UV-radiation is measured in order to investigate, whether (V)UV-radiation generates excited atomic oxygen far outside the APPJ's discharge region.

4.2.2 (V)UV-Radiation

The significance of (V)UV-radiation as energy supply for processes in the APPJ's effluent becomes evident, when the bond energy of selected atmospheric molecules is plotted against the wavelength of radiation of that energy (see figure 4.13). The O_2 -molecule, for example, dissociates at an energy of $\geq 5.16 \text{ eV}$ [Lide00], which corresponds to a wavelength of $\lambda \leq 240 \text{ nm}$. As could already be seen from figures 3.14 and 3.15, the APPJ emits radiation at least down to 120 nm . In the following, the spacial and spectral distribution of (V)UV-radiation in the effluent is investigated.

A schematic of the VUV-optical emission spectroscopy experimental setup is shown in figure 4.14. The APPJ's effluent is directed onto an MgF_2 -window, which is placed in front of the slit of a 0.2 m monochromator (Minuteman Laboratories Inc. 302VM, grating 1200 mm^{-1}). The monochromator is evacuated to a pressure of $5 \cdot 10^{-3} \text{ Pa}$ by an oil free turbomolecular pump with a membrane fore pump.

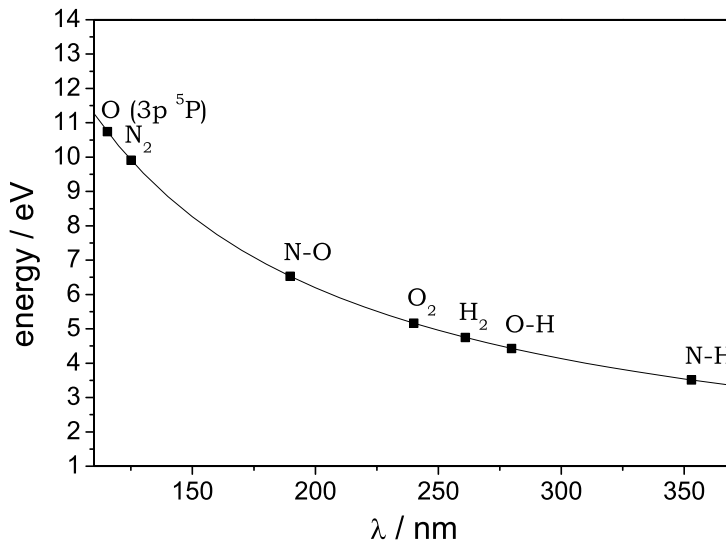


Figure 4.13: Bond energy for atmospheric molecules as a function of wavelength (bond energies from [Lide00], $\text{O}(3p^5\text{P})$ -energy state from [Moore75])

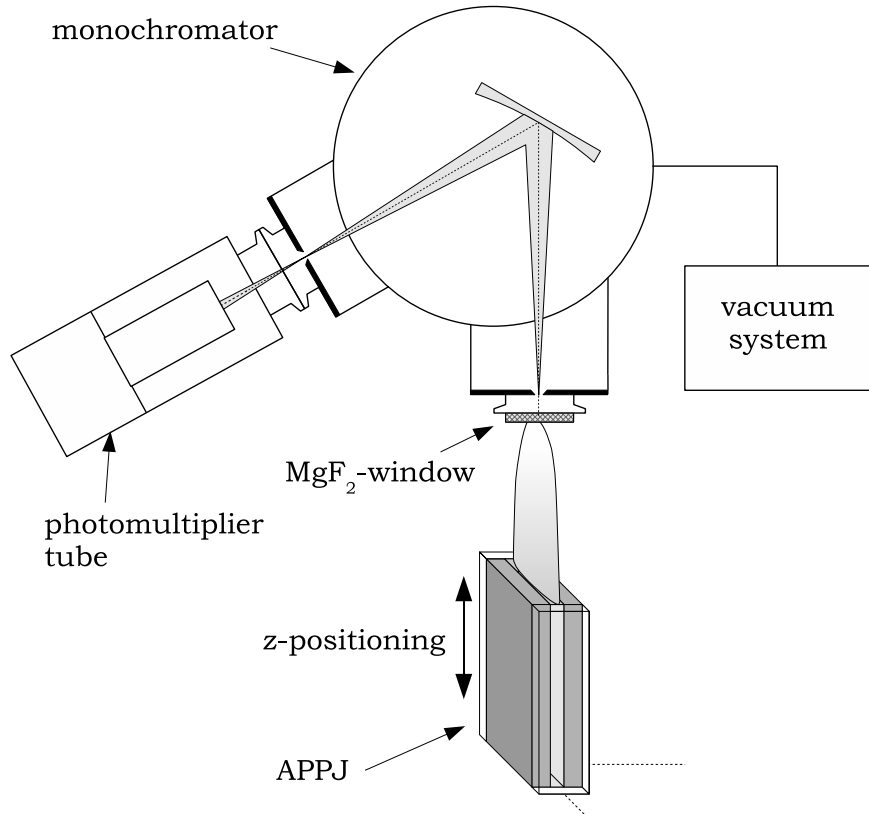


Figure 4.14: VUV-emission spectroscopy experimental setup

For the radiation detection, a solar blind photomultiplier with a CsTe-photocathode (EMI G-26H315, MgF_2 -window, spectral response 110 to 340 nm, see figure 4.15) is installed at the monochromator's exit port. The photomultiplier signal is recorded by a National Instruments data acquisition (DAQ) PC-card NI-6013 with 16 bit resolution. For measuring VUV- and UV-spectra as a function of distance to the nozzle, the jet is mounted on a linear translation stage, controlled by a stepping motor.

Figure 4.16 shows that considerable VUV- and UV-radiation can be detected even at several centimetres distance from the nozzle. The radiation is not absorbed by the surrounding air, because the jet emits a plume of helium, in which VUV-radiation can be transported. The main spectral features visible are the atomic oxygen line at $\lambda = 130$ nm, the Schumann-Runge bands, and NO-bands from gas impurities between 180 and 300 nm.

(V)UV-radiation might thus indeed be responsible for an energy transport from the APPJ's core plasma into the effluent and produce excited atomic oxygen by pho-

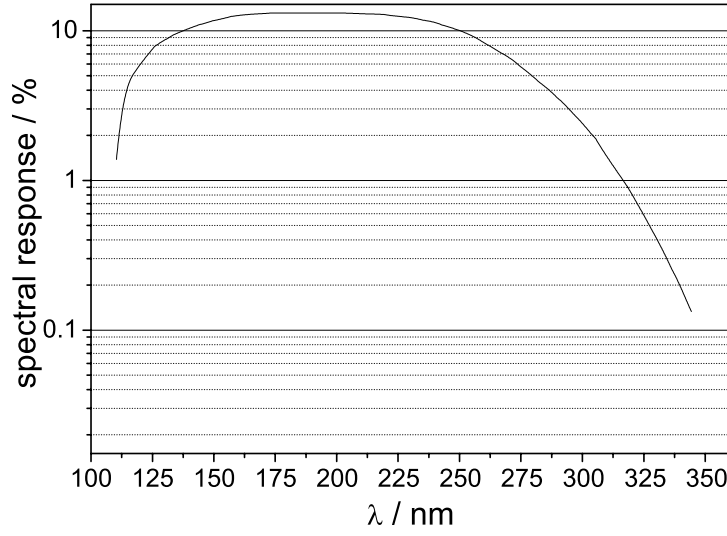


Figure 4.15: Quantum efficiency of the EMI G-26H315 photomultiplier [Gencom77]

to dissociation of metastable molecular oxygen outside the discharge. Since $O_2(a^1\Delta_g)$ has a lifetime of > 10 ms at one atmosphere of O_2 [Ogryzlo78], this metastable species can be present still at several centimetres from the jet's nozzle. The processes involving metastable molecular oxygen will be studied in the following by chemical model calculations. Subsequently, the influence of (V)UV-radiation on atomic oxygen generation is experimentally investigated.

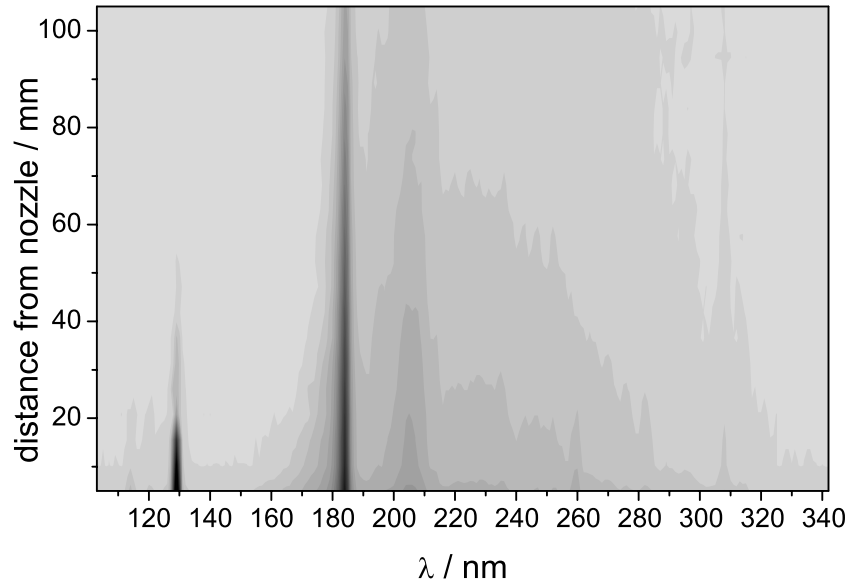


Figure 4.16: Space resolved (V)UV-emission spectrum of the APPJ

4.3 Oxygen Radical Chemistry in the Effluent

For a better understanding of the processes in the APPJ's effluent, chemical kinetics modelling is performed, following the assumptions presented in earlier works by Jeong et al. [Jeong00]. In the present study, also the temperature distribution in the effluent is taken into account. Furthermore, diffusion and radiation effects are considered. Ozone absorption measurements as well as optical emission spectroscopy on $O_2(b^1\Sigma_g^+)$ yield the missing oxygen radical input parameters necessary for the model calculations. From the comparison of model calculations with the measured oxygen radical densities, information about the processes and the energy transfer from the discharge region into the effluent is gained.

4.3.1 Chemical Kinetics Modelling

According to [Jeong00], the only species to be included in the chemical model of the APPJ's effluent are ground-state O_2 , O_3 , He, and O-atoms, as well as the two forms of metastable molecular oxygen $O_2(a^1\Delta_g)$ and $O_2(b^1\Sigma_g^+)$. This assumption is justified on the basis of lifetime calculations for charged particles and metastable atoms [Jeong00]. The recombination coefficient for ions and electrons at atmospheric pressure is approximately $10^{-6} \text{ cm}^3/\text{s}$ yielding a charged particle density of only 10^{11} cm^{-3} after $10 \mu\text{s}$. This value is well below the concentrations of the reactive neutral species, which are in the range of 10^{15} cm^{-3} (see e.g. chapter 4.1). The excited metastable $He(3S_1)$ - and $O(^1D)$ -states are rapidly quenched by reactions with O_2 . Both states exhibit a pseudo first-order rate constant of about 10^7 s^{-1} at O_2 -concentrations of 10^{17} cm^{-3} . Consequently, their lifetimes are only $0.1 \mu\text{s}$ in the here performed experiments. Likewise, metastable $O(^1S)$ is quenched by reaction with O_3 . Given a rate constant of $5.8 \times 10^{-10} \text{ cm}^3/\text{s}$, and an ozone concentration of $\sim 10^{15} \text{ cm}^{-3}$, the lifetime of $O(^1S)$ is less than $1 \mu\text{s}$. The transient mass balance for each of the six species considered in the model (O, O_2 , O_3 , $O_2(a^1\Delta_g)$, $O_2(b^1\Sigma_g^+)$, and He) is:

$$\frac{d[x]}{dt} = \sum_i k_i [x_i] [y_i] \left(\sum_j c_j [z_j] \right) \quad (4.8)$$

where $[x]$ ($[y]$) is the concentration of species x (y), and k_i is the rate of reaction i that either produces or consumes x (y). $[z]$ represents the concentration of the collision partners in three body reactions and remains unchanged. c_j are the respective

	reactions		rate constants	reference
R ₁	$O + O + M \rightarrow O_2 + M$	k ₁	$5.2 \times 10^{-35} e^{\left(\frac{900}{T}\right)\dagger\star}$	[Hampson75]
R ₂	$O + O_2 + M \rightarrow O_3 + M$	k ₂	$1.85 \times 10^{-35} e^{\left(\frac{1057}{T}\right)\ddagger\star}$	[Sabadil80]
R ₃	$O + O_3 \rightarrow O_2 + O_2$	k ₃	$1.5 \times 10^{-11} e^{\left(-\frac{2250}{T}\right)\diamond}$	[Hampson75]
R ₄	$O_2(a^1\Delta_g) + O_3 \rightarrow O + 2O_2$	k ₄	$6.01 \times 10^{-11} e^{\left(-\frac{2852}{T}\right)\diamond}$	[Jeong00]
R ₅	$O_2(b^1\Sigma_g^+) + He \rightarrow O_2 + He$	k ₅	$1 \times 10^{-17\diamond}$	[Jeong00]
R ₆	$O_2(b^1\Sigma_g^+) + O \rightarrow O_2 + O$	k ₆	$8.0 \times 10^{-14\diamond}$	[Jeong00]
R ₇	$O_2(b^1\Sigma_g^+) + O_3 \rightarrow O + 2O_2$	k ₇	$1.5 \times 10^{-11\diamond}$	[Jeong00]

Table 4.2: Reactions and their kinetic constants

(unit: \star cm⁶molecules⁻²s⁻¹; \diamond cm³molecules⁻¹s⁻¹; collision efficiencies: \dagger 0.62 for He and 1.15 for O₂; \ddagger 1.0 for O₂, and 0.54 for He, and 0.13 for O, and 2.27 for O₃)

collision efficiencies in case of a three body reaction. The reactions employed and the corresponding kinetic constants are presented in table 4.2.

The unit for the rate constants is cm³molecules⁻¹s⁻¹ for the two-particle reactions marked with \diamond , and cm⁶molecules⁻²s⁻¹ for the three-particle reactions marked with \star . T is the gas temperature in Kelvin. The collision efficiencies for the third collision partner in reaction R_1 is 0.62 in case of helium, and 1.15 in case of O₂. For reaction R_2 the collision efficiency is 1 in case of O₂ as third collision partner, 0.54 for helium, 0.13 for O, and 2.27 for O₃. Helium plays an important role as collision partner in the reactions. The helium density, however, remains unaltered. Therefore, the differential equation for helium is redundant. The remaining five coupled first order differential equations are solved numerically for a given set of starting parameters. As an example, equation 4.9 shows the differential equation for atomic oxygen:

$$\begin{aligned}
\frac{dn_O}{dt} = & -k_1 \cdot n_O n_O (0.62 \cdot n_{He} + 1.15 \cdot n_{O_2}) \\
& -k_2 \cdot n_O n_{O_2} (n_{O_2} + 0.54 \cdot n_{He} + 0.13 \cdot n_O + 2.27 \cdot n_{O_3}) \\
& -k_3 \cdot n_O n_{O_3} + k_4 \cdot n_{O_2(a^1\Delta_g)} n_{O_3} + k_7 \cdot n_{O_2(b^1\Sigma_g^+)} n_{O_3}
\end{aligned} \tag{4.9}$$

In the following, the described model will be adapted for the present study. Atmospheric conditions of the laboratory will be taken into account. It is considered whether the time dependent model can be compared to the space resolved O-density measured with TALIF-spectroscopy (chapter 4.1.3). The actual gas temperature distribution in the effluent, as well as diffusion effects are taken into account to make a comparison of oxygen radical density measurements and model calculations possible.

For the necessary modification of the model, initially the given starting parameters as described in Jeong et al. are used. For the following investigation, however, ozone and metastable $O_2(b^1\Sigma_g^+)$ densities are measured and used as input parameters for the final model calculations.

4.3.2 Adaption and Modification of the Model

The model calculations performed by Jeong et al. were compared to experimental data measured at the given atmospheric conditions at Los Alamos (New Mexico, USA), situated at an altitude of 2500 m. Figure 4.17 shows a comparison of model calculations at Los Alamos atmospheric conditions (dashed lines) and at the atmospheric conditions in Essen (solid lines), where the measurements presented in this work were performed. As can be seen, the differences in experimental conditions have little effect on the radical distribution in the jet's effluent. In the following, however, the calculations are based on the experimental conditions at the university laboratories in Essen.

Jeong et al. performed investigations and measurements of the oxygen radicals (except atomic oxygen) in the time afterglow of a parallel plate APPJ's discharge at

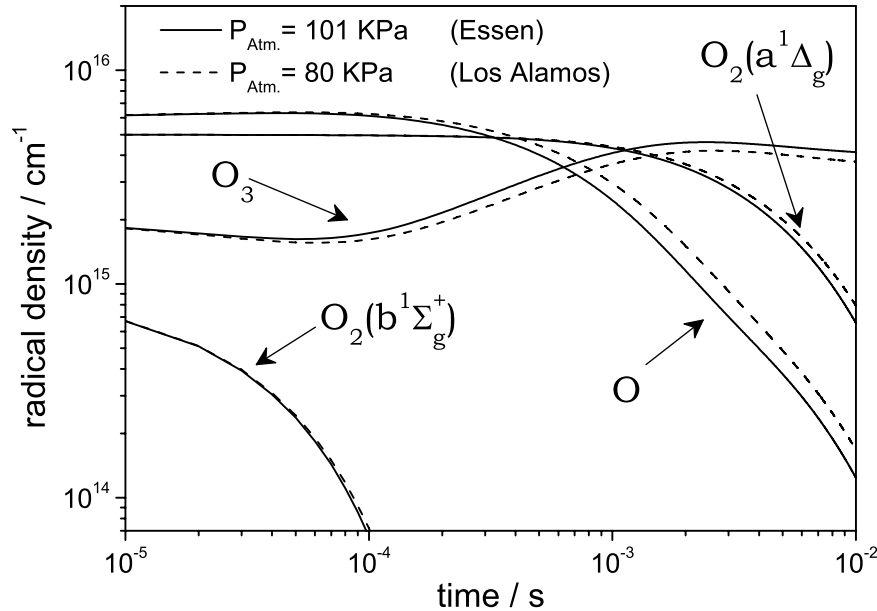


Figure 4.17: Chemical model calculations at different atmospheric conditions in Los Alamos (800 mbar) and in Essen (1013 mbar)

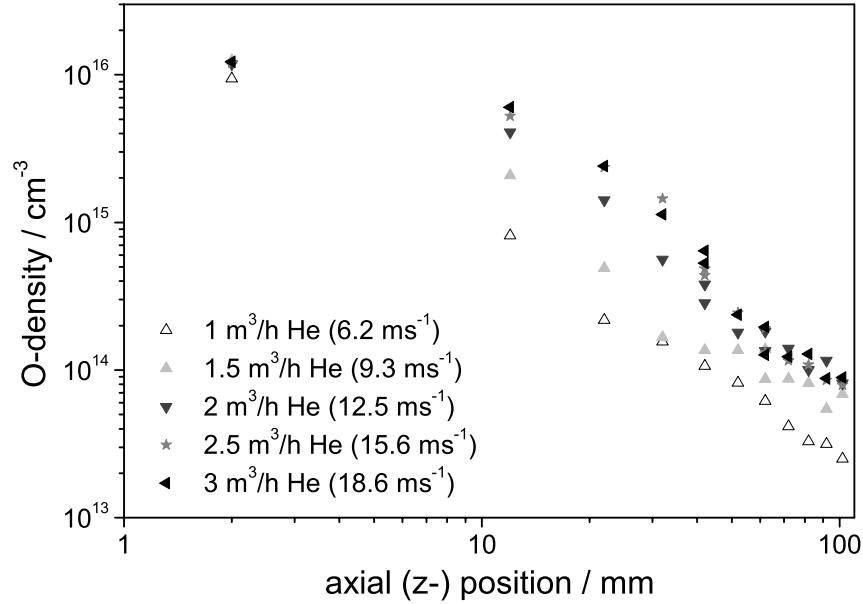


Figure 4.18: Measured atomic oxygen density as a function of distance from the nozzle for different total gas fluxes

different delays after plasma switch-off.³ Therefore, the resulting experimental data as well as the model are time dependent, whereas in the present study, measurements on the effluent of the APPJ are performed space resolved. To investigate whether the described time dependent model can be compared with space resolved measurements, on-axis TALIF-measurements are performed for different gas fluxes.

Figure 4.18 shows five measured atomic oxygen density distributions. From the total gas flux and the cross sectional area of the APPJ ($\sim 44 \text{ mm}^2$) a mean gas velocity for the respective gas fluxes is calculated (see figures 4.18 and 4.19). From the axial position (z) of the density measurements, a density distribution is derived for a constant gas velocity as a function of time of flight (see figure 4.19). As can be seen from the TALIF-measurements, the on-axis atomic oxygen density is rather a function of time of flight, than a function of the axial position (deviations towards higher time of flight will be investigated in the following). Transforming the axial position into time of flight, the time dependent model of the chemical processes in the effluent can thus be applied.

³Jeong et al. proceeded as follows for supplementary space-resolved measurements: they guided the effluent by an alumina and a cooled stainless steel plate, thus controlling the effluent's gas temperature and avoiding diffusion, at the cost of introducing additional surfaces, not considered in their model calculations.

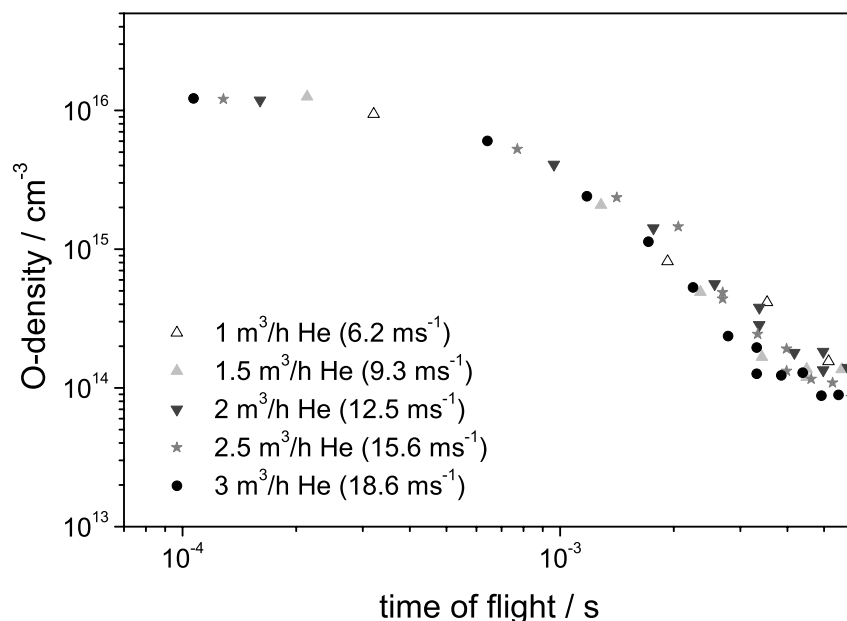


Figure 4.19: Measured atomic oxygen density as a function of time of flight (calculated from the average gas velocity) for different total gas fluxes

4.3.2.1 Temperature Distribution

As can be seen in table 4.2, rate constants k_1 to k_4 have a temperature dependent component. The temperature in the effluent at 10 cm distance is half of the temperature directly at the nozzle. In the model calculations presented in this work, the temperature distribution in the effluent is taken into account by considering the

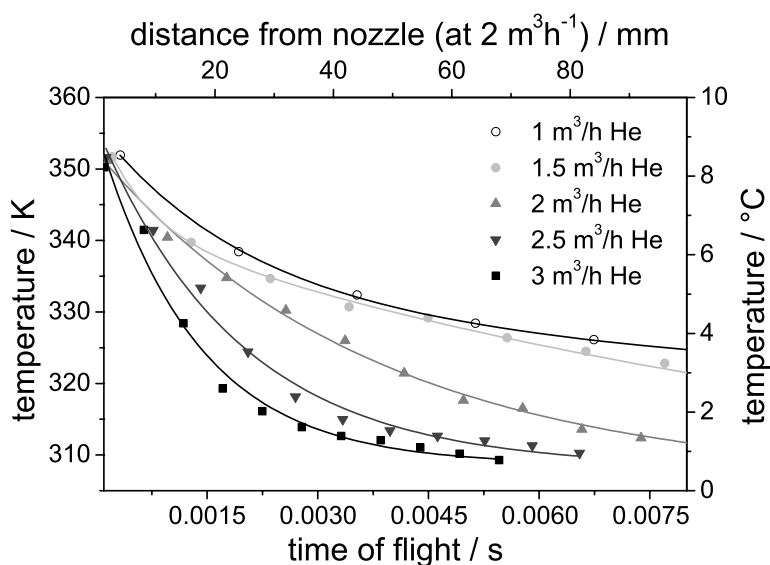


Figure 4.20: Measured on-axis gas temperature for different total gas fluxes

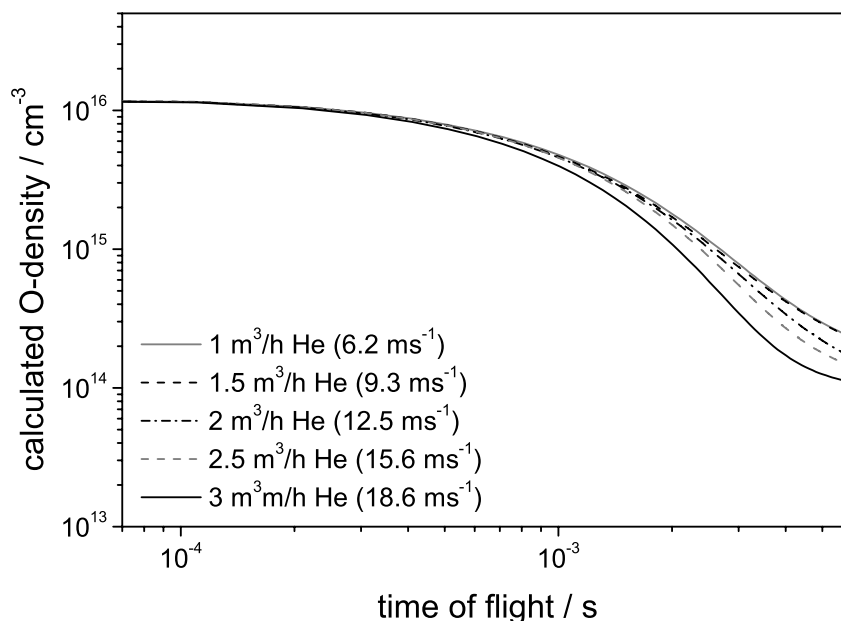


Figure 4.21: Model calculated atomic oxygen density as a function of time of flight for different total gas fluxes

actually measured on-axis gas temperature distributions (see figure 4.20) along the axis in the rate constants of the model calculations.

As can be seen in figure 4.21, occurring variation of O-density for different total gas fluxes towards higher time of flight (figure 4.19) can be explained by the model when the different temperature distributions for the different gas velocities are included in the calculations.

In a preliminary comparison of results from model calculations – taking temperature distribution into account – with experimental results, good agreement is achieved: In figure 4.22, the calculated O-density is compared with the on-axis O-density from TALIF-measurements (see chapter 4.1.3). The measured atomic oxygen density is plotted as a function of distance or time of flight, respectively, assuming a gas flux of ~ 12.5 m/s. The initial densities of the six species presented were chosen according to the actual experimental conditions and the measurements (for He and O), and according to measurements on the comparable APPJ investigated in [Jeong00] (for O_3 , $O_2(a^1\Delta_g)$ and $O_2(b^1\Sigma_g^+)$). The only parameter varied was the molecular oxygen admixture. With the on-axis temperature distribution taken into account, agreement between TALIF-measurements and model calculations of the atomic oxygen density is achieved, however, it is necessary to assume a molecular oxygen admixture of 1 vol% instead of the actual 0.5 vol% admixture in the measure-

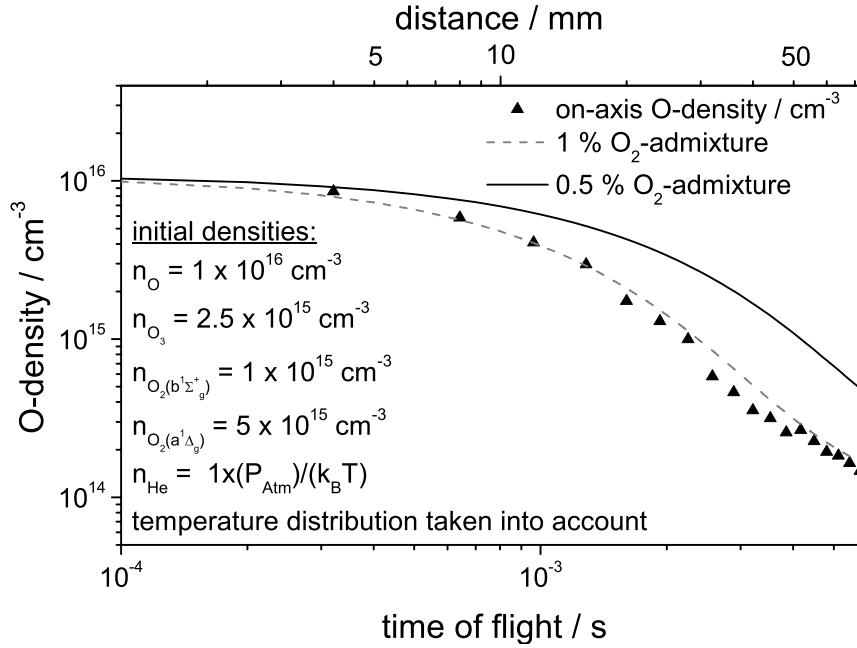


Figure 4.22: Measured on-axis atomic oxygen density in comparison to model calculations for two different O₂-admixtures taking the temperature distribution into account

ments. It is presumed that taking into account diffusion and radiation effects will result in further improvement of the accordance between calculations and measurements.

4.3.2.2 Diffusion

The on-axis atomic oxygen density in the effluent's downstream flow is decreased by diffusion. The diffusion of the effluent can be observed in the O-density map presented in figure 4.12. In figure 4.23 the full width at half maximum (FWHM) of the lateral O-density profiles taken from the O-density map is plotted as a function of distance from the nozzle. The linear increase of the FWHM is a measure for the atomic oxygen diffusion. In figure 4.24 the measured on-axis O-density (derived from figure 4.12) is shown.

In order to allow a comparison of the measurements with the chemical model which does not include diffusion, a confined effluent can be assumed, with a fixed FWHM of the initial 1.2 mm (taken from the lateral O-density profile directly at the jet's nozzle). The respective lateral O-density profiles of this confined effluent would in comparison to the non-confined effluent be smaller in width, but – assuming

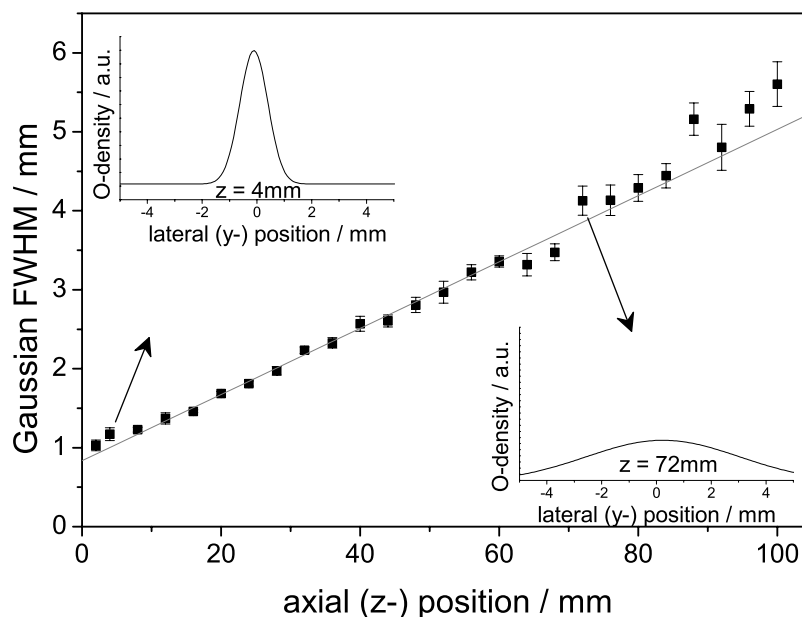


Figure 4.23: Full width at half maximum of the lateral O-density profiles taken from the O-density map in figure 4.12 as a function of distance from the nozzle

the same integral O-density – higher at the centre. The resulting on-axis O-density, shown in figure 4.24, represents an estimate for the O-density without diffusion. These results can now be directly compared to the calculated O-density in the model. For a concluding comparison of measured radical densities with model calculations, measurements of the ozone density and OES on $\text{O}_2(\text{b}^1\Sigma_g^+)$ will be performed in the following.

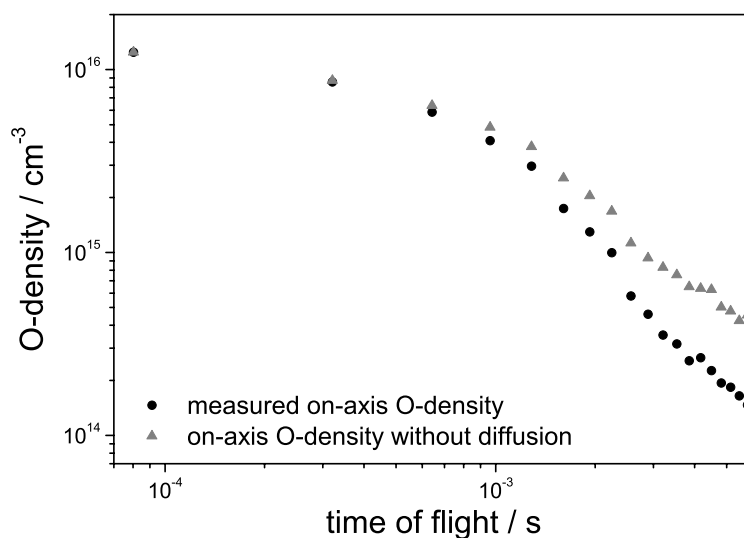


Figure 4.24: Measured on-axis O-density taken from figure 4.12 and on-axis O-density calculated from these measurements assuming a confined effluent without diffusion

4.3.3 Ozone and $O_2(b^1\Sigma_g^+)$ -Density Measurements in the Effluent

For the six species relevant for the chemical model calculations, starting parameters for the radical densities need to be defined. The initial densities of helium and molecular oxygen are derived from the experimental conditions. The initial density of atomic oxygen is taken from the TALIF-measurements. The density of metastable $O_2(a^1\Delta_g)$ is in the same magnitude as the atomic oxygen [Jeong00]. The densities of ozone and $O_2(b^1\Sigma_g^+)$ are determined in the following.

4.3.3.1 Ozone

The ozone density in the APPJ's effluent is determined by UV-absorption spectroscopy. The experimental setup is shown in figure 4.25. The $\lambda = 253.7$ mercury line of a Hg/Ar-lamp is used for the UV-absorption measurements. The UV-spectrum, recorded with a 0.2m monochromator (Minuteman Laboratories Inc. 302VM, see

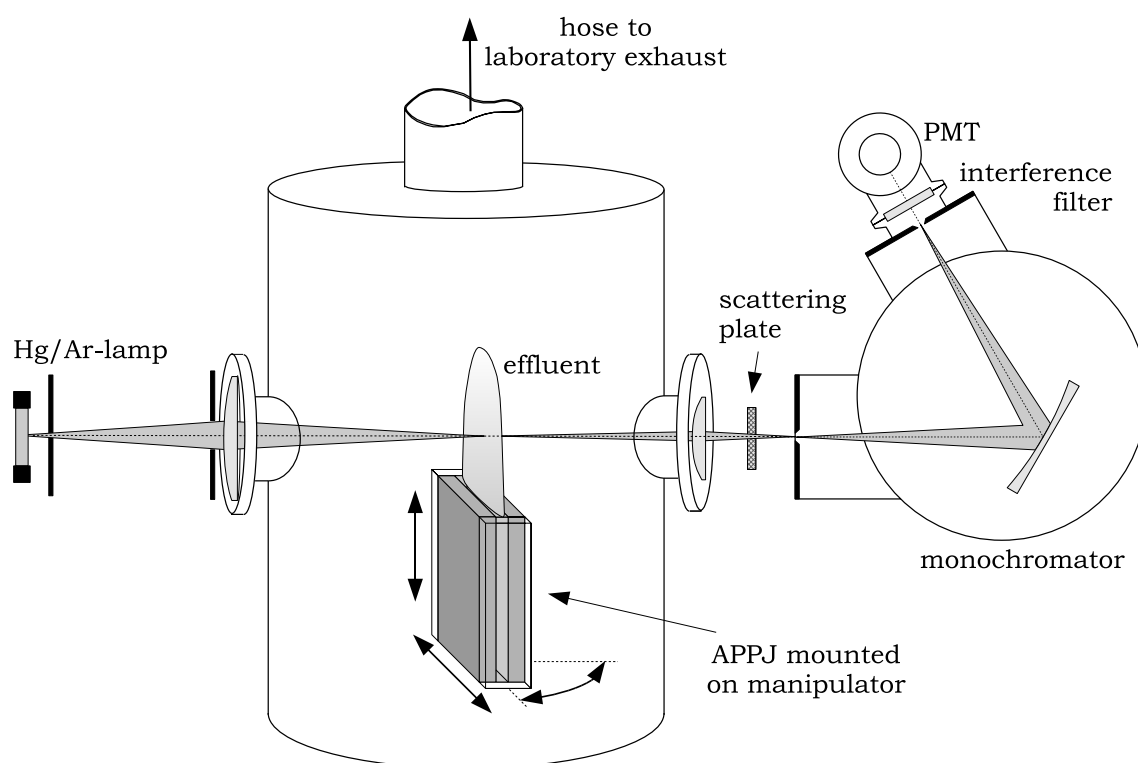


Figure 4.25: Experimental setup of the ozone density measurements by UV-absorption spectroscopy

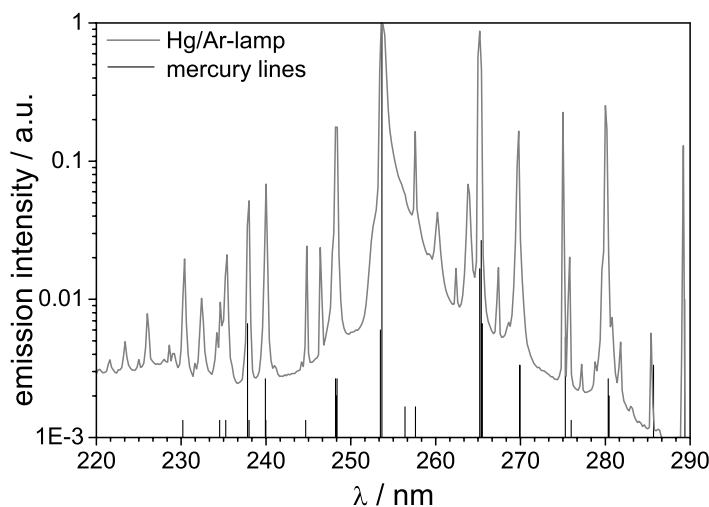


Figure 4.26: Emission spectrum of the mercury/argon lamp with corresponding Hg-lines taken from [Sansonetti01]. The Hg-line at ~ 253 nm is used for the absorption measurements on ozone.

chapter 4.2.2), is depicted in figure 4.26. The density is calculated by Beer's law (see chapter 2.2) taking into account the absorption cross section of ozone as taken from [Parisse96] (see figure 4.27). The light is focused into the plane of the APPJ and focused afterwards onto the slit of the monochromator. At the exit slit of the monochromator, a dielectric interference filter (Roper Scientific GmbH, $\lambda_0 = 258.6$ nm, $T = 33.4\%$, $\text{FWHM} = 38.8$ nm) is placed, in order to reduce stray light. The APPJ is operated under the same experimental conditions as for the TALIF-measurements (described in chapter 4.1.1), placed in a recipient filled with one atmosphere of helium. The off-gas of the APPJ is vented through a large flange connected to the laboratory exhaust.

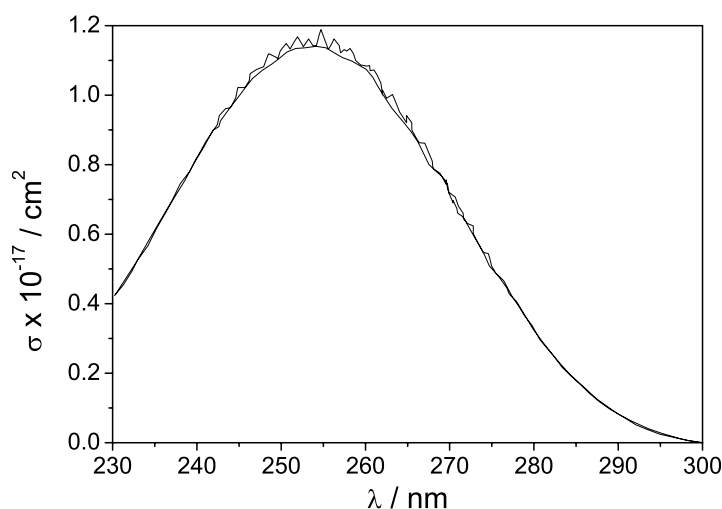


Figure 4.27: Absorption cross section data of ozone (Hartley system) recorded at atmospheric pressure and ambient temperature. For details see [Parisse96].

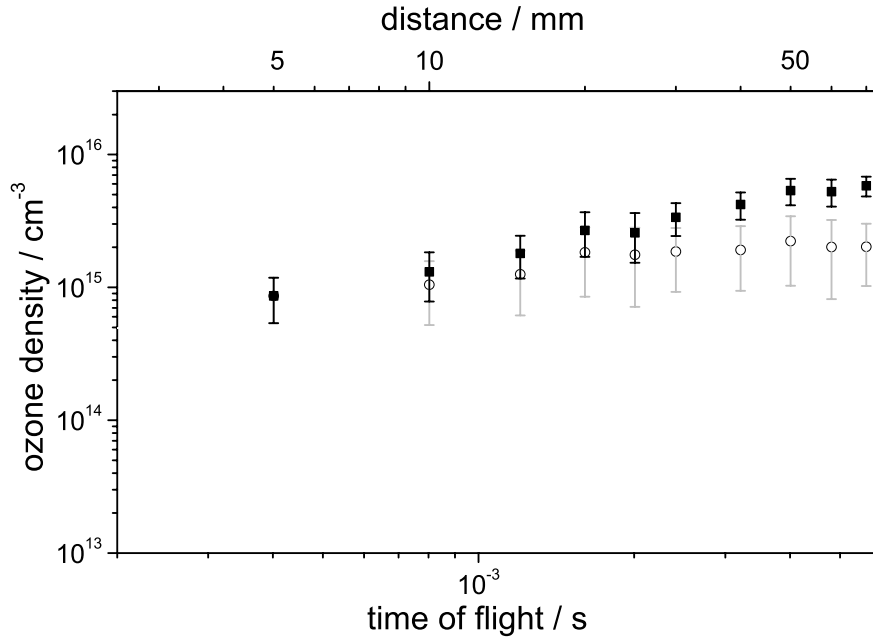


Figure 4.28: On-axis ozone density as measured (\circ) and ozone density with diffusion effects considered (\blacksquare)

To override experimental problems of striae due to density inhomogeneity of the effluent and the surrounding air⁴ deflecting the beam of light, a Suprasil scattering plate is placed in front of the slit of the monochromator. This significantly reduces the spacial dependency of the transmitted light signal. For absorption measurements, the jet is alternately switched on and off, thus allowing a reference measurement without absorption. The ozone density measurements were calibrated in an external setup in air which provided a higher accuracy due to the decreased distance between lamp and detector. The calibration measurements were performed directly at the nozzle, where the influence of the atmosphere on the radical density distribution is assumed to be negligible (a detailed view on measurements at ambient conditions will be given in chapter 5.2.3.4). The resulting on-axis ozone density distribution is shown in figure 4.28. It needs to be taken into account that diffusion decreases the on-axis density in the downstream flow. For the following model calculations, an estimate of the on-axis ozone density without diffusion is calculated in the same way as for the on-axis O-density in chapter 4.3.2.2.

⁴The refractivity of helium is one-eighth that of air [Stone04].

4.3.3.2 $\text{O}_2(\text{b}^1\Sigma_g^+)$

A relative density distribution of $\text{O}_2(\text{b}^1\Sigma_g^+)$ is derived from optical emission spectroscopy. The spectroscopic setup is described in chapter 3.4.2. Directly adjacent to the most prominent feature (the 777 nm oxygen line) in the spectrum already presented in figure 3.22, is the emission band of singlet metastable molecular oxygen. In figure 4.29 only the $\text{O}_2(\text{b}^1\Sigma_g^+)$ -band is shown (transition $(\text{b}^1\Sigma_g^+), \nu=0 \rightarrow (\text{X}^3\Sigma_g^-), \nu=0$). The R and P branches are centered at 759.9 and 764.5 nm. The light is captured with an optical fibre placed at 4 mm distance from the nozzle, with the optical path parallel to the discharge gap and perpendicular to the gas flow direction. The spectra shown in figure 4.29 are recorded for seven different gas fluxes. The helium line at 706 nm remains constant within the error margin of below 10 %. The plasma parameters are therefore assumed to remain unchanged during gas flux variation, as could also be seen from temperature and O-density measurements in chapter 4.3.2, which showed unvarying results directly at the jet's nozzle.

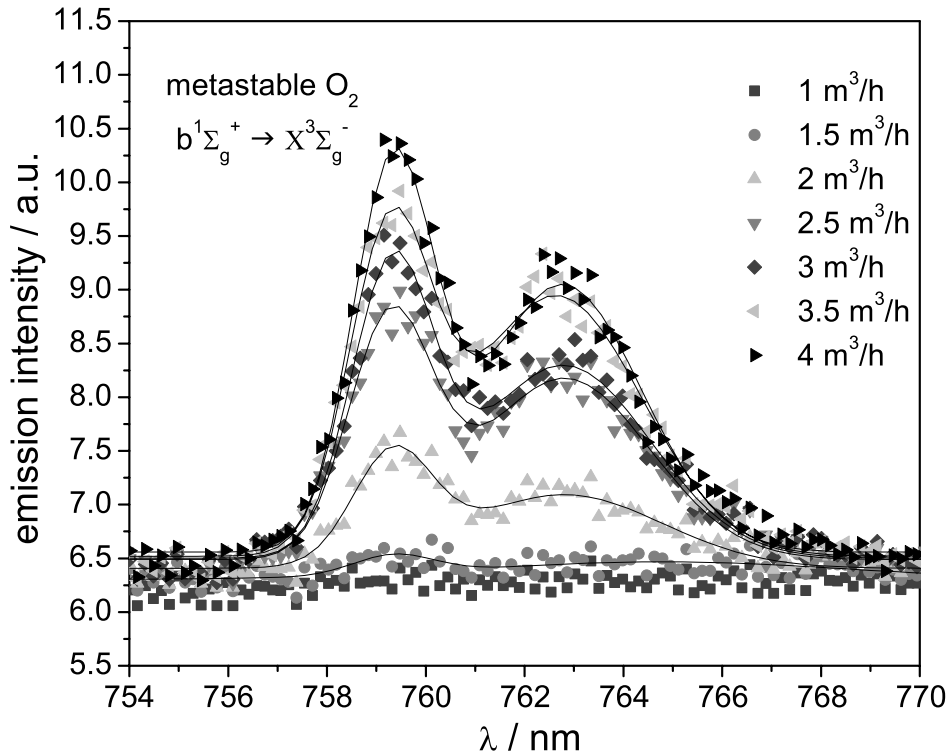


Figure 4.29: OES on $\text{O}_2(\text{b}^1\Sigma_g^+)$ at 4 mm distance from the jet's nozzle in helium atmosphere at 150 Watt and 1 vol% O_2 -admixture for seven different gas fluxes

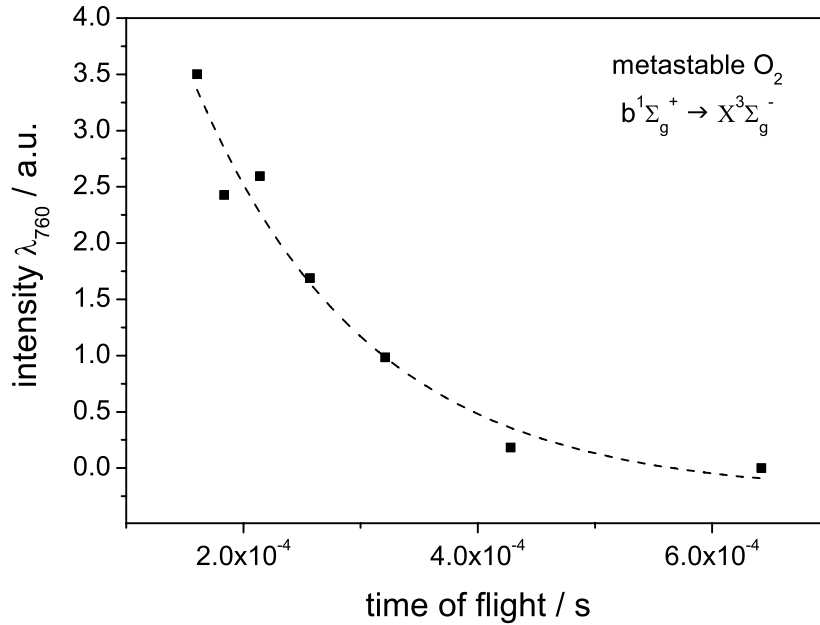


Figure 4.30: Intensity of the $O_2(b^1\Sigma_g^+)$ -peaks at ~ 759 nm versus time of flight calculated by average gas velocities and OES-measurement distance of 4 mm from the jet's nozzle

Figure 4.30 shows the intensity of the $O_2(b^1\Sigma_g^+)$ -band at 759 nm as a function of time of flight, calculated from the average gas velocities.

4.3.4 Comparison of Measured Oxygen Radical Densities with Chemical Model Calculations

The final results from the model calculations compared with the measured radical densities (O , O_3 , and $O_2(b^1\Sigma_g^+)$) are depicted in figure 4.31. The open symbols represent the measurements and the solid symbols are the radical densities with diffusion effects taken into account according to chapter 4.3.2.2. The relative $O_2(b^1\Sigma_g^+)$ -density as derived from the OES-measurements in chapter 4.3.3.2 is reconciled with the density distribution from the model calculations to achieve an absolute $O_2(b^1\Sigma_g^+)$ -density. The progression of measured and calculated oxygen radical densities is in excellent agreement. The processes in the effluent can be summarised as follows: Ozone is produced by the three-body reaction of atomic and molecular oxygen with a third reaction partner. A high consumption of ozone close to the nozzle is mainly due to reaction with $O_2(b^1\Sigma_g^+)$. The rapid decrease of the $O_2(b^1\Sigma_g^+)$ -density due to this reaction explains the observed increase of the ozone

density towards higher distances from the nozzle. The model calculations also show that the $\text{O}_2(\text{a}^1\Delta_g)$ -density decreases slowly (due to the metastables' high lifetime) and is still considerably high at several centimetres distance from the nozzle. The likewise slow decrease of the atomic oxygen density can partially be explained by reaction of ozone with $\text{O}_2(\text{a}^1\Delta_g)$, generating atomic oxygen. However, the comparison shows that the calculated atomic oxygen density has to be assumed lower than the measurements proved it to be, in order to achieve agreement towards higher time of flight. Accordance between measured radical densities and results from the model calculations is achieved when atomic oxygen produced by (V)UV-radiation is added to the calculated O-density. Experimental proof for the presumed atomic oxygen generation in the jet's effluent through photodissociation by (V)UV-radiation is given in the following.

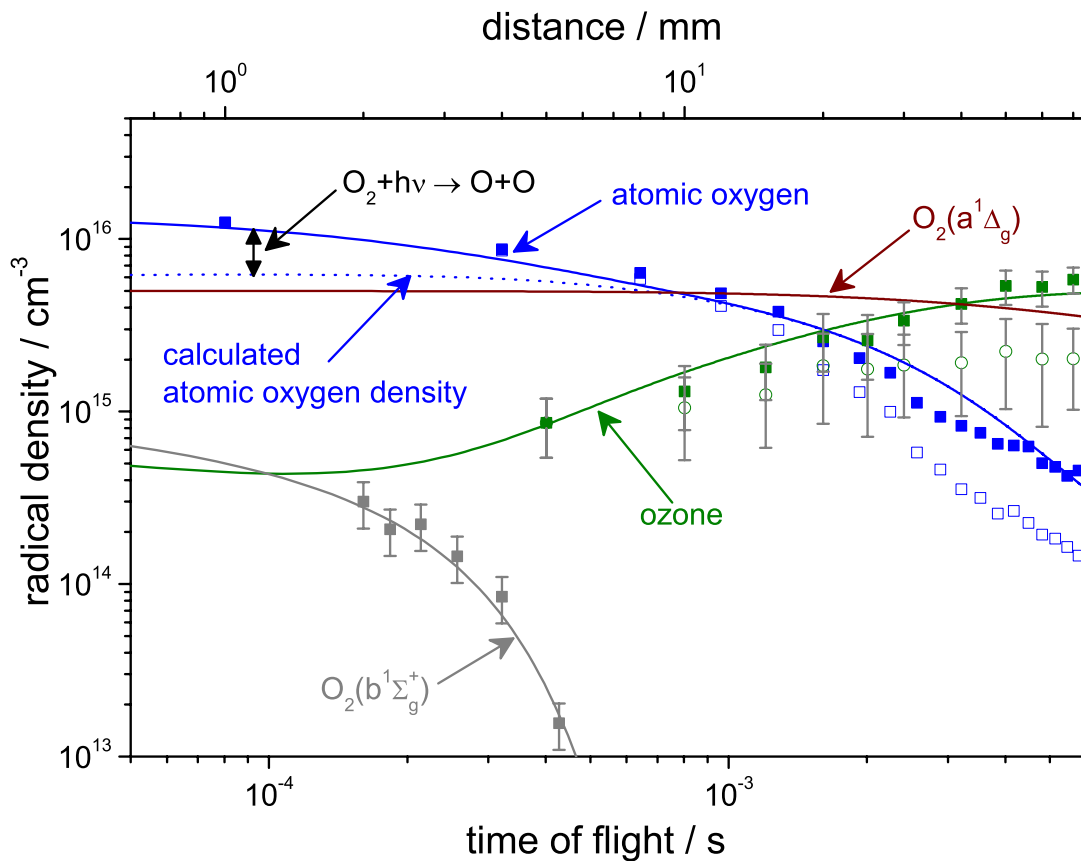


Figure 4.31: Comparison of chemical model calculations with the measured oxygen radical densities. Solid symbols represent the on-axis radical densities with diffusion effects considered. Open symbols for atomic oxygen and ozone represent the measured on-axis densities.

4.3.5 Atomic Oxygen Production by (V)UV-Radiation

The influence of the (V)UV-radiation on the generation of atomic oxygen in the jet's effluent is investigated by blocking this radiation, while the particle flux remains unhindered. For this purpose, a (V)UV-blocking nozzle was developed for the APPJ. This (V)UV-trap, a schematic of which is depicted in figure 4.32, consists of a bisected (BK7) glass tube of 10 mm diameter, in which a glass rod of 1.5 mm diameter is centred. The trap is set in front of the electrode gap and prevents a direct line of sight into the jet. The advantage of glass as (V)UV-trap material is its extremely low recombination coefficient for atomic oxygen ($\sim 10^{-4}$) [Cartry99]. Due to this low sticking coefficient, the O-density can be assumed to decrease insignificantly towards the walls, making diffusion negligible [Macko04]. Not only the wall material, but also high pressure, as well as laminar gas flow reduce particle-wall interaction and thus O-recombination to a minimum [Diamy05]. The effectiveness of this (V)UV-trap is demonstrated in figure 4.33, where a (V)UV-spectrum at 12 mm distance to the jet's nozzle is shown with and without the trap set in place. The (V)UV-radiation is reduced below the detection limit of the (V)UV-spectroscopic measurement setup (see figure 4.14), which is three orders of magnitude lower than the initial (V)UV-radiation intensity.

The effect of the (V)UV-radiation on the atomic oxygen generation is tested by TALIF-measurements. The results from TALIF-measurements with and without the (V)UV-trap are shown in figure 4.34. Installing the (V)UV-trap indeed results in a reduction of atomic oxygen density by a factor of ~ 4 . This reduction can be

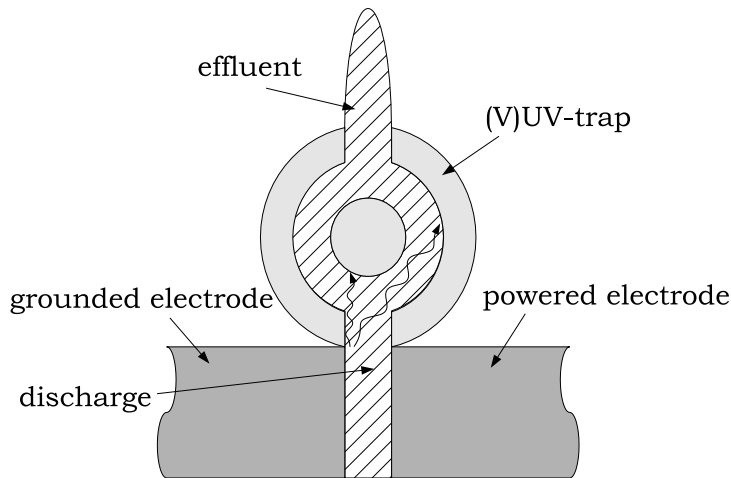


Figure 4.32: (V)UV-radiation emitted by the APPJ is blocked by a (V)UV-trap made of BK7-glass which prevents a direct line of sight into the jet

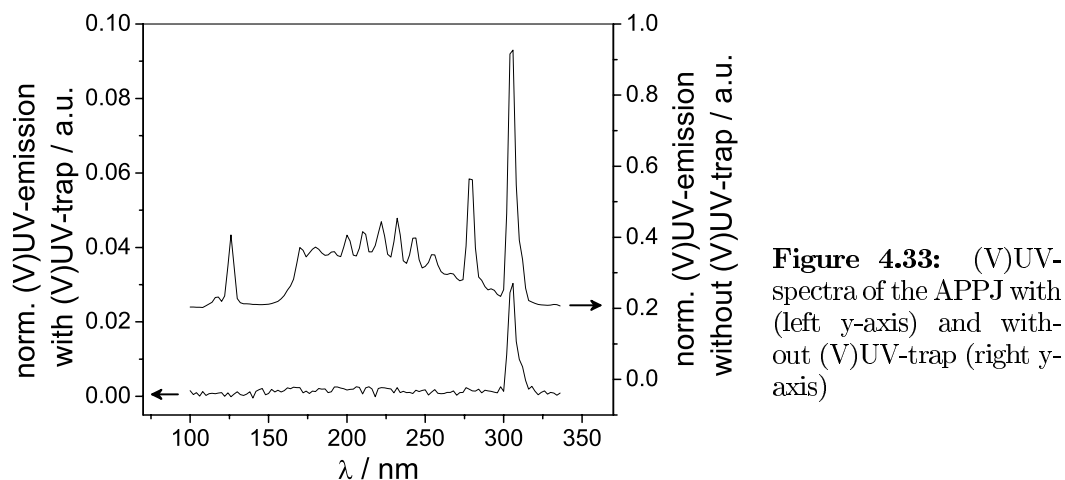


Figure 4.33: (V)UV-spectra of the APPJ with (left y-axis) and without (V)UV-trap (right y-axis)

explained by the lack of photodissociation (for the mechanisms see e.g. [Lee77, Nee97, Parker00]).

It can be concluded that (V)UV-radiation from the APPJ's core plasma – by photodissociation of molecular oxygen – produces atomic oxygen outside the discharge. These results substantiate the assumption that (V)UV-radiation in combination with metastable oxygen $O_2(a^1\Delta_g)$, which is present still far into the effluent (see chapter 4.3), does supply sufficient energy for generation of excited atomic oxygen outside the discharge.

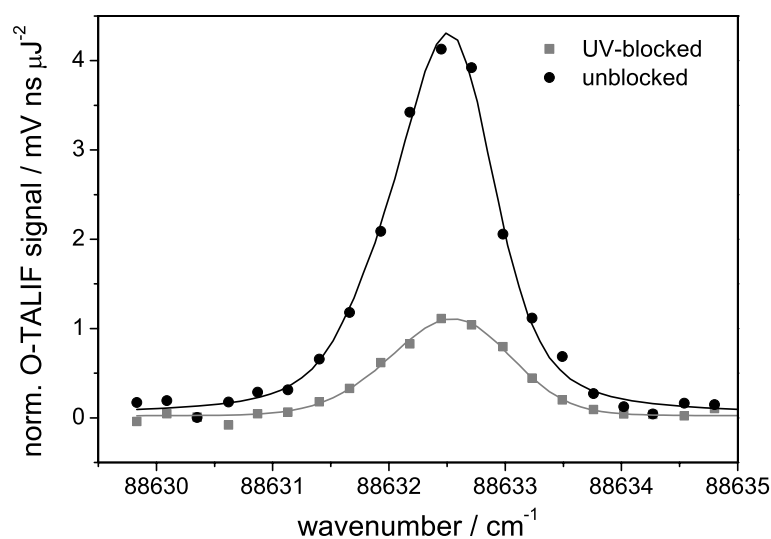


Figure 4.34: Comparative TALIF-measurements with and without (V)UV-trap show a significant effect on the O-density

4.4 An Outlook to the μ -APPJ

Based on the present study, a new so-called μ -APPJ was developed [Reuter07, Niemi07], which offers a wider observation angle of the discharge region. This modified APPJ is expected to supplement the present work's understandings of the processes in the effluent by insights into the processes within the plasma, in future studies.

A schematic of the μ -APPJ is depicted in figure 4.35. The length of the discharge region is approximately 3 cm. The dimension of the discharge cross section is $1\text{ mm} \times 1\text{ mm}$, yielding a reduction of the cross section by a factor of 40 compared to the regular planar APPJ. The jet can be operated at RF-power ranging from about 2 to 40 Watt. Due to the reduced size, the gas flux can be reduced down to several standard litres per minute (slm). The jet is equipped with windows at the sides.

A VI-characteristic of the μ -APPJ, depicted in figure 4.36, shows the resemblance of the μ -APPJ to the regular APPJ. The jet is operated in an abnormal glow. Towards high RF-power, the α -mode of the glow discharge constricts into a γ -mode discharge. Reducing the power reverts the discharge form back to the initial α -mode.

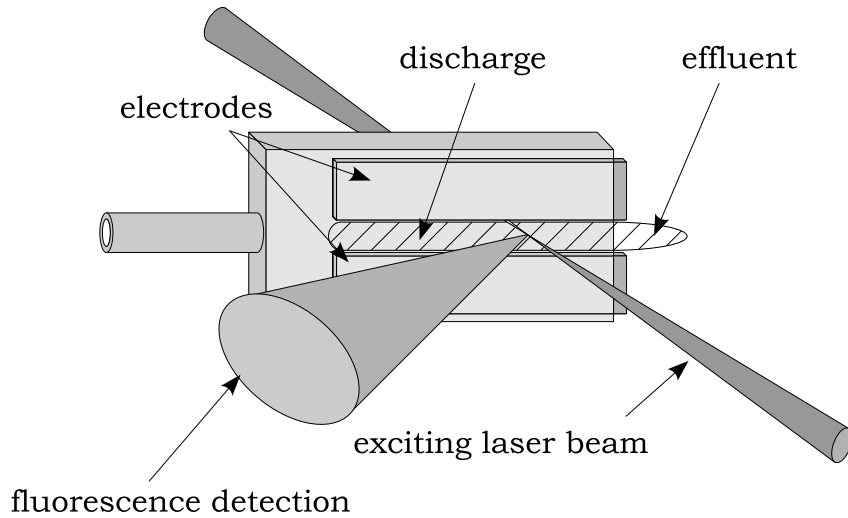


Figure 4.35: Schematic of the μ -APPJ, depicting a possible laser excitation and fluorescence detection scheme for TALIF-measurements inside the discharge region

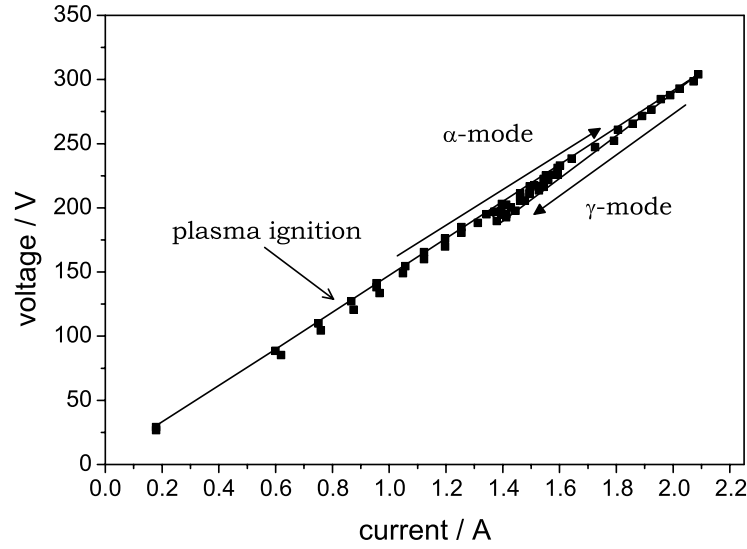


Figure 4.36: VI-characteristic of the μ -APPJ operated with 3 slm helium and no oxygen admixture

Due to the wide optical access to the discharge section, this new setup makes two-photon laser induced fluorescence (TALIF) spectroscopy inside the discharge region possible.⁵

4.5 Conclusion

The oxygen radical densities in the effluent of the APPJ were measured by TALIF-spectroscopy (O), UV-absorption measurements (O_3), and OES ($O_2(b^1\Sigma_g^+)$). A comparison of these measured radical densities with densities derived from chemical kinetics model calculations showed the following processes in the effluent: Ozone is produced by the three-body reaction of atomic and molecular oxygen with a third reaction partner. A high consumption of ozone close to the nozzle is mainly due to reaction with $O_2(b^1\Sigma_g^+)$. The rapid decrease of the $O_2(b^1\Sigma_g^+)$ -density explains the observed increase of the ozone density towards higher distances from the nozzle. The slow decrease of the atomic oxygen density can partially be explained by reaction of ozone with $O_2(a^1\Delta_g)$, generating atomic oxygen. However, the comparison showed that the atomic oxygen density in the APPJ's effluent is higher than predicted by model calculations. Further investigations lead to the conclusion that

⁵A publication is planned. See also: N. Knake, *Bestimmung der atomaren Sauerstoffkonzentration in einem Plasmajet zur Oberflächenbehandlung*, diploma thesis, University of Duisburg-Essen, submitted September 2007 [Knake07].

(V)UV-radiation from the APPJ's core plasma produces ground state atomic oxygen outside the jet in the effluent. This is supported by measurements with suppressed VUV-radiation and unblocked oxygen radical flow. Two causes for an energy transport from the APPJ discharge region into the jet's effluent could be identified: The chemical model calculations state the presence of energetic metastable $O_2(a^1\Delta_g)$ far outside the discharge region. Along with the (V)UV-radiation with an energy of several eV, these metastables provide sufficient energy for the production of excited atomic oxygen outside the APPJ's discharge region.

Chapter 5

Oxygen Radical Interaction Processes in APPJ Surface Treatment

The atmospheric pressure plasma jet is a plasma source ideally suited for treatment of sensitive surfaces and has – among other possible fields of application – already been successfully used for deposition and etching of thin films [Babayan01b, Park98, Jeong98]. As the previous chapters demonstrated, the main reactive species in the jet’s effluent are, apart from metastable O₂-molecules, atomic oxygen, ozone, and VUV-radiation. The latter three species have each separately been employed for surface treatment [Peeling03, Criegee75, Hozumi04, Joubert89]. Used in combination, synergistic effects of enhanced surface functionalisation can be observed [Boudam06]. In this chapter, possible applications for the atmospheric pressure plasma jet are presented. Following a brief overview on preliminary investigations on silicon oxidation in chapter 5.1, special emphasis is set on the hydrophilisation of polymers in chapter 5.2.

With the aid of plasma diagnostics as described in the previous chapters and the results from two-photon absorption laser induced fluorescence (TALIF) spectroscopy measurements of the atomic oxygen ground state density and model calculations (see chapter 4), the processes involved in the hydrophilisation of polymers by plasma treatment with the APPJ are investigated in a parameter study, by correlating the polymer’s wettability – determined by water contact angle measurements – with the oxygen radical densities in the effluent.

5.1 Preliminary Investigations on Silicon Oxidation

In cooperation with the group of Prof. Dr. Möller¹ at the University of Duisburg-Essen, the APPJ was tested for its suitability for silicon oxidation. Silicon constitutes the base material for integrated circuits in semiconductor technology, during the production of which two thirds of the processing steps are based on plasma technology [BMBF07]. The structures of integrated circuits continuously become smaller. Simple and cost efficient deposition processes need to be established for assembly line production. In order to create the required nanoscale transistors, insulating intermediate barrier oxide layers are applied. For smaller structures, these oxide layers also have to become thinner. For silicon as base material, these barrier layers usually consist of SiO₂-films. To avoid expensive vacuum equipment, processes to produce SiO₂-layers in ambient conditions are sought after. The most common method for forming SiO₂-film is thermal oxidation of silicon in O₂-atmosphere. This method requires heating at over 900°C [Tosaka05]. Also used and reported in literature is the photooxidation method, where oxygen radicals are generated by photodissociation of molecular oxygen [Fang03] or ozone [Tosaka05]. Fang and coworkers operated at low pressure and Tosaka et al. operated at elevated temperatures. The processes both required highly reactive oxygen radicals.

Since the APPJ provides not only ozone and vacuum ultraviolet radiation but also ground state as well as excited atomic oxygen and metastable molecular oxygen, a vast effect on silicon surfaces was expected. For silicon oxidation two silicon samples were treated with the atmospheric pressure plasma jet for 10 minutes at a distance of 10 mm from the nozzle at 150 Watt input power with 2 m³/h helium flux and 1 vol% oxygen. The treated samples were then analysed by Auger spectroscopy. The thickness of the resulting SiO₂-layers was 9 nm. The growth rate of 0.9 nm per minute in a not optimised process is remarkable, especially since – in contrast to previous studies mentioned above – the process takes place at room temperature and in ambient conditions.

¹University of Duisburg Essen, Surface Science Group Prof. Dr. R. Möller / Dr. H. Nienhaus (www.exp.physik.uni-duisburg-essen.de/moeller).

5.2 Surface Functionalisation of Polymers

A central field of application of low temperature plasmas is the functionalisation of polymers. Manipulation of surface free energy, e.g. by implantation of oxygen [Schrader92], influences the surface properties of polymer material. Especially the enhancement of adhesion properties and wettability is essential in textile treatment, optics (e.g. for contact lenses), restoration and other applications, for many of which biocompatibility of the treated material is a vital factor.

Oxidation of polymer surfaces by atmospheric pressure plasma treatment is widely used in industrial applications. Since commonly used filamentary dielectric barrier discharges hold the danger of destroying the treated surfaces [Sira05], atmospheric pressure glow discharges are considered a promising alternative for treatment of polymers [Balcon07, Massines98a, Roth01b]. While plasma is very efficient in surface functionalisation, it also induces a degradation of the surface, i.e. the bond breaking by active species leads to a loss of polymer fragments. The degradation rate is particularly high when the substrate is in direct contact with the plasma, where it is exposed to ion and electron bombardment [Normand95].

The atmospheric pressure plasma jet is expected to be highly efficient in polymer treatment. The polymer surface to be functionalised has no direct contact to the plasma, it is exposed to the jet's effluent. As TALIF-measurements have shown (see chapter 4), the APPJ's effluent contains a high oxygen radical density, ideal for the manipulation of surface free energy of polymers. Furthermore, the effluent contains very few to no ions and electrons, thus inducing minimal surface degradation².

The present study focuses on a future application of the atmospheric pressure plasma jet which combines the jet's excellent sterilisation capability³ with its high potential for polymer surface functionalisation. In the following, therefore, the efficiency

²In the cooperative project „Oberflächenmodifikation mit Plasma: Ein neues technisches Hilfsmittel für die Konservierung und Restaurierung von Kunststoffen“ together with Anna Comiotto, (group: Prof. Dr. S. Wuelfert, Hochschule der Künste Bern, Switzerland) polyethylene surface pretreatment with the APPJ for adhesion improvement was investigated. The APPJ significantly increases bonding of polyethylene samples by an acrylate adhesive, yielding a new implement in conservation and restoration of modern artwork. (www.hkb.bfh.ch/okonservierung.html)

³The sterilisation capability of the APPJ was investigated on commercially available bacterial culture stripes, containing resistance class III-type bacteria *Bacillus stearothermophilus* and *Bacillus subtilis*, in a cooperative project with the „Institut für Hygiene und Arbeitsmedizin“ AG Prof. Dr. A.W. Rettenmeier. Results from these investigations were presented at the Frühjahrsagung der Deutschen Physikalischen Gesellschaft [Reuter05] and at the 8th Symposium on Biomaterials and Biomechanics [Schulz-von der Gathen05].

of the APPJ for surface manipulation is investigated by treatment of polystyrene⁴ Petri dishes. By hydrophilisation of the Petri dishes' polymer surface, cell culturing of bacteria can be significantly increased [Choi99]. Accordingly, the influence of APPJ treatment on the wettability of polystyrene Petri dishes is investigated by contact angle measurements. The processes involved are analysed by variation of the APPJ's RF-power, variation of total gas flux, variation of oxygen admixture, as well as variation of distance between sample and jet's nozzle. A promising future application will be the simultaneous surface functionalisation and sterilisation of the Petri dishes' surface. The APPJ might thus offer ideal surface pretreatment for cell culturing. While the regular APPJ can be applied for treatment of large areas, the μ -APPJ introduced in chapter 4.4 is ideal for localised treatment, allowing precisely patterned surface functionalisation.

5.2.1 Hydrophilisation and Contact Angle Measurements

The wettability of a material can be tested by applying a drop of liquid (e.g. water) onto its surface. The applied liquid can adopt two states of equilibrium: the formation of a drop on the solids' surface (see figure 5.1a & b), or the state of total wetting (figure 5.1c). If the angle θ that the drop profile adopts with respect to the solids surface is non zero (figure 5.1a & b), the surface exhibits partial wetting. Two cases can be distinguished: In figure 5.1a θ is smaller than 90° , meaning that the surface is hydrophilic. In figure 5.1b θ is greater than 90° , meaning that the surface is hydrophobic.

A closer look at the three interfaces that appear in the system of solid sample (S), drop of liquid (L) and surrounding vapour (V) shows that the measurement of the contact angle can be used to monitor the free energy of a surface [Adamson90]. Each of the three interfaces has a certain amount of surface free energy per unit area, γ_{SV} , γ_{SL} and γ_{LV} . In the immediate vicinity of the triple point (rather a triple line in three dimensions), where the three phases meet, the shape of the drop becomes distorted, e.g. due to van der Waals forces [Gennes85]. T. Young [Young05] discovered that despite of this distortion, the drop-angle can be expressed merely by the thermodynamic quantities of the respective surface free energies, based on the assumption that in equilibrium the energy of the system remains stationary with respect to a displacement Δd of the triple point (see figure 5.2): The energy of the bulk

⁴Polystyrene $[-\text{CH}_2\text{CH}(\text{C}_6\text{H}_5)]_n$ is the base material for Styrofoam.

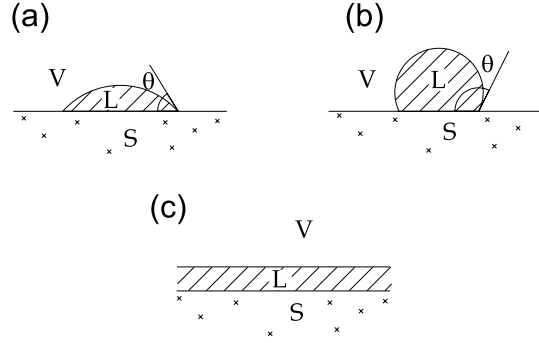


Figure 5.1: Drop of water on (a) hydrophilic and (b) hydrophobic solid surface and (c) complete wetting of surface. The three phases are indicated by V (vapour), L (liquid), and S (solid).

remains unchanged, since the pressure is the same in liquid and vapour. The energy in the vicinity of the triple point is not altered, because this point is only shifted and otherwise unchanged. Only the surface energies are changed proportionally to the change of surface areas, namely S_{SL} by Δd , S_{SV} by $-\Delta d$ and S_{LV} by $\Delta d \cdot \cos(\theta)$. This consideration led Young to equation 5.1:

$$\gamma_{SV} - \gamma_{SL} = \gamma_{LV} \cos(\theta) \quad (5.1)$$

Accordingly, the measurement of the contact angle yields quantitative information about the solid's surface and is used as an important analysis method in surface and materials science (see e.g. [Schrader92, Berg93]).

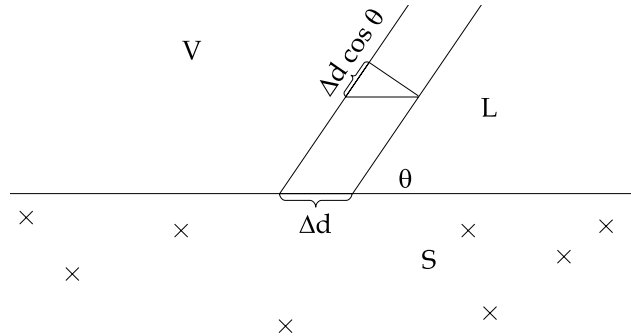


Figure 5.2: Geometric approach to Young's equation. Δd indicates the translation of the triplet point where the three phases (V; L; S) meet. θ is the contact angle the liquid adopts on the solid's surface.

5.2.2 Experimental Setup for Polymer Treatment

To investigate the influence of plasma treatment with the APPJ on the wettability of polymer samples, wettability measurements are performed by sessile drop technique, a diagnostic technique which is still very common due to its simplicity [Sira05, Spelt87]. A drop of distilled water ($\leq 5 \mu\text{l}$) is placed on the surface of the sample to be analysed. After a short time in which the three-phase system reaches an equilibrium state, the drop is photographed. The angle which the drop adopts with respect to the surface is deduced from the resulting picture. Computer-aided, a circle is fit to the boundary region of the water drop, subsequently the angle between the circles tangent and the intersecting substrate surface is calculated. The accuracy of the procedure is estimated to show less than 1° deviation.

The mechanical setup of the contact angle measurement system consists of a three axis moving stage on which the sample is placed and with which it can be positioned with respect to the camera by micrometre screws. The drop of distilled water is applied by a micro syringe (SDG 25F) and the volume of the drop is held below $5 \mu\text{l}$ to ensure that the drop's shape will not be distorted by gravitational effects [Amirfazli98, Drelich97]. The drop and the sample are illuminated from behind by a white lamp with an attached scattering plate, to achieve a contrast rich image of the drops curvature on the photograph. The three axis moving stage is placed on an optical bench, along with a stand for a digital camera (Canon Ixus V2 6x digital

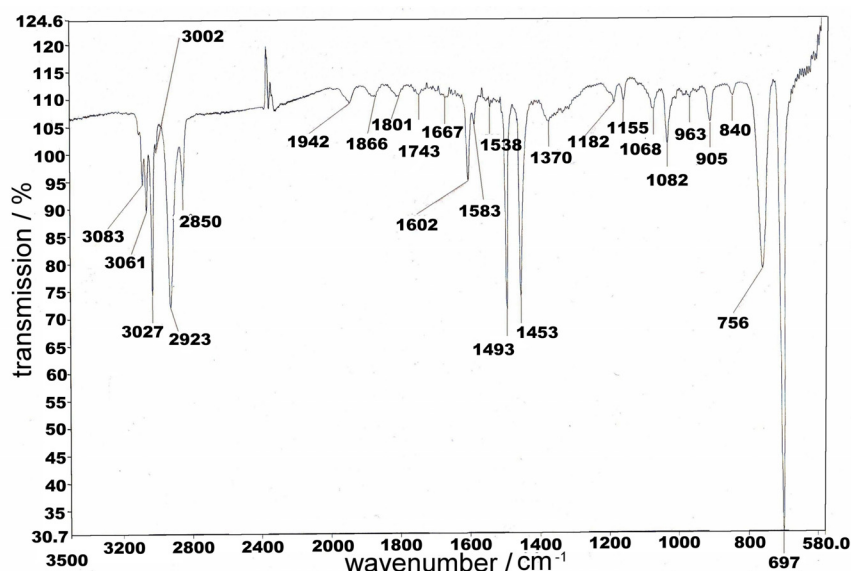


Figure 5.3: The ATR-FTIR-fingerprint of the polymer Petri dishes identifies the sample material to be polystyrene

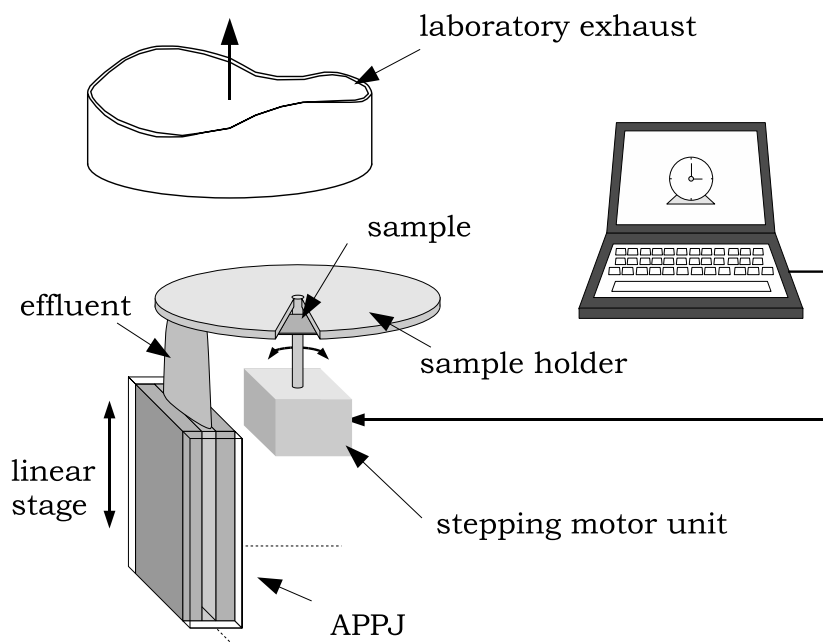


Figure 5.4: Experimental setup for polystyrene sample treatment. The rotatable sample holder allows a precise treatment time at stable plasma conditions.

zoom). The stand for the camera can be tilted, so that the drop can be photographed at a slight angle (≤ 1) ensuring a correct allocation of the drop's contact points on the resulting photograph [Spelt87].

In this study, plasma treatment of commercially available Petri dishes is investigated. An ATR-FTIR spectrum (see figure 5.3) identifies the material to be polystyrene.⁵ The Petri dishes have a water contact angle of 67° . Treatment with the APPJ proves very effective: Contact angles of about 10° can be reached. At contact angles below 20° , a surface can be considered very wetting [Roth07]. The strong hydrophilisation effect due to the high oxygen radical densities in the jet's effluent makes a thorough controlling of the treatment time necessary. To engage a stable discharge mode, the APPJ requires at times several seconds, depending on the state of the matching unit. A remote time control of the plasma power is thus prohibited. For treatment, the polystyrene sample is placed on a rotatable substrate holder (see figure 5.4), with which it can be moved into the jet's effluent at the start of the plasma treatment and removed at the end of the desired treatment time. This setup allows sample treatment for a precise period of time during which an unchanged plasma condition can be assumed, since the APPJ is continuously operated with a

⁵The author wishes to thank Anna Comiotto of the Hochschule der Künste Bern for performing the ATR-FTIR measurements.

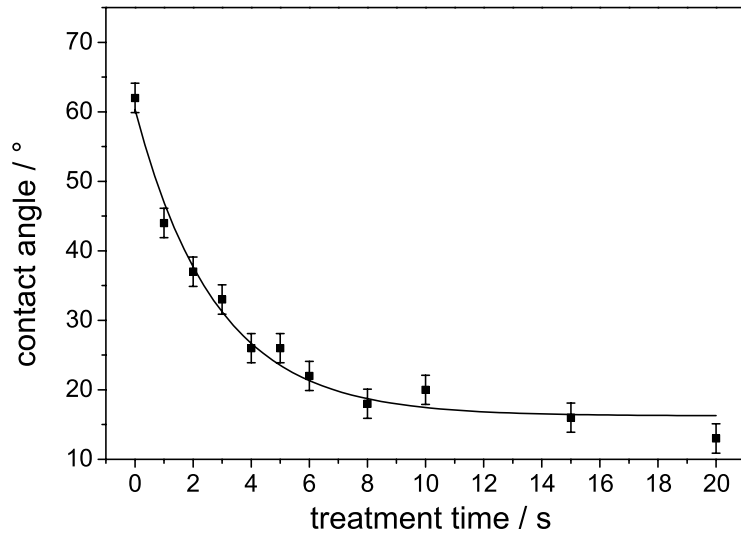


Figure 5.5: Contact angle of distilled water on a polystyrene surface as a function of treatment time. Samples are treated with the APPJ at a sample to nozzle distance of 18 mm, a gas flux of $2 \text{ m}^3/\text{h}$ helium and an oxygen admixture of 1 vol% at 100 Watt input power.

given set of parameters. Already after a treatment time of 2 seconds, an essential lowering of the contact angle to about 37° takes place (see figure 5.5), although the APPJ's operating parameters have not yet been optimised for hydrophilisation.

5.2.3 Parameter Study on Hydrophilisation of Polystyrene Petri Dishes

For further investigations, standard operating parameters for plasma treatment of polystyrene have been defined (table 5.1). These parameters are chosen so that the water contact angle achieved under standard conditions is situated in mid-range. A change in parameters can thus result in a change of contact angle in both directions. For the following study, each parameter is varied respectively. Multiple contact angle measurements on ten different samples at standard APPJ operating parameters prove the measurements to be correct within a standard deviation of 2.1° (see figure 5.6). This accuracy is typical for sessile drop contact angle measurements [Spelt87].

parameter:	value:
treatment time	2 s
gas flux	$2 \text{ m}^3/\text{h}$
oxygen admixture	1 vol%
RF-power	100 Watt
distance	18 mm

Table 5.1: Standard operating parameters for APPJ polymer treatment

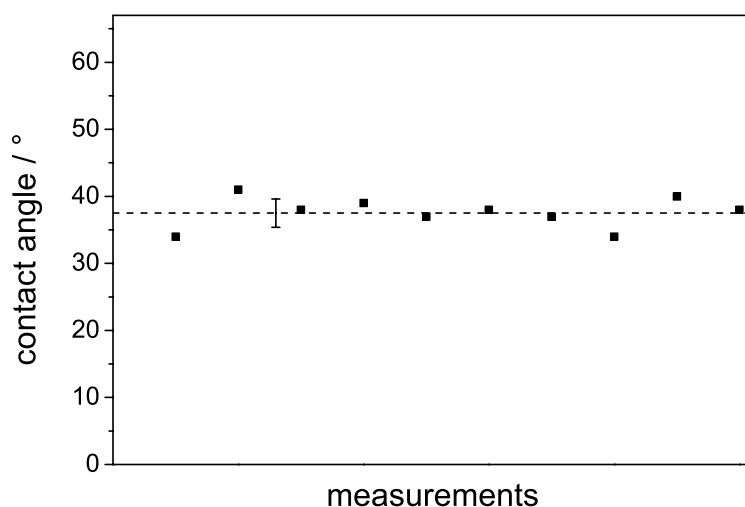


Figure 5.6: Measurement error of the contact angle measurements on samples treated for 2 seconds at APPJ standard operating parameters (see table 5.1)

The oxidising effect of polymer plasma treatment is temporary. Rehydrophobisation takes place after the treatment. For practical surface treatment, the hydrophilic effect has to persist at least until subsequent processing of the polymer is completed. The rehydrophobisation test described in the following proves polymer treatment with the APPJ to create a more than sufficiently long lasting hydrophilic effect. For rehydrophobisation, the samples are stored in a box directly after plasma treatment. Contact angle measurements are performed after a different rehydrophobisation time for each sample. Figure 5.7 shows the slow rehydrophobisation process, taking place after plasma treatment at standard operating parameters. For 10 minutes past treat-

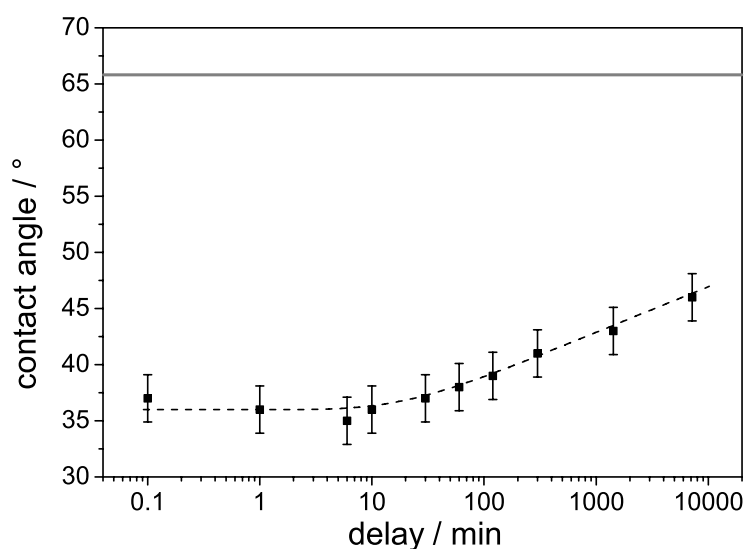


Figure 5.7: Long time hydrophilisation effect of APPJ polymer treatment

ment, the contact angle practically remains unchanged or even decreases further, yet not significantly. Even after 120 hours, the contact angle increases only marginally from initially 37° to 45° . The solid grey line in figure 5.7 indicates the initial contact angle of the untreated samples.

The fundamental experiments described here, clearly demonstrate the practicality of polymer surface hydrophilisation by atmospheric pressure plasma jet treatment. In the following chapters, the influence of parameter variation on the water contact angle of the polymer samples is investigated.

5.2.3.1 Variation of RF-Power

Increasing the RF-input power provides higher energy per oxygen molecule, resulting in a higher O_2 -dissociation degree, as optical TALIF-spectroscopy measurements confirm. The atomic oxygen density at 18 mm distance to the jet's nozzle (see figure 5.8) increases proportionally to the applied RF-power. Contact angle measurements (figure 5.9) show the expected increase in wettability towards higher RF-powers. Towards higher atomic oxygen concentration, the effect saturates.

Variation of RF-power not only changes the atomic oxygen density, but it affects other reactive components in the effluent of the APPJ which might be important for polymer hydrophilisation: As the visible plasma emission intensity rises with increasing RF-power, an increase of UV-radiation can be assumed. Also the metastable oxygen molecule $O_2(a^1\Delta_g)$ -density rises proportionally to the input power [Jeong00]. The ozone density, though, decreases towards higher RF-powers. Two effects counter-

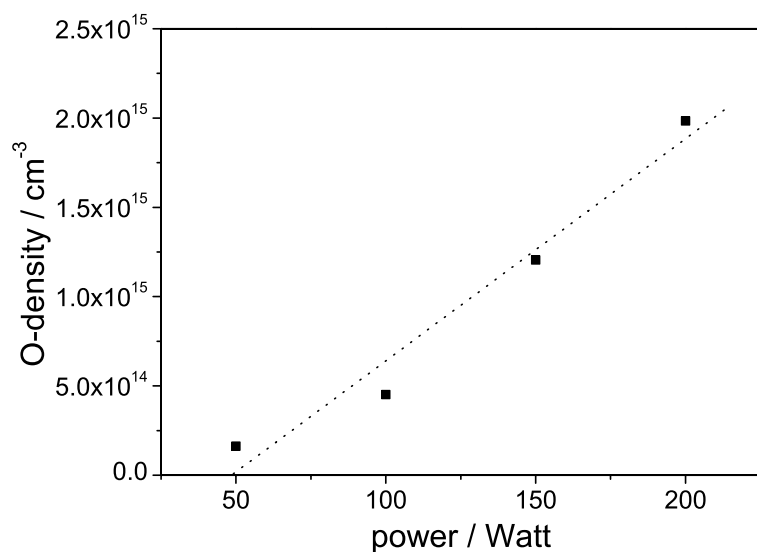


Figure 5.8: Atomic oxygen content in the effluent as a function of input power, measured by TALIF-spectroscopy. Measuring point is 18 mm distance from the jet's nozzle in the centre of the effluent at APPJ standard operating parameters.

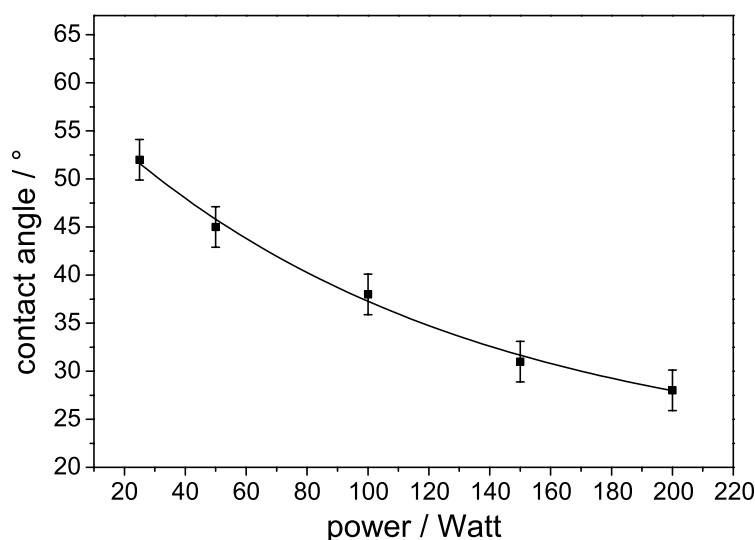


Figure 5.9: Contact angle of distilled water on a polystyrene surface as a function of input power. Samples were treated with the APPJ at standard operating parameters.

act in the O_3 -generation and destruction: more atomic oxygen is produced, therefore more ozone can be generated by collisions of O and O_2 . Higher RF-power and the concomitant higher radiation density, however, lead to a higher O_3 -dissociation in the plasma. The resulting O_3 -density measurements (figure 5.10) show that the dissociative effects prevail and the ozone density decreases towards higher RF-power. It can thus be deduced that ozone has only minor influence on the hydrophilisation of polystyrene.

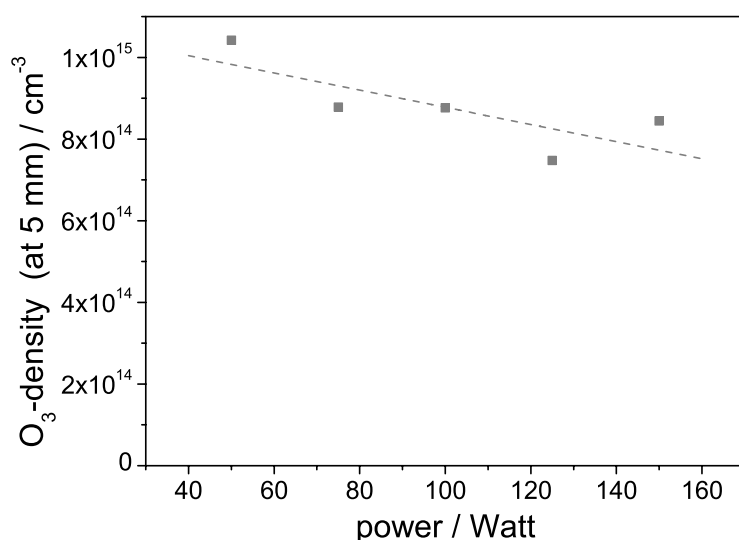


Figure 5.10: Ozone content directly at the jet's nozzle (5 mm distance) as a function of input power. Measuring point is in the centre of the effluent at APPJ standard operating parameters.

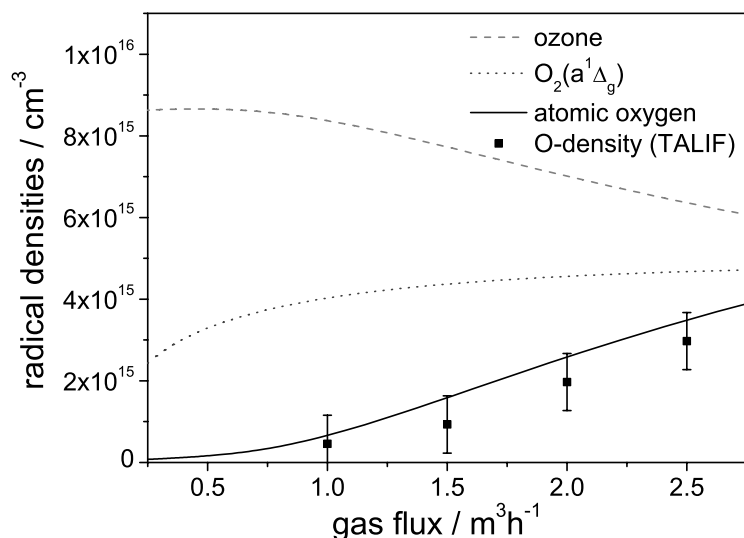


Figure 5.11: Radical density in the effluent at 18 mm distance from the jet's nozzle as a function of total gas flux calculated by the chemical model (see chapter 4.3)

5.2.3.2 Variation of Total Gas Flux

Increasing the total gas flux results in a higher mean gas velocity. Since the time in which the chemical reactions in the APPJ's effluent take place essentially remains constant, a variation of gas velocity has significant influence on the radical densities at fixed distances to the nozzle.

Figure 5.11 shows chemical model calculations (and TALIF-measurements) of atomic oxygen, as well as ozone, and $O_2(a^1\Delta_g)$ -densities at 18 mm distance from the jet's nozzle as a function of total gas flux. The molecular oxygen fraction was kept at 1 vol%. As in the previous measurements, a decrease of ozone density is observed, while atomic oxygen density and $O_2(a^1\Delta_g)$ -density increase. $O_2(b^1\Sigma_g^+)$ -density at 18 mm distance to the nozzle is negligible (see chapter 4.3).

Towards higher gas flux the wettability of polystyrene surfaces is enhanced (see figure 5.12, left y-axis). This was expected from the rise in density of reactive radicals towards higher gas flux. Important to note is the steeper decline of the contact angle at lower gas flux. As could already be seen from input power variation, atomic oxygen and $O_2(a^1\Delta_g)$ can both be considered responsible for polymer surface functionalisation. Remarkable, however, is that with higher gas flux, the progression of contact angle follows inversely the progression of O-density (see figure 5.12). From this it can be concluded that an abundance of atomic oxygen counteracts the hydrophilisation effect. This negative influence of atomic oxygen on polymer hydrophilisation was already proven for the polymeric materials PE and PC by Normand et al. [Normand95].

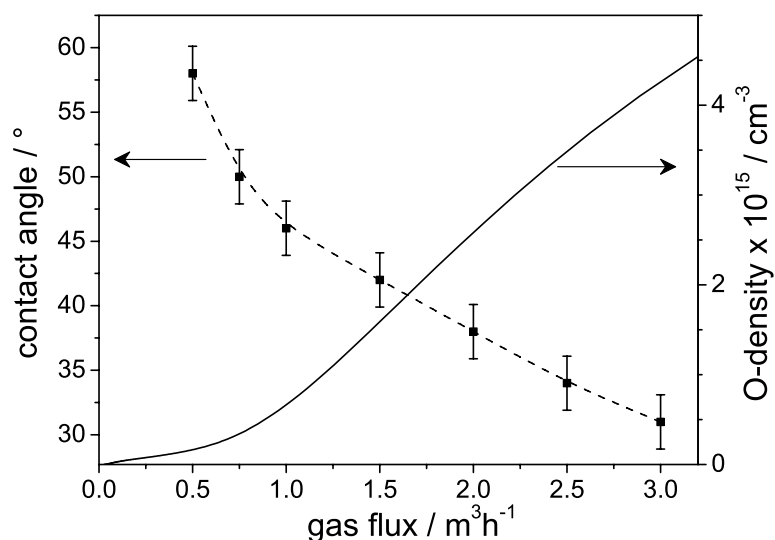


Figure 5.12: Contact angle of distilled water on polystyrene surface (left y-axis) and atomic oxygen density at 18 mm distance from the nozzle determined by chemical model calculations (right y-axis) as a function of total gas flux. Samples are treated at APPJ standard operating parameters.

5.2.3.3 Variation of Oxygen Admixture

Variation of the molecular oxygen admixture helps to understand in detail the influence of $O_2(a^1\Delta_g)$ and atomic oxygen on the wettability of polystyrene. An increase of the molecular component in the APPJ's feed gas is expected to lead to a higher output of reactive radicals. This expectation seems to be confirmed by contact angle measurements (see figure 5.13): With higher O_2 -admixture, the wettability of the polystyrene is increasingly enhanced.

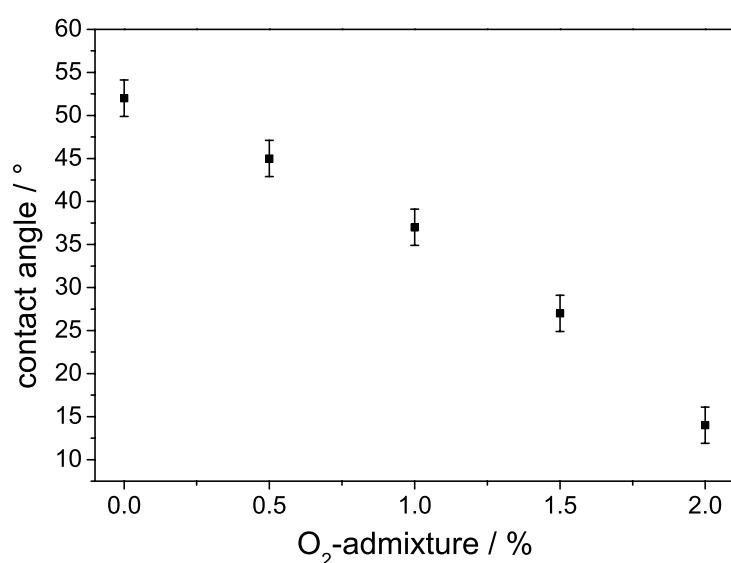


Figure 5.13: Contact angle of distilled water on a polystyrene surface as a function of molecular oxygen admixture. Samples are treated at APPJ standard operating parameters.

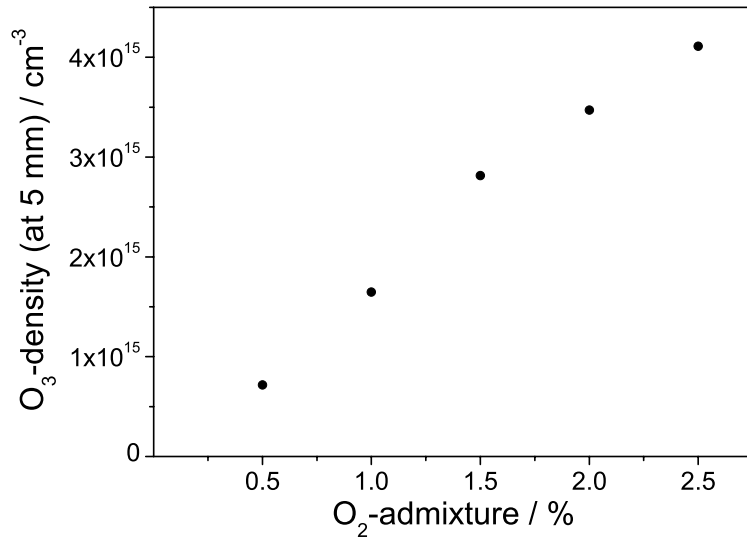


Figure 5.14: On-axis ozone density as a function of O₂-admixture measured at the jet's nozzle (5 mm distance) with UV-absorption spectroscopy at APPJ standard operating parameters

UV-absorption measurements directly at the jet's nozzle show an increase of ozone for higher O₂-admixture (see figure 5.14). Directly at the jet's nozzle also an increase of atomic oxygen density as well as an increase of O₂(a¹Δ_g)-density for higher O₂-admixture is stated in [Jeong00]. TALIF-measurements at 18 mm distance from the jet's nozzle, however, yield unexpected results: With increasing molecular oxygen admixture, the atomic oxygen density decreases (see figure 5.15) linearly on a logarithmic scale.

To understand the mechanisms leading to this decrease of atomic oxygen density at greater distance, the present study performs chemical model calculations for dif-

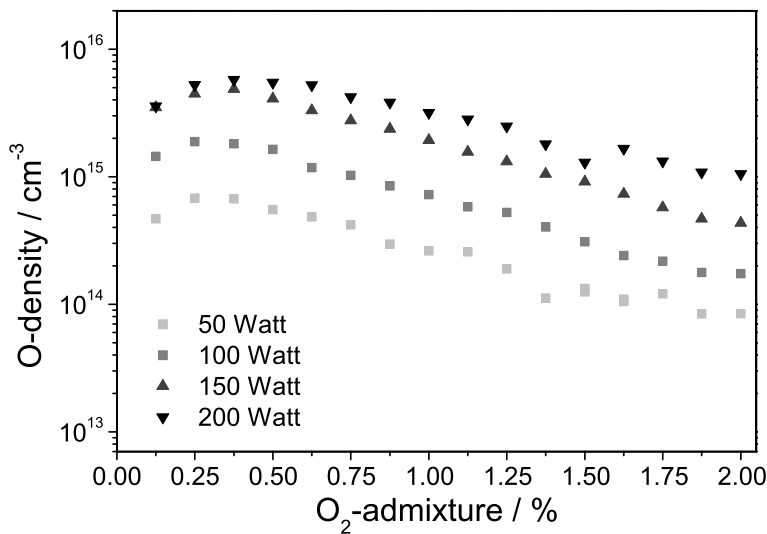


Figure 5.15: Atomic oxygen density at 18 mm distance from the nozzle as a function of O₂-admixture at APPJ standard operating parameters

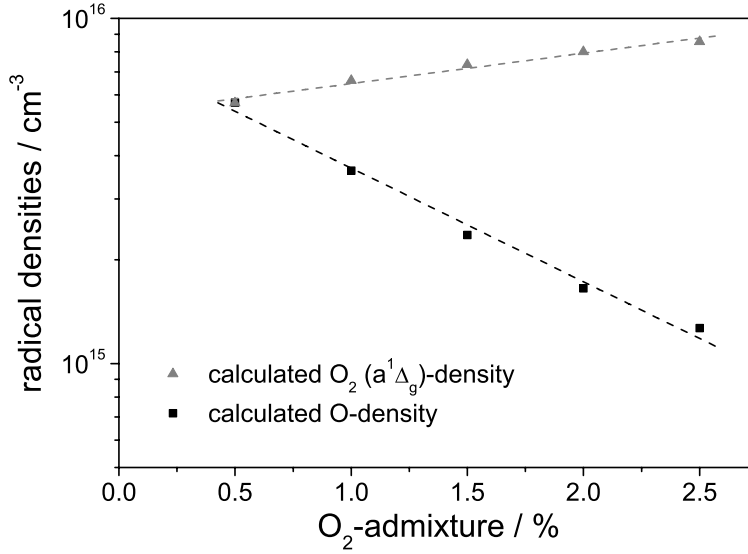
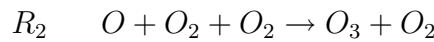
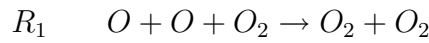


Figure 5.16: Results from chemical model calculations with increasing O₂-admixture at 18mm distance from the nozzle

ferent O₂-admixtures. A linear increase in the initial atomic oxygen density as well as in the initial O₂(a¹Δ_g)-density is assumed as input parameters. The initial ozone density is taken from UV-absorption measurements depicted in figure 5.14.

The chemical model calculations presented in figure 5.16 confirm the results of the TALIF-measurements (figure 5.15): An increase in O₂-admixture with a linear increase in the initial atomic oxygen density leads to a linear decrease on a logarithmic scale of the atomic oxygen density at 18mm distance from the nozzle.

Figure 5.17 explains this unexpected behaviour of the atomic oxygen density. The underlying mechanisms is as follows: A higher O₂-density results in more collisions of atomic oxygen with oxygen molecules. These collisions increase the recombination of the oxygen atoms according to reactions R₁ and R₂ in the chemical model (see chapter 4.3):



This subsequently leads to a quicker decrease of the on-axis O-density for higher O₂-admixtures.

Variation of RF-power in chapter 5.2.3.3 proved ozone to be of minor importance for hydrophilisation of polystyrene. Thus the metastable O₂(a¹Δ_g) as only other main reactive component rising with increasing oxygen admixture is identified to play a major role in polystyrene treatment. Similar findings for polyethy-

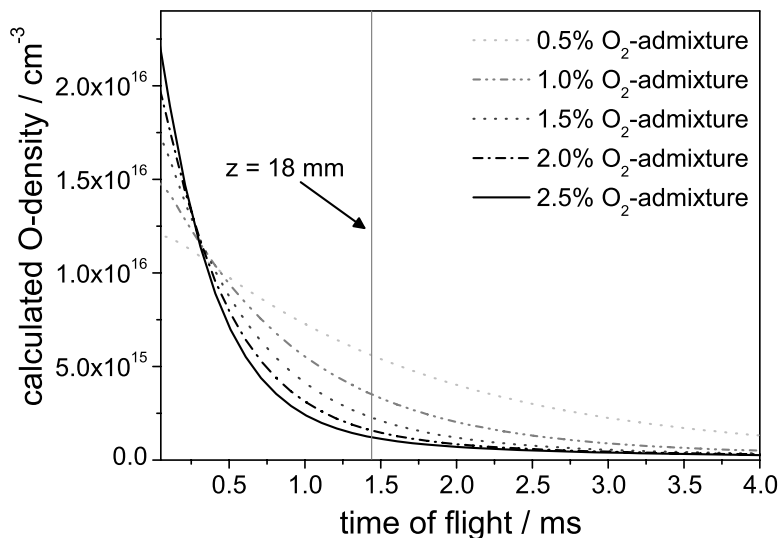


Figure 5.17: Results from chemical model calculations. A higher O₂-admixture leads to a faster decay of the atomic oxygen density in the downstream flow.

lene and polycarbonate treatment have been described by Normand and coworkers [Normand95]. The polystyrene surface is hydrophilised as follows: Polymer chains are broken by atomic oxygen. Subsequently, ground state and metastable O₂ form functional groups, necessary for a hydrophilic surface. (These functional groups might then again be destroyed by excess atomic oxygen.)

By this sequence of processes during polystyrene hydrophilisation, the accelerated functionalisation towards higher oxygen admixture can be explained: With increasing O₂-admixture, the density of the destructive atomic oxygen (at 18 mm distance from the jet's nozzle) decreases, while the density of the productive O₂ and O₂(a¹Δ_g) increases. Even with an O₂-admixture of more than 2 vol%, the atomic oxygen density in the effluent is, however, still sufficiently high for polymer bond breaking.

Also the saturation behaviour of the contact angle with rising RF-power can be explained (see chapter 5.2.3.1). The towards higher RF-power increasing atomic oxygen density reduces the surface hydrophilisation, leading to saturation.

In future studies it needs to be reconsidered whether ozone might yet have an influence due to the following presumed mechanism: The sample placed into the effluent provokes a change of the effluent flowfield. As a „foreign body“ it stems the effluent's flux (as was shown in flow model calculations for a thermal jet by Wang et al. [Wang07]) and might cause an accumulation of radicals directly at the polymer surface. A dissociation of built up ozone by (V)UV-radiation (see e.g. [Takahashi98, Cole06]) could lead to an increase of atomic oxygen directly at the

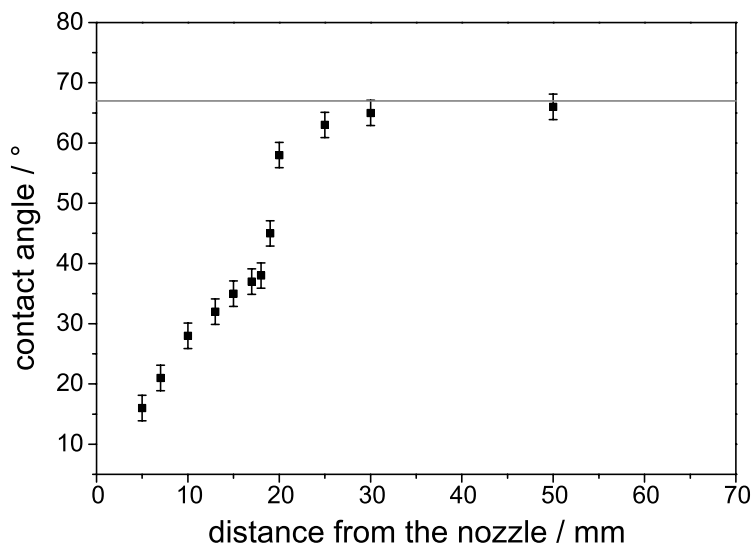


Figure 5.18: Contact angle of distilled water on a polystyrene surface as a function of distance from the sample to the jet's nozzle. The solid line indicates the initial contact angle. Samples are treated at APPJ standard operating parameters.

sample's surface. For a more detailed investigation of these processes, in-situ TALIF-measurements with an obstructed effluent are planned to be performed at the Ruhr-University Bochum.⁶

5.2.3.4 Variation of Sample-Nozzle-Distance

A variation of the sample to nozzle distance is expected to produce the same results as variation of gas flux. In the wettability experiments with varying gas flux (chapter 5.2.3.2), the polystyrene sample was held at a fixed distance to the jet's nozzle, while the chemically active radicals were transported faster to the sample with higher gas flux. Moving the sample towards the radicals leaving the jet's nozzle – at fixed gas flux – is expected to show identical hydrophilisation effects as the faster transport of the radicals to the sample.

Figure 5.18 indeed shows a strong dependency of the contact angle on the sample-nozzle distance. Starting at 5 mm from the nozzle, the contact angle exponentially increases with higher distance, as can be expected from the exponentially decreasing radical densities (with the exception of the ozone density, see chapter 4.3.3.1). At about 20 mm from the nozzle, however, a sharp discontinuity in the progression of the contact angle can be observed. This discontinuity cannot be explained by any of the previous investigations and also this observation differs significantly from results of wettability measurements with varying gas flux.

⁶Institute for Experimental Physics II, Ruhr-University Bochum – Prof. Dr. J. Winter / Dr. V. Schulz-von der Gathen (www.ep2.ruhr-uni-bochum.de).

An explanation for these unexpected results can be found in a closer examination of the chemically active species in the APPJ's effluent. In contrast to the radicals, the photon distribution is mainly independent of the gas flux. Although VUV-radiation is usually absorbed in air, VUV- and UV-radiation is transported in the helium-atmosphere generated by the APPJ, and can be detected in the effluent still at a considerable distance to the nozzle (see chapter 4.2.2). In the following, a closer look is taken at the APPJ's (V)UV-radiation emission intensity as a function of distance to the nozzle.

The effect of (V)UV-radiation on polymer surfaces is known and has already been used for surface functionalisation [Fozza99, Dhayal06]. The influence of UV- or VUV-radiation in plasma surface modification of polymers has been investigated by a number of researchers who came to the conclusion that oxidation of polymer surfaces by oxygen atoms is greatly enhanced when the surface is concurrently illuminated by UV-photons [Strobel03, Schrader92]. (V)UV-radiation enhances the generation of functional groups in the polymer not only by dissociation of molecular oxygen into reactive atomic oxygen [Lee77, Nee97] but also by breaking of polymer chains in the irradiated surface [Gejo06]. A comparison of the absorption profile of polystyrene with the APPJ's (V)UV-emission spectrum, as depicted in figure 5.19, makes obvious

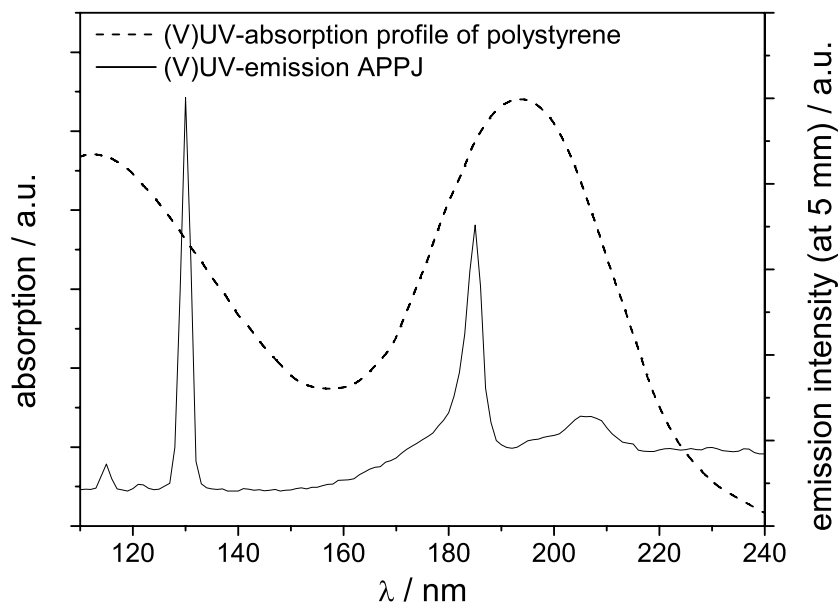


Figure 5.19: (V)UV-absorption of polystyrene [Fozza99] and (V)UV-emission intensity of the APPJ at 5 mm distance from the nozzle, looking head-on into the discharge

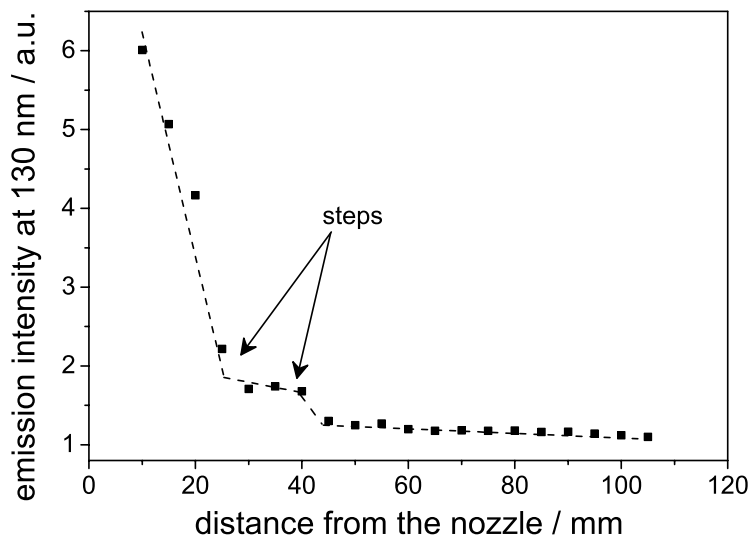


Figure 5.20: 130 nm VUV-emission line from figure 5.19 as a function of distance from the nozzle

the importance of (V)UV-radiation in the APPJ's effluent for hydrophilisation of polystyrene. The emission maxima of the (V)UV-spectrum correspond exceptionally well to the absorption maxima of the (V)UV-absorption curve of polystyrene. The emission peak at 130 nm can be attributed to the $O(^3S^0 \rightarrow ^3P)$ -transition. The features at about 180 to 220 nm are due to molecular oxygen. The APPJ's (V)UV-emission spectrum was measured with the setup depicted in figure 4.14 (see chapter 4.2.2). VUV-radiation below 120 nm is emitted from the APPJ, but can not be detected due to the transmission cut off of the MgF_2 -window used for the (V)UV-spectroscopy measurements.

Figure 5.20 shows the APPJ's VUV-radiation at 130 nm as a function of distance to the nozzle. The most prominent structures in this graph are a steep linear decline followed by a drastic change of the slope at about 20 mm distance from the jet's nozzle. These results correspond to the step already observed in contact angle measurements (figure 5.18). In the following, this behaviour will be explained.

While TALIF-measurements of the effluent's atomic oxygen density as described in chapter 4.1 were performed on the APPJ operated at atmospheric pressure in a recipient with a controlled helium atmosphere, the plasma treatment investigated here as well as (V)UV-emission spectroscopy are performed at ambient conditions. Comparative studies on both experimental setups are expected to indicate a possible source for the discontinuity observed in (V)UV-emission measurements as well as in the contact angle measurements.

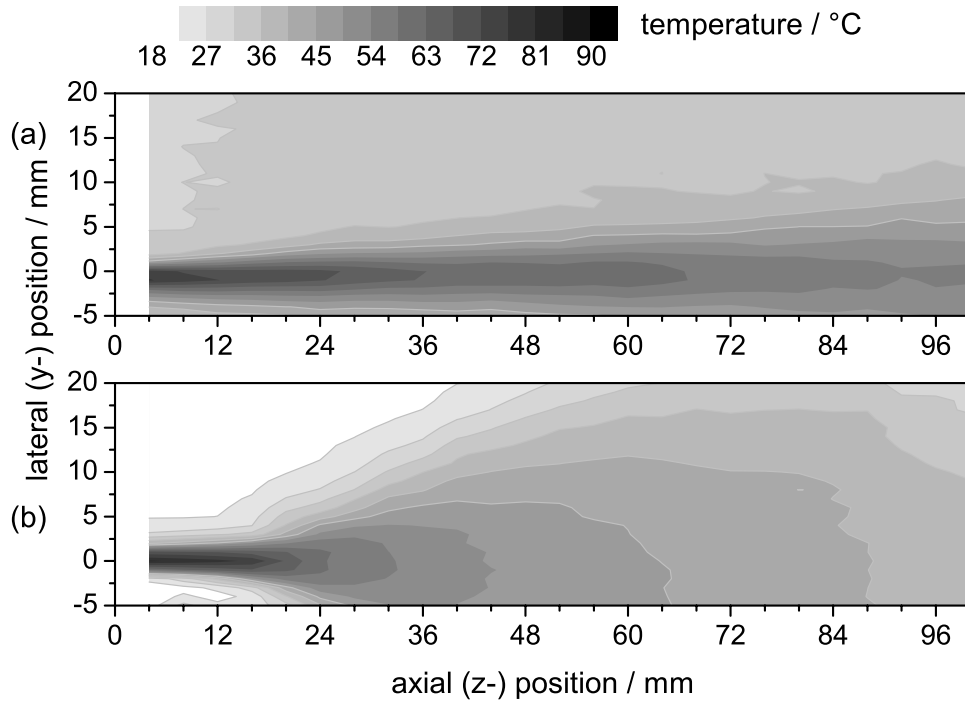


Figure 5.21: Temperature map of the APPJ operated in helium atmosphere (a) and operated in ambient conditions (b) (measurement perpendicular to the discharge gap at a centered position)

Figure 5.21 shows a comparative study of the temperature distribution in the effluent of the APPJ operated in helium (a) and in air (b). All other operating conditions are held constant.

A striking difference to be observed in the temperature field measurements is a spreading of the effluent starting at around 20 mm from the nozzle of the jet when operated in ambient conditions, whereas the effluent of the jet operated in helium atmosphere stays confined over the entire length measured. In the following it will be demonstrated how this spreading structure is not only to be observed for the temperature map, but more importantly, also for the radical density distribution. TALIF-measurements in ambient conditions are prohibited due to unknown quenching partners introduced by the surrounding air, which make a calibration of the measured signals impossible. Also striae in the effluent would obscure the TALIF signals. Therefore, comparing measurements on ozone are used to study the radical distribution in the effluent.

The ozone density in the effluent of the APPJ operated in ambient conditions is measured according to chapter 4.3.3.1. A spatially resolved map of the ozone

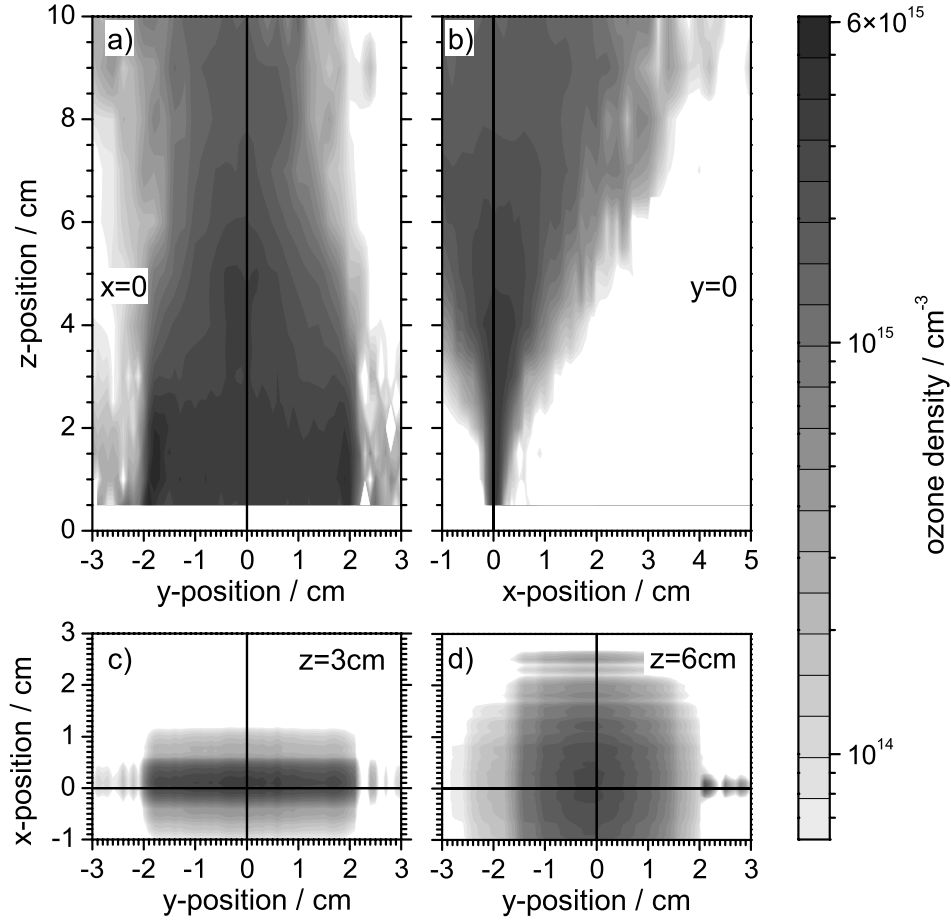


Figure 5.22: Ozone density map of the APPJ operated in air. a) and b) show yz - and xz -cross sections of the effluent, c) shows a xy -cross section at a distance of 3 cm from the jet's nozzle, d) shows a xy -cross section at 6 cm distance from the jet's nozzle.

concentration is obtained from two transverse scans performed for distances up to 10 cm from the nozzle in x - and y -direction with a step-width of 0.2 mm. The upper two subfigures a) and b) of figure 5.22 show yz - and xz -cross sections of the effluent, the lower two subfigures c) and d) show xy -cross sections at $z = 3$ cm and $z = 6$ cm respectively. It can be observed that turbulence is setting in at a distance of about 2 cm from the nozzle (see figure 5.22 b)), so that mixing with the ambient air might occur. Up to that point the cross section of the ozone flow has a rectangular shape (see figure 5.22 c)). Beyond this point the flow spreads and soon transforms into a beam of circular shape (see figure 5.22 d)).

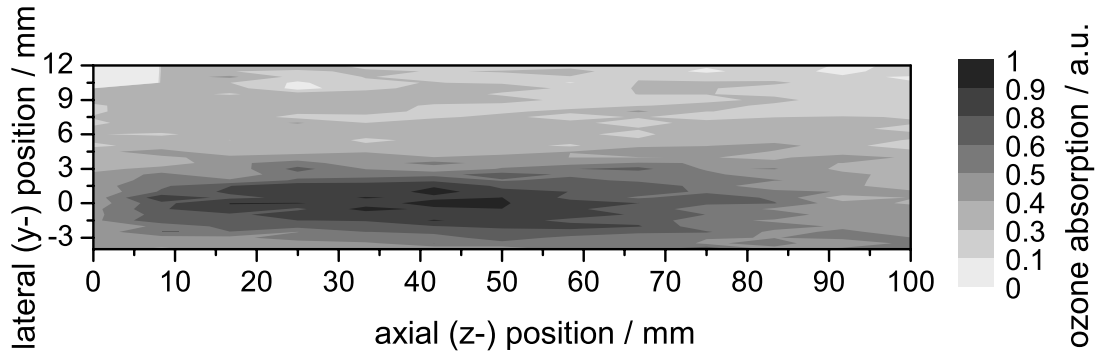


Figure 5.23: Ozone density map of the APPJ operated in helium in the same recipient as for the TALIF-measurements of the atomic oxygen density

To confirm that this spreading effect is in fact connected to the ambient operating conditions and is not characteristic for the ozone distribution alone, UV-absorption measurements are performed on the APPJ operated in helium atmosphere, in the same recipient as for the TALIF-measurements of the atomic oxygen density (see figure 4.1). This setup requires a considerable distance between the UV-lamp and the detecting spectrograph and thus results in a rather low transmitted light intensity and a rather high signal to noise ratio. Absorption signals are too low to be measured perpendicular to the jet's plane so that absorption can only be measured parallel to the jet's plane.

A relative total absorption map is shown in figure 5.23. Despite the high noise-fraction, the ozone absorption map indeed shows that when operated in a helium atmosphere, the ozone concentration stays confined in the same way as the atomic oxygen density distribution (figure 4.12) as well as the temperature distribution of the effluent (figure 5.21a)). The expansion of the radical distribution in the effluent of the jet corresponds in structure to the temperature distributions.

From above results, the following can be concluded: When the APPJ is operated in air, turbulence sets in at about 2 cm distance from the nozzle and the effluent rapidly expands. This has significant impact on the particle density distribution in the effluent. Although the plane integrated ozone density rises with greater distance to the nozzle (as was predicted from the chemical model calculations, see figure 4.28), the on-axis ozone density decreases due to ozone transport lateral to the gas flux (see figure 5.24). Corresponding distributions can be assumed also for the remaining radicals in the effluent.

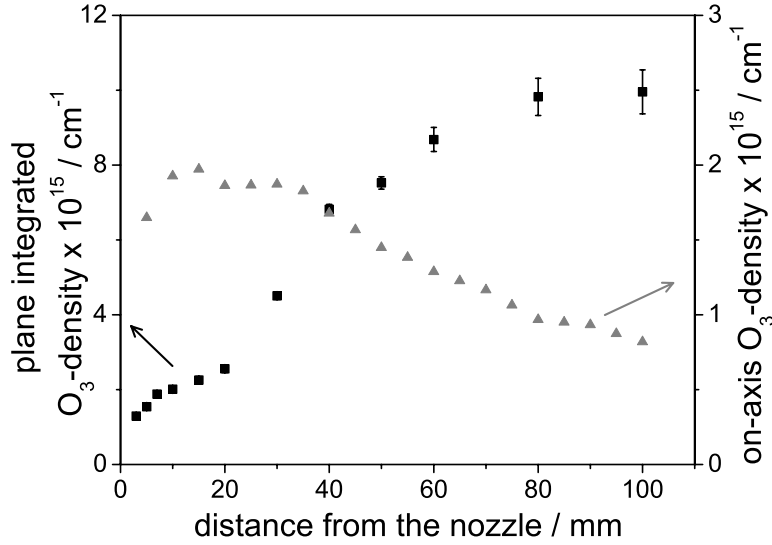


Figure 5.24: Plane integrated and on-axis ozone density as a function of distance from the nozzle

The stepwise decrease of the on-axis oxygen radical densities has a strong influence on the VUV-radiation at 130 nm (depicted in figure 5.20): At high radical densities directly at the nozzle, VUV-radiation is quickly absorbed. At 20 mm, with the rapid drop in radical density, the VUV-radiation is significantly less absorbed. The second step in the VUV-emission distribution (see figure 5.20 at around 40 mm) can be attributed to increased absorption by air flowing into the effluent.

The described measurements and comparative investigations show that the discontinuity in contact angle as a function of distance to the nozzle (figure 5.18) correlates with the structural step in the effluent of the APPJ operated in ambient conditions and the concomitant drop in reactive species densities.

5.3 Conclusion

The atmospheric pressure plasma jet (APPJ) is an excellent plasma source for surface treatment due to its high radical density and low gas temperature in the effluent. The parameter study, correlating the oxygen radical densities (O, O₂^{*}, O₃...) in the APPJ's effluent with polystyrene surface hydrophilisation, analysed by contact angle measurements, yields information on the processes occurring in plasma treatment: The atomic oxygen density has been identified to have a strong influence on surface functionalisation (here: hydrophilisation) of polymers, since atomic oxygen leads to breaking of polymer chains in the treated surface. The broken polymer chains can subsequently be turned into functional groups by (ground state and

metastable) molecular oxygen. Too much atomic oxygen in the effluent, however, counteracts the desired effect and leads to a decrease in functionalisation by immediately destroying the newly built functional groups. This sequence of processes during polystyrene hydrophilisation explains the saturation behaviour of the contact angle with rising RF-power, as well as the accelerated functionalisation towards higher molecular oxygen admixture. Compared to atomic oxygen and $\text{O}_2(\text{a}^1\Delta_{\text{g}})$, ozone is of minor importance for polystyrene hydrophilisation. For future investigations TALIF-measurements directly in front of treated surfaces promise further insight into the mechanisms occurring during surface treatment.

Chapter 6

Improving the APPJ's Atomic Oxygen Output

From the previous chapters it is known that atomic oxygen in the jet's effluent plays a substantial role for possible applications of the APPJ. Despite the complex chemical effects described for polystyrene treatment in chapter 5, for most applications a maximal atomic oxygen density is essential. Therefore, improving the atmospheric pressure plasma jet means increasing its atomic oxygen output at the same input power and feed gas supply. The strong influence of the electrode material on the atomic oxygen density, observed in this chapter, leads to a modification of the APPJ: The jet's bare metal electrodes are coated with a thin dielectric SiO_2 -layer. This new dielectric barrier APPJ (DB-APPJ) is compared to the original APPJ. The homogeneity of both discharges is investigated via voltage and current measurements as well as by phase resolved optical emission intensity measurements. The atomic oxygen generation efficiency is determined by measuring the absolute atomic oxygen ground state density in the effluent by two-photon absorption laser induced fluorescence (TALIF) spectroscopy.

6.1 Atomic Oxygen Generation in the Plasma

For an improvement of the APPJ's atomic oxygen generation efficiency, a closer look at the atomic oxygen production inside the discharge region is necessary. In the following, the influence of the electrodes' walls on the atomic oxygen output is analysed by increasing the volume to wall ratio.

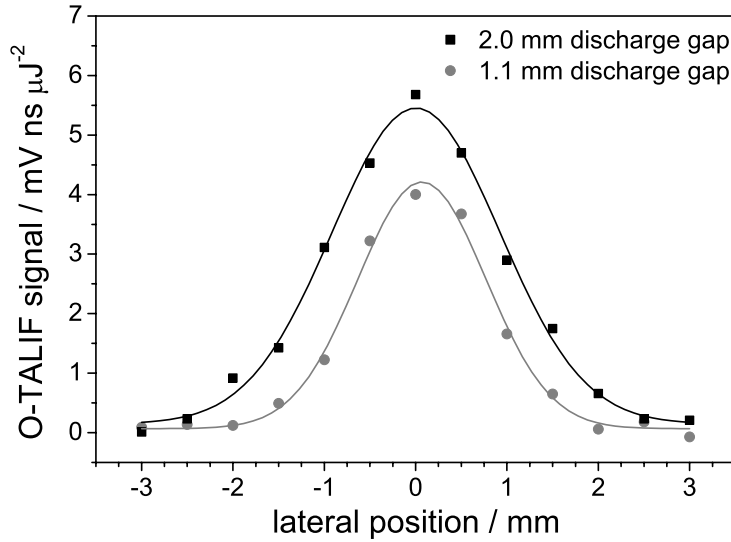


Figure 6.1: Normalised TALIF-signal profile measured at 12 mm distance from the jet's nozzle perpendicular to the discharge gap

6.1.1 Influence of the Electrode Surface Material

To investigate the influence of the electrode surface material on the APPJ's atomic oxygen output, the influence of the electrode walls is decreased by changing the discharge gap from 1.1 mm to 2 mm in order to increase the volume to wall ratio: An increase in the atomic oxygen output is expected, since atomic oxygen loss due to sticking and recombination processes of atomic oxygen on the bare metal electrode walls is reduced. Figure 6.1 shows two comparing TALIF-signal profiles at 12 mm distance from the APPJ's nozzle measured perpendicular to the discharge gap with constant operating parameters. The TALIF-signal profiles prove indeed that the atomic oxygen density in the central position is increased by 40% for a larger discharge gap.

Figure 6.2 shows VI-characteristics of both setups (1.1 mm and 2 mm discharge gap) in comparison. No drastic change is observed. The transition to a γ -mode discharge for the APPJ with a large discharge gap occurs at higher currents, but the recovering to the α -mode discharge occurs at about the same current as for the APPJ with the smaller discharge gap.

It can be concluded that the electrode walls indeed have a significant influence on the APPJ's atomic oxygen output. By changing the electrodes' surface material, in the following, further improvement of the atomic oxygen generation efficiency is investigated.

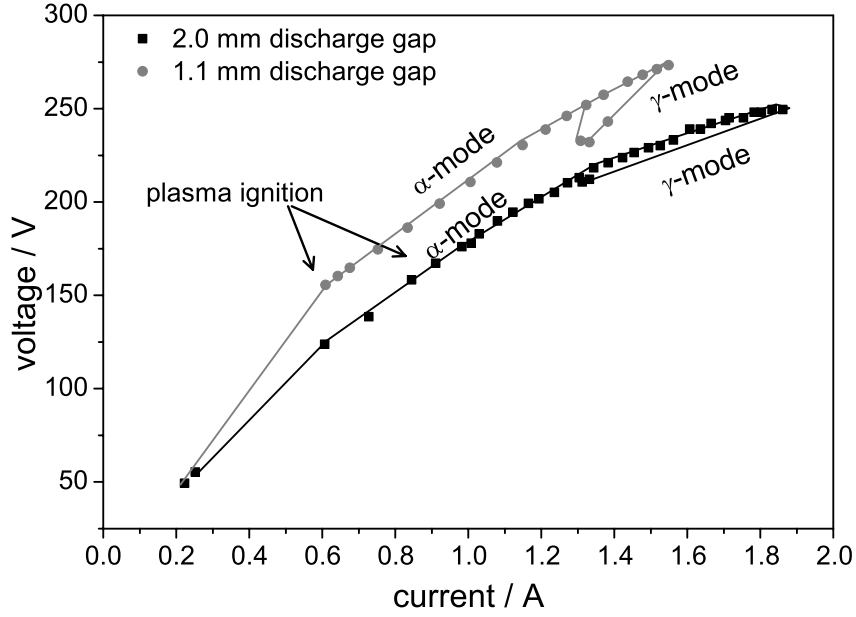


Figure 6.2: VI-characteristic of APPJ with small discharge gap (1.1 mm) and large discharge gap (2 mm)

6.2 The Dielectric Barrier APPJ

In order to reduce sticking of atomic oxygen to the electrode walls and thus reduce atomic oxygen loss by recombination, the material of the APPJ's electrode walls is changed from stainless steel – having a high sticking coefficient for atomic oxygen – to SiO_2 , a material with an extremely low sticking coefficient for atomic oxygen. The recombination coefficient for atomic oxygen on SiO_x was measured in several previous studies, ranging from 0.2×10^{-4} [Macko04, Magne93] to 2.4×10^{-3} [Pagnon95]. The recombination coefficient for atomic oxygen on stainless steel was determined higher by orders of magnitude, ranging from 0.07 [Mozeti00] to 0.14 [Kiehlbauch03] and 0.17 [Singh00]. The applied thin SiO_2 -layers, which are expected to enhance the APPJ's atomic oxygen output, constitute a dielectric barrier. By coating the electrodes with a dielectric, the APPJ is technically modified to what is generally referred to as atmospheric pressure glow discharge (APGD) [Roth07, Bogaerts02]. In this study, however, the modified jet will be referred to as dielectric barrier APPJ (DB-APPJ), due to its affinity to the regular APPJ.

In the following, the influence of the dielectric barriers on the discharge is investigated by phase resolved optical emission intensity measurements, OES and electric measurements, and by TALIF-measurements. It will be shown that the discharge

mode is unaltered by the electrode modifications. This can be explained by the physical properties of an α -mode RF-glow discharge, in which the plasma sheaths conduct no current, and the conduction current through the plasma is connected to the electrodes exclusively by the displacement currents [Raizer95]. Bare metal electrodes therefore behave as impassively as dielectrics. The APPJ and the DB-APPJ are expected to exhibit the same glow discharge.

6.2.1 Electrode Modification

A thin SiO_2 -layer is deposited to a thickness of 230 nm onto the electrodes' surface by an anodic vacuum arc [Ehrich88]. Only the side facing the plasma is coated. Coverage of the electrodes is tested by immersing the coated area into salt-water and measuring the coating's resistance with a multimeter. The resistance exceeds the multimeter's measurement range and is higher than 10 M Ω . This proves that the layer covers the entire area and exhibits no cracks. After 37 hours operation of the SiO_2 -modified DB-APPJ at 150 Watt, 2 m³/h helium flux and an admixture of 0.5 vol% molecular oxygen, the SiO_2 -layer is analysed with a reflectance spectrometer. Subsequently, the layer's thickness is determined by fitting a spectrum calculated by Fresnel's equations – with the film thickness as fitting parameter – to the measured spectrum (figure 6.3), neglecting absorption and substrate background reflection. For thin film thickness determination see e.g. [Reuter03, Heimann04]. A refractive index of 1.46 for SiO_2 is assumed. Despite etching in the plasma, the film's thickness still measures 175 nm after 37 hours of operation.

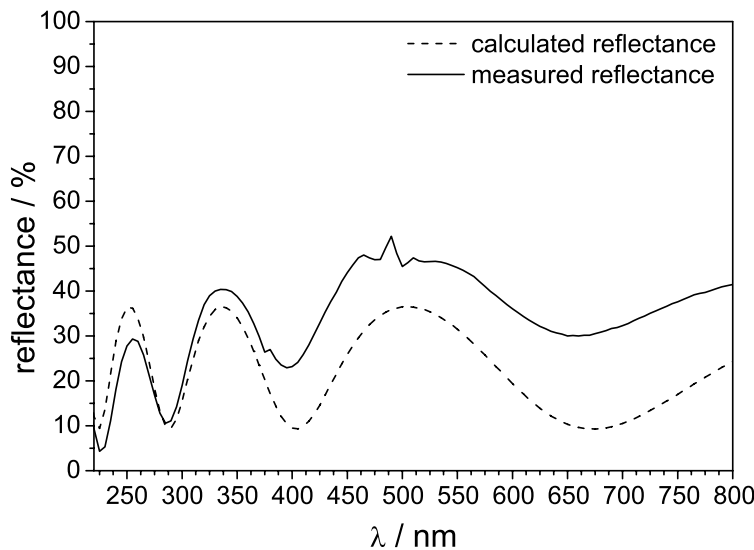


Figure 6.3: Measured and calculated reflectance spectrum of the SiO_2 -layer after 37 hours of operation at 150 Watt and 2 m³/h helium flux with 0.5 vol% O_2 -admixture

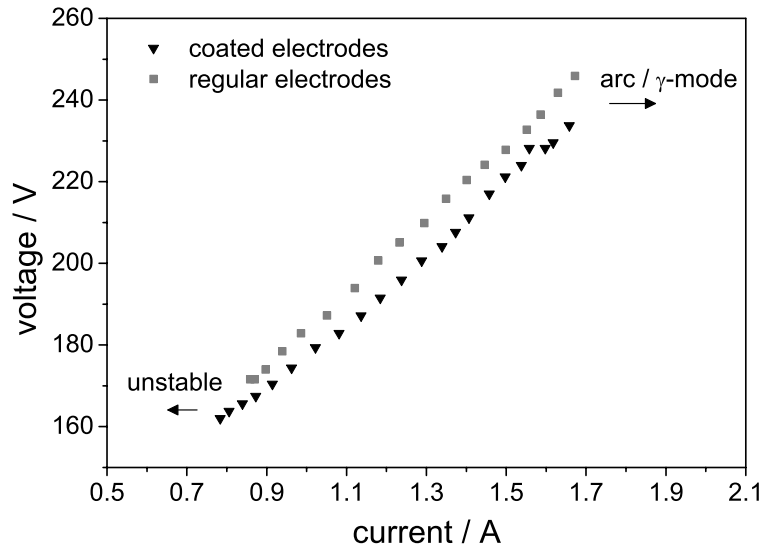


Figure 6.4: VI-characteristic of regular APPJ (with bare metal electrodes) and DB-APPJ (with SiO₂-coated electrodes) in comparison

6.2.2 Discharge Characteristics

VI-characteristics of regular APPJ and DB-APPJ, measured with the setup described in chapter 3.3, using a Gould 6064 oscilloscope with 500 MHz bandwidth, are shown in figure 6.4. Progression of voltage with current is identical for both discharges within the accuracy of the electric measurements.

Figure 6.5 shows normalised optical emission spectra of the discharge region of the regular APPJ and the DB-APPJ. Both spectra are very similar, showing the helium line at 706 nm and two atomic oxygen lines at 777 nm and 844 nm. The slightly higher intensity ratio of the oxygen peaks to the helium peak in the spectrum of the

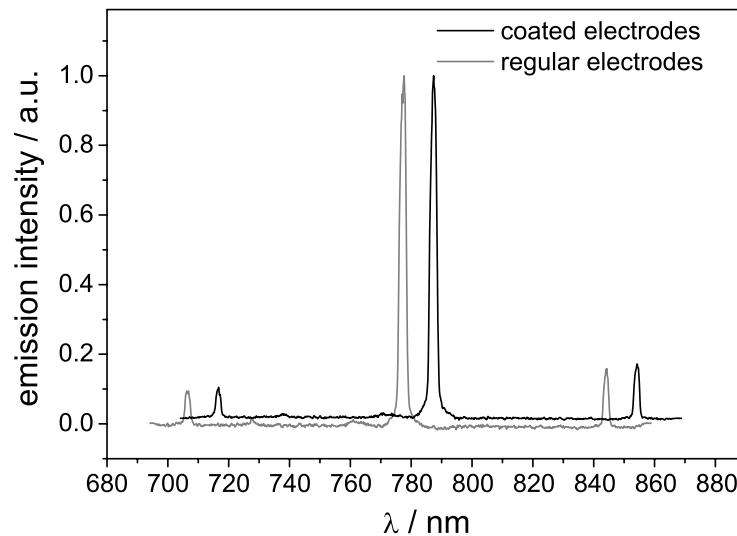


Figure 6.5: Normalised optical emission spectra of the regular APPJ (with bare metal electrodes) and the DB-APPJ (with SiO₂-coated electrodes). For a better distinction, the spectrum of the DB-APPJ's discharge is shifted by 10 nm towards higher wavelengths.

DB-APPJ shows that a higher oxygen output can be expected from this modified plasma jet.

6.2.3 Phase and Space Resolved Emission Imaging

The phase and space resolved plasma intensity of the respective discharge regions is recorded with an optical spectroscopy multichannel analyser (OSMA, already described for the OES-measurements in chapter 2.1.3). A schematic of the setup is depicted in figure 6.6. The discharge region is imaged onto the 1024 pixel of the OSMA's photo diode array, resulting in a spacial resolution of 0.08 mm. The OSMA detector head is connected to an FG-100 gate pulse generator, with which a gate pulse of ≥ 8 ns can be achieved (see figure 6.7). The gate pulse generator is triggered by a DG535 pulse delay generator, which is synchronised to the TTL-out signal of the RF-generator. Phase resolved measurement is realised by gating the OSMA with a gate width of ≥ 8 ns synchronised to the APPJ's excitation frequency of 13.56 MHz. After recording an image, the gate is delayed with respect to the trigger by 8 ns. The process is performed repeatedly. By this method one excitation cycle of about 74 ns is resolved into ~ 8 ns time intervals yielding five images of the discharge from the respective phase position.

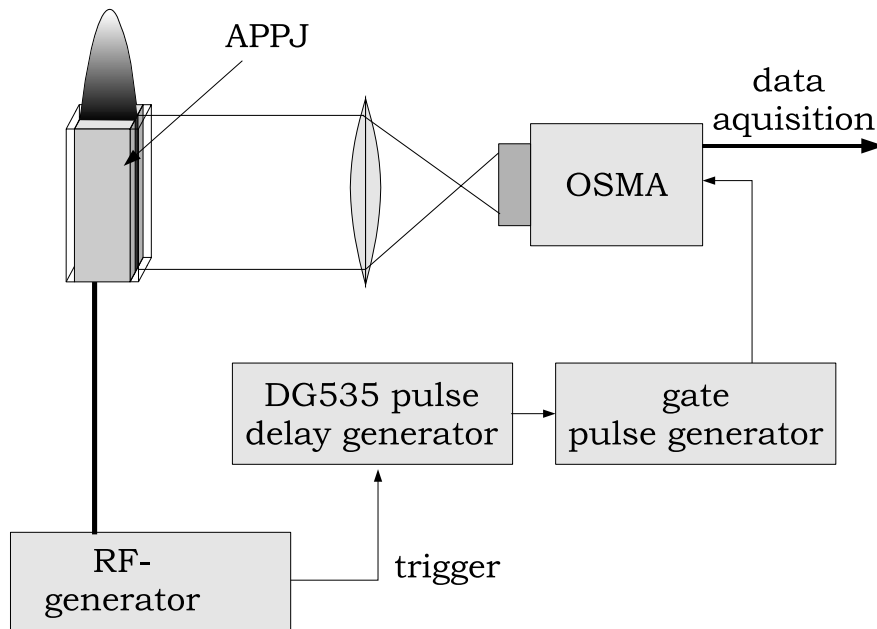


Figure 6.6: Experimental setup of the space and time resolved plasma emission intensity measurements

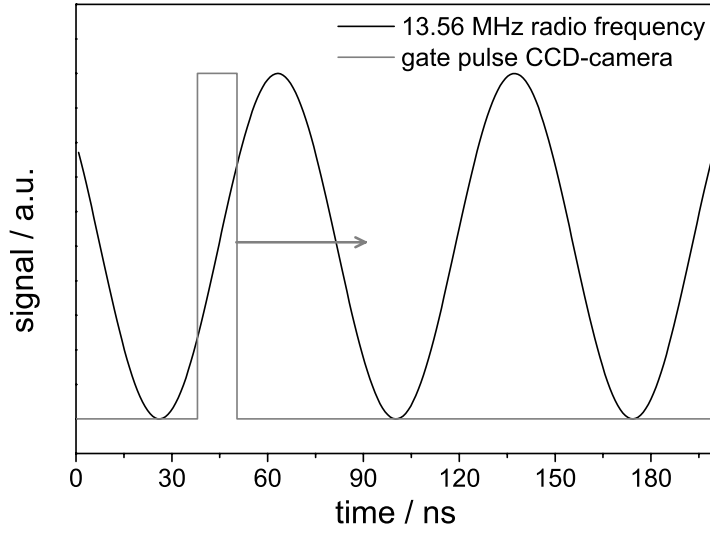


Figure 6.7: Gate pulse of pulsed operation of the OSMA triggered to the 13.56 MHz RF-power signal

The resulting measurements are presented in figure 6.8. On the figure's left side, the phase resolved emission intensity of the DB-APPJ can be seen and on the figure's right side, the phase resolved emission intensity of the APPJ with bare metal electrodes is shown. Capital to note is the fact that the images are taken with only a single shot and no averaging measurements were performed. This accounts for the noise in the images. The emission intensity images were captured over a range of one

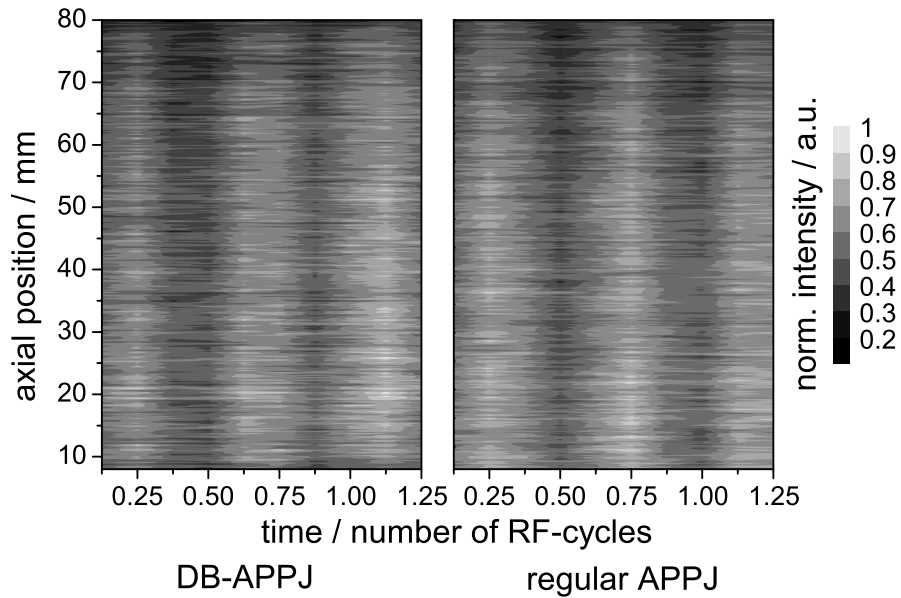


Figure 6.8: Normalised plasma emission intensity as a function of RF-cycles of DB-APPJ (left) and of regular APPJ (right)

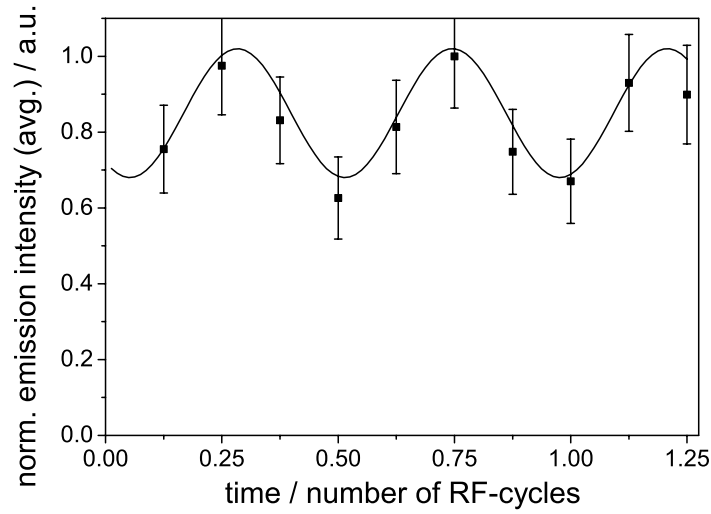


Figure 6.9: Normalised plasma emission intensity as a function of RF-cycle measured on the regular APPJ averaged over the length of the discharge region

RF-cycle. Two intensity maxima during one RF-cycle can be seen, due to excitation at one electrode in the first half of the RF-cycle, and subsequent excitation at the other electrode in the second half of the RF-cycle.

Figures 6.9 and 6.10 present an evaluation of the images from figure 6.8. The mean emission intensity averaged over the electrode length as well as the variance of the emission intensity distribution are shown together with a sinusoidal fit. Both discharges – regular APPJ with bare metal electrodes and DB-APPJ – exhibit identical emission intensity images during an RF-cycle. The variance of the DB-APPJ images is not higher than the one of the regular APPJ with bare metal electrodes, contrary to what would be expected if the DB-APPJ's discharge consisted of streamers as is the case in a regular dielectric barrier discharge (DBD).

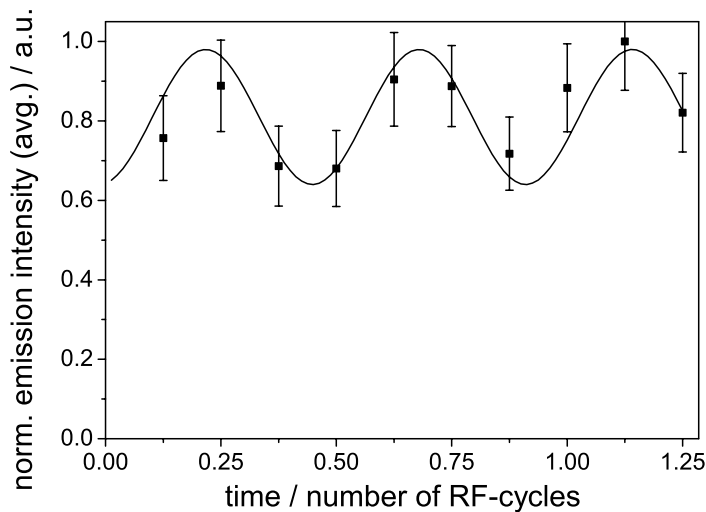


Figure 6.10: Normalised plasma emission intensity as a function of RF-cycle measured on the DB-APPJ averaged over the length of the discharge region

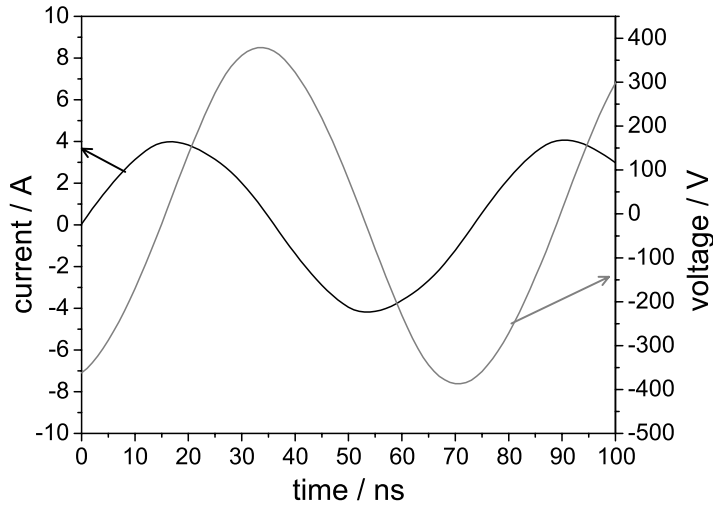


Figure 6.11: RF-cycle of the regular APPJ operated in helium at 150 Watt

An according observation can be made for voltage and current waveforms. In a DB-discharge with streamers, current spikes for each streamer are characteristic. The current and voltage waveforms of the DB-APPJ with coated electrodes do not differ from the ones of the regular APPJ with metal electrodes, and exhibit no spikes (see figures 6.11 and 6.12).

Summarising the investigations, it can be concluded from both, the phase resolved optical emission intensity measurements and the current/voltage measurements, that the DB-APPJ discharge produces exactly the same homogeneous glow discharge as the regular APPJ with bare metal electrodes.

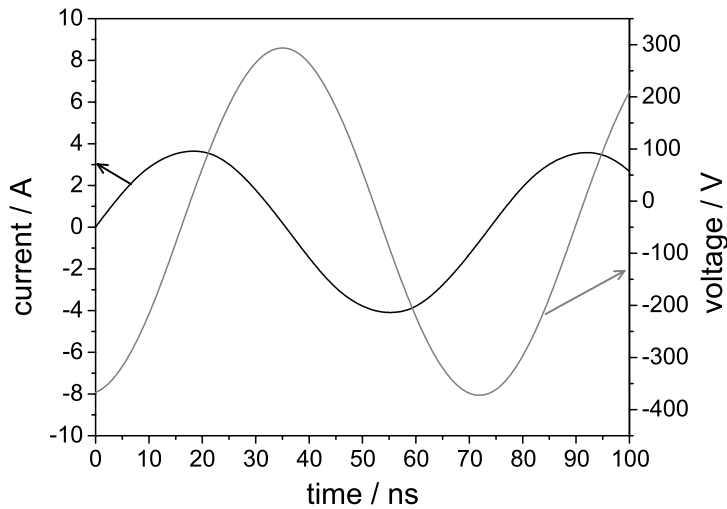


Figure 6.12: RF-cycle of the DB-APPJ operated in helium at 150 Watt

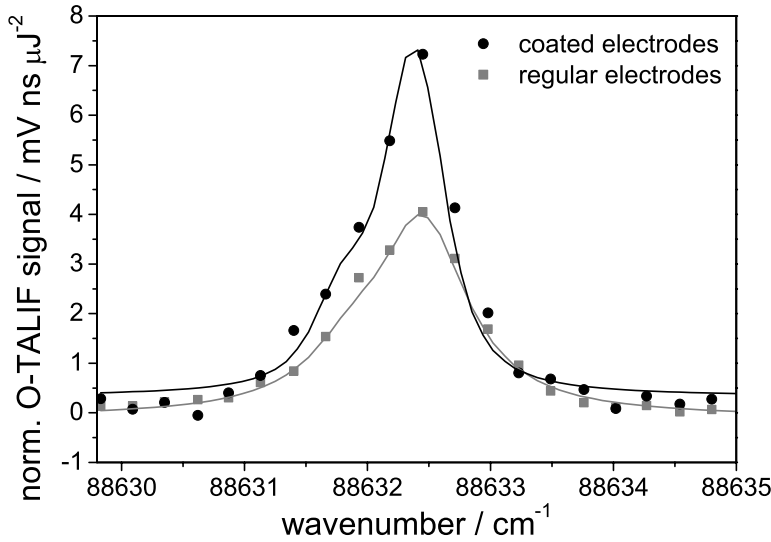


Figure 6.13: Normalised TALIF-signal of the regular APPJ (with bare metal electrodes) and the DB-APPJ (with SiO₂-coated electrodes)

6.2.4 Atomic Oxygen Production Efficiency

The atomic oxygen output of regular APPJ and DB-APPJ is investigated by TALIF-spectroscopic measurements. Both discharges are operated at 150 Watt at 2 m³/h helium flux with 0.5 vol% O₂-admixture. The measuring point is on-axis at 12 mm distance from the nozzle. The TALIF-signals in figure 6.13 demonstrate that decreasing atomic oxygen recombination at the electrode walls by a thin SiO₂-layer as used for the DB-APPJ, increases the plasma jet's atomic oxygen output by a factor of almost two.

6.3 Conclusion

Both electrodes of the APPJ were coated with a thin SiO₂-layer in order to increase the atomic oxygen output – vital for plasma treatment applications. The sticking coefficient for atomic oxygen was thus reduced by orders of magnitude. Since the SiO₂-coating constitutes a dielectric barrier, this modified setup is referred to as DB-APPJ. Measurements of electric characteristic and phase resolved optical emission intensity of the DB-APPJ's discharge show a homogeneous glow discharge identical to the discharge of the regular APPJ. TALIF-measurements, comparing the atomic oxygen ground state density in the respective effluents, proved that the atomic oxygen output efficiency of the new DB-APPJ is higher by a factor of almost two.

Chapter 7

Conclusion and Outlook

The present work contributes to a fundamental understanding of the physical and chemical processes in an atmospheric pressure plasma jet (APPJ), essential also for possible applications. The investigations focus on production and annihilation mechanisms of highly reactive atomic oxygen. – While earlier studies on the APPJ performed by other research groups only indirectly traced the atomic oxygen by means of optical emission spectroscopy and/or chemical modelling, here, the atomic oxygen density in the effluent of the planar APPJ is for the first time measured directly by two-photon absorption laser induced fluorescence spectroscopy (TALIF). Close to the jet’s nozzle an atomic oxygen density of $\sim 1 \times 10^{16} \text{ cm}^{-3}$ has been determined. Even at 10 cm distance from the nozzle, still 1 % of the initial atomic oxygen density was detected. Furthermore, optical emission spectroscopy (OES) measurements proved the occurrence of excited atomic oxygen also at 10 cm distance from the nozzle. Due to their short lifetime, it can be excluded that these excited species are generated in the plasma and subsequently transported far into the effluent. Thus, it follows that the population of these excited states can only take place outside the discharge region.

Special emphasis, therefore, was set on the identification of mechanisms of an energy transport from the discharge region into the effluent. For this purpose, results from chemical kinetics model calculations were correlated with results from optical plasma diagnostics (TALIF, optical emission-, and absorption spectroscopy). Six relevant species were investigated in the chemical model: helium, atomic and molecular oxygen, ozone, and metastable molecular oxygen $\text{O}_2(\text{a}^1\Delta_g)$ and $\text{O}_2(\text{b}^1\Sigma_g^+)$. The $\text{O}_2(\text{b}^1\Sigma_g^+)$ -density rapidly decreases close to the nozzle, as was shown also by OES-measurements. In agreement with the measurements within the jet’s effluent, the

model shows a rise in the on-axis ozone density, as well as a relatively slow decrease of the atomic oxygen density towards greater distance from the jet's nozzle. The decrease of the atomic oxygen density is slowed down due to generation of ground state atomic oxygen by reactions of ozone and long living $O_2(a^1\Delta_g)$. However, a comparison of measured and calculated oxygen radical density distributions – diffusion effects taken into account – shows that the measured atomic oxygen density close to the nozzle is higher than results from the model calculations. For an explanation of this surplus of atomic oxygen, as well as for the presence of excited atomic oxygen in the effluent, further formation mechanisms in the effluent needed to be considered.

Electrons and ions, as well as metastable helium atoms could be excluded as origin for an energy transport into the effluent, because their respective densities quickly decrease, as soon as electric excitation ceases. Energetic vacuum ultraviolet (VUV) radiation was detected by optical emission spectroscopy down to the VUV-spectral range. A spectroscopic investigation of its spacial distribution showed that (V)UV-radiation originating in the plasma reaches far into the effluent. (V)UV-radiation has sufficient energy to produce atomic oxygen outside the plasma by photodissociation of ozone or molecular oxygen. A blocking of the (V)UV-radiation at unhindered radical flux resulted in a considerably reduced atomic oxygen density in the effluent, thus confirming the (V)UV-radiation's presumed influence. According to the generation of ground state atomic oxygen, excited atomic oxygen can be generated outside the plasma by photodissociation of metastable molecular oxygen $O_2(a^1\Delta_g)$. (V)UV-radiation and the longliving metastable molecular oxygen thus yield an explanation for the energy transport into the effluent.

The present work constitutes a basis for future investigations on the atmospheric pressure plasma jet. In order to gain further insight into the processes within the APPJ's discharge region, measurements of the atomic oxygen density in the plasma are necessary. For this purpose, a so-called μ -APPJ was developed [Reuter07, Niemi07]. The dimension of this jet's discharge cross section is $1\text{ mm} \times 1\text{ mm}$. The jet is equipped with windows at the sides, allowing a wide optical access to the discharge region. This new setup of the APPJ makes two-photon laser induced fluorescence spectroscopy inside the discharge region possible. According investigations in laboratories of the Ruhr-University Bochum already showed first results.

For future investigations it is recommendable, that the newly developed μ -APPJ be modified so that the atomic oxygen density can be measured in a confined, guided

effluent. In a possible setup, the effluent region should be a continuation of the discharge region, with non-conducting walls in place of the electrodes so that no electric excitation occurs. The formation and annihilation mechanisms of the oxygen radicals in this setup could be investigated with above mentioned plasma diagnostic methods under controlled conditions.

Its characteristic properties such as its low effluent temperature and its high radical density make the APPJ exceptionally well suited for treatment of sensitive surfaces. In the present work, the influence of the jet's effluent on polymer surfaces was investigated by plasma treatment of polystyrene Petri dishes. These studies are valuable especially regarding possible applications for which a simultaneous sterilisation and functionalisation of the surface is desired. With the aid of the reactive radicals in the APPJ's effluent, Petri dishes, for example, can be prepared for biomedical applications. In a parameter study, hydrophilisation of the polystyrene surface was correlated with the oxygen radical densities in the jet's effluent. The study confirmed the following process during APPJ plasma treatment of polystyrene: As expected, atomic oxygen plays a key role in surface hydrophilisation by breaking the surface's polymer chains and thus preparing the surface for functionalisation. The actual functionalisation is reached by embedding molecular oxygen and metastable molecular oxygen. However, it became also clear that excess atomic oxygen can counteract the functionalisation of polystyrene surfaces by breaking the previously formed functional groups.

The investigations of the physical and chemical processes finally resulted in a modification of the APPJ: The production efficiency of atomic oxygen, the main reactive species in the APPJ, was improved by coating the electrode's metal surface with a thin SiO₂-layer, which reduced the recombination of atomic oxygen on the electrode walls considerably. This modified APPJ – here called DB-APPJ – was compared to the regular APPJ. It was examined, whether, due to the applied dielectric, the discharge form of the DB-APPJ differs fundamentally from that of the regular APPJ. Focus was set especially on the discharges' homogeneities. Discharges with coated electrodes can consist of so-called streamers, which only in time average appear as a homogeneous glow. Yet, phase resolved optical emission intensity measurements as well as voltage and current measurements have shown that both plasma sources produce the same homogeneous glow discharge. The plasma sheath, forming in a capacitively coupled RF-discharge, acts as dielectric. It is, therefore, irrelevant for the electrical characteristics, whether the electrodes' surface is coated with a di-

electric or consists of bare metal. Measurements of the respective atomic oxygen densities by two-photon laser induced fluorescence (TALIF) spectroscopy demonstrated that by modifying the APPJ, the atomic oxygen density was successfully increased by a factor of two.

Zusammenfassung und Ausblick

Die vorliegende Arbeit liefert einen Beitrag zum grundlegenden Verständnis der insbesondere für mögliche Anwendungen wesentlichen physikalischen und chemischen Prozesse im Atmosphärendruck Plasmajet (APPJ). Im Vordergrund der Untersuchungen stand die Frage nach den Mechanismen der Erzeugung und Vernichtung von atomarem Sauerstoff. – Während in früheren Arbeiten anderer Arbeitsgruppen der vom APPJ produzierte atomare Sauerstoff nur indirekt über optische Emissionsspektroskopie und/oder Modellierungen untersucht wurde, so konnte hier die atomare Sauerstoffdichte im Effluent des planaren APPJ erstmals direkt mittels Zweiphotonen laserinduzierter Fluoreszenzspektroskopie (TALIF) gemessen werden. Diese Messungen ergaben eine sehr hohe Sauerstoffdichte von ca. $1 \times 10^{16} \text{ cm}^{-3}$ unmittelbar an der Düse des Jets. Sogar in einer Entfernung von 10 cm ist noch 1% der anfänglichen atomaren Sauerstoffdichte vorhanden. Zusätzlich wiesen optische Emissionsspektroskopiemessungen das Vorhandensein von angeregtem atomarem Sauerstoff ebenfalls noch in ca. 10 cm Entfernung von der Düse nach. Aufgrund ihrer kurzen Lebensdauer ist ausgeschlossen, dass diese nachgewiesenen angeregten Sauerstoffatome im Plasma selbst erzeugt und bis weit in den Effluent transportiert werden. Die Erzeugung dieser Sauerstoffatome kann folglich nur außerhalb der Entladungsregion stattfinden.

Ein Hauptanliegen der Untersuchungen war es daher, die bisher nicht verstandenen Mechanismen des Energietransports aus der Entladungsregion in den Effluent zu identifizieren. Zu diesem Zweck wurde der APPJ-Effluent mit Methoden der optischen Plasmadiagnostik, sowie durch Modellierung der Reaktionskinetik untersucht. Die Ergebnisse der Modellrechnungen wurden mit den Resultaten der Plasmadiagnostiken (TALIF-, optische Emissions- und Absorptionsspektroskopie) verglichen. Im chemischen Modell wurde die Reaktionskinetik der sechs relevanten Spezies betrachtet: Helium, atomarer und molekularer Sauerstoff, Ozon sowie metastabiler molekularer Sauerstoff $\text{O}_2(a^1\Delta_g)$ und $\text{O}_2(b^1\Sigma_g^+)$. Die $\text{O}_2(b^1\Sigma_g^+)$ -Dichte nimmt, wie auch

durch OES-Messungen gezeigt werden konnte, bereits an der Düse des Jets schnell ab. In Übereinstimmung mit den Messungen im Effluent zeigt das Modell mit zunehmendem Abstand zur Düse einen Anstieg der axialen Ozondichte, sowie eine relativ langsam abfallende atomare Sauerstoffdichte. Verantwortlich für den verlangsamten Abfall ist die Erzeugung atomaren Grundzustandssauerstoffs durch Reaktionen zwischen Ozon und dem langlebigen metastabilen $\text{O}_2(\text{a}^1\Delta_g)$. Der Vergleich der gemessenen und berechneten Sauerstoffradikalendichteverläufe zeigte allerdings – auch nach Berücksichtigung von Diffusionseffekten –, dass die gemessene Sauerstoffdichte nahe der Düse höher ist, als aus den Modellrechnungen hervorgeht. Weitere Erzeugungsmechanismen im Effluent müssen demzufolge in Betracht gezogen werden, um die höhere atomare Sauerstoffdichte, sowie den angeregten atomaren Sauerstoff im Effluent zu erklären.

Elektronen, Ionen, und metastabile Heliumzustände konnten als Verantwortliche für einen Energietransport bis in den von der Düse des Jets weit entfernten Bereich des Effluent ausgeschlossen werden, da ihre Dichte zu schnell abfällt, sobald keine elektrische Anregung mehr erfolgt. Optische Emissionsspektroskopie bis in den VUV-Bereich konnte energiereiche VUV-Strahlung im Effluent nachweisen. Spektroskopische Untersuchungen der räumlichen Verteilung dieser Strahlung zeigten (V)UV-Strahlung aus dem Plasma noch in einer Entfernung von mehreren Zentimetern Abstand von der Düse. Diese (V)UV-Strahlung besitzt ausreichende Energie, um durch Photodissoziation von molekularem Sauerstoff oder Ozon atomaren Sauerstoff außerhalb des Plasmas zu erzeugen. Bestätigt werden konnte dieser Effekt durch ein Blockieren der (V)UV-Strahlung bei ungehindertem Radikalenfluss. Der Wegfall der (V)UV-Strahlung resultierte in einer reduzierten atomaren Sauerstoffdichte. Der Erzeugung von atomarem Sauerstoff im Grundzustand entsprechend kann angeregter atomarer Sauerstoff außerhalb des Plasmas durch Photodissoziation von metastabilem molekularem Sauerstoff $\text{O}_2(\text{a}^1\Delta_g)$ generiert werden. Die (V)UV-Strahlung und der langlebige metastabile molekulare Sauerstoff liefern somit eine Erklärung für den Energietransport aus dem Plasma in den Effluent.

Die vorliegende Arbeit dient auch als Grundlage für zukünftige Untersuchungen am Atmosphärendruck Plasmajet. Um das Verständnis des APPJ auf Prozesse in der Entladungsregion auszuweiten, ist es unumgänglich, die atomare Sauerstoffdichte im Plasma zu messen. Basierend auf Erkenntnissen dieser Arbeit wurde bereits ein so genannter μ -APPJ entwickelt [Reuter07, Niemi07]. Die Dimensionen des Entladungsquerschnitts sind $1\text{ mm} \times 1\text{ mm}$. Dieser Jet ist seitlich mit Fenstern versehen

und erlaubt einen weiten optischen Zugriff auf die Entladungsregion. Der neuartige Aufbau des APPJ ermöglicht es, Zweiphotonen laserinduzierte Fluoreszenzspektroskopie auch in der Entladungsregion durchzuführen. Erste Ergebnisse konnten in weiterführenden Untersuchungen in Laboren der Universität Bochum bereits gezeigt werden.

Für zukünftige Untersuchungen wäre es ferner empfehlenswert, den neu entwickelten μ -APPJ dahingehend zu modifizieren, dass die Sauerstoffdichte in einem geführten Effluent gemessen werden kann. In einem möglichen Aufbau sollte die Effluentregion dabei eine Weiterführung der Entladungsregion darstellen, wobei dort anstelle der Elektroden Quarzwände eingesetzt werden könnten, so dass keine elektrische Anregung mehr stattfindet. Die Erzeugungs- und Vernichtungsmechanismen der Sauerstoffradikale könnten dann unter kontrollierten Bedingungen mit oben genannten optischen Diagnostikmethoden untersucht werden.

Durch seine Eigenschaften, wie etwa die geringe Temperatur des Effluent und die hohe Radikalendichte, ist der hier untersuchte APPJ hervorragend geeignet, empfindliche Oberflächen zu behandeln. Um den Einfluss des Jet-Effluent auf Polymeroberflächen nachzuweisen, wurde in der vorliegenden Arbeit die Plasmabehandlung von Polystyrol-Petrischalen untersucht. Diese Untersuchungen sind insbesondere in Hinblick auf solche möglichen Anwendungen interessant, bei denen eine gleichzeitige Sterilisierung und Funktionalisierung der Oberfläche erwünscht ist. Durch die reaktiven Radikale im Effluent könnten beispielsweise Petrischalen optimal für biomedizinische Anwendungen vorbereitet werden. Im Detail untersucht wurde die Verbesserung der Benetzbarkeit der Polystyroloberfläche in Abhängigkeit zu den Radikalendichten. Die Untersuchungen zeigten den folgenden Prozess bei der APPJ-Plasmabehandlung von Polystyrol: Bei der Hydrophilisierung der Oberfläche nimmt atomarer Sauerstoff wie zu erwarten eine Schlüsselrolle ein, da er die Polymerketten aufricht und somit für die Funktionalisierung vorbereitet. Die eigentliche Funktionalisierung geschieht dann durch den Einbau von molekularem Sauerstoff und metastabilem molekularem Sauerstoff. Es zeigte sich, dass ein Überschuss an atomarem Sauerstoff für die Behandlung von Polystyroloberflächen jedoch schädlich ist, da er durch Aufbrechen der funktionalen Gruppen die erwirkte Funktionalisierung wiederum zerstört.

Die gewonnenen Erkenntnisse über die physikalischen und chemischen Abläufe konnten schließlich in eine Effizienzsteigerung der Produktion von atomarem Sauerstoff, der hauptreaktiven Spezies des APPJ, umgesetzt werden. Durch eine Beschichtung der Metalloberfläche der Elektroden mit SiO_2 konnte die Rekombination

des atomaren Sauerstoffs an den Elektrodenwänden erheblich reduziert werden. Ob sich die Entladungsform dieses hier als DB-APPJ bezeichneten modifizierten Jets durch das aufgebrachte Dielektrikum grundlegend, insbesondere aber in ihrer Homogenität, von der des regulären APPJ unterscheidet, wurde untersucht. Bei der Entladung mit beschichteten Elektroden sind so genannte Streamer denkbar, die im zeitlichen Mittel als homogene Glimmentladung erscheinen können. Phasenaufgelöste optische Emissionsmessungen, optische Emissionsspektroskopie, sowie Strom- und Spannungssignale und -kennlinien zeigten jedoch, dass beide Entladungen die gleiche homogene Entladungsform besitzen. Die Plasmaschicht, die sich in kapazitiv gekoppelten RF-Glimmentladungen entwickelt, wirkt wie ein Dielektrikum, sodass es für die elektrischen Eigenschaften der Plasmaquelle unerheblich ist, ob die Elektroden mit einem Dielektrikum beschichtet sind, oder ob es sich um bloße Metallelektroden handelt. Wie vergleichende Messungen der atomaren Sauerstoffdichten mittels Zweiphotonen laserinduzierte Fluoreszenzspektroskopie (TALIF) zeigten, wurde durch diese im abschließenden Teil der Arbeit beschriebene Modifikation des APPJ die produzierte atomare Sauerstoffdichte um den Faktor Zwei erhöht.

Bibliography

- [Adamson90] A. Adamson: *Physical Chemistry of Surfaces*, John Wiley & Sons Inc., New York (1990).
- [Amirfazli98] A. Amirfazli, D. Chatain, and A. W. Neumann: *Drop size dependence of contact angles for liquid tin on silica surface: line tension and its correlation with solid-liquid interfacial tension*, *Colloids Surfaces A: Physicochem. Eng. Aspects* **142**(2-3) (1998) 183–188.
- [Amorim00] J. Amorim, G. Baravian, and J. Jolly: *Laser-induced resonance fluorescence as a diagnostic technique in non-thermal equilibrium plasmas*, *J. Phys. D: Appl. Phys.* **33**(9) (2000) R51–R65.
- [Armstrong67] B. H. Armstrong: *Spectrum Line Profiles: The Voigt Function*, *J. Quant. Spectrosc. Radiat. Transfer* **7** (1967) 61–88.
- [Baars-Hibbe05] L. Baars-Hibbe, P. Sichler, C. Schrader, K.-H. Gericke, and S. Büttgenbach: *Micro-Structured Electrode Arrays: Characterization of High Frequency Discharges at Atmospheric Pressure*, *Plasma Process. Polym.* **2**(3) (2005) 174–182.
- [Babayan01a] S. E. Babayan, G. Ding, and R. F. Hicks: *Determination of the Nitrogen Atom Density in the Afterglow of a Nitrogen and Helium, Nonequilibrium, Atmospheric Pressure Plasma*, *Plasma Chem. Plasma Process.* **21**(4) (2001) 505–521.
- [Babayan01b] S. E. Babayan, J. Y. Jeong, A. Schütze, V. J. Tu, M. Moravej, G. S. Selwyn, and R. F. Hicks: *Deposition of silicon dioxide films with a non-equilibrium atmospheric-pressure plasma jet*, *Plasma Sources Sci. Technol.* **10**(4) (2001) 573–578.
- [Balcon07] N. Balcon, A. Aanesland, and R. Boswell: *Pulsed RF discharges, glow and filamentary mode at atmospheric pressure in argon*, *Plasma Sources Sci. Technol.* **16**(2) (2007) 217–225.
- [Becker04] K. H. Becker, R. J. Barker, K. H. Schoenbach, and U. Kogelschatz: *Non-Equilibrium Air Plasmas at Atmospheric Pressure (Series in Plasma Physics)*, Institute of Physics Publishing, Bristol/Philadelphia (2004).

- [Berg93] J. C. Berg: *Wettability*, Marcel Dekker Inc., New York (1993).
- [Bhoj05] A. N. Bhoj and M. J. Kushner: *Plasma-polymer interactions in a dielectric barrier discharge*, IEEE Trans. Plasma Sci. **33**(2) (2005) 250–251.
- [Bicchi97] P. Bicchi, C. Marinelli, E. Mariotti, M. Meucci, and L. Moi: *Energy-pooling ionization and electron-ion recombination measurements in indium*, J. Phys. B: At., Mol. Opt. Phys. **30** (1997) 473–482.
- [Biondi76] M. Biondi: *Recombination*, in: G. Bekefi (Ed.) *Principles of Laser Plasmas*, chap. 4, John Wiley & Sons Inc., New York (1976), 125–157.
- [BMBF07] BMBF: *PlasmaNews*, Newsletter, VDI-Technologiezentrum, Düsseldorf (2007).
- [Boffard04] J. B. Boffard, C. C. Lin, and C. A. DeJoseph Jr: *Application of excitation cross sections to optical plasma diagnostics*, J. Phys. D: Appl. Phys. **37**(12) (2004) R143–R161.
- [Bogaerts02] A. Bogaerts, E. Neyts, R. Gijbels, and J. van der Mullen: *Gas discharge plasmas and their applications*, Spectrochimica Acta Part B **57** (2002) 609–658.
- [Bonin84] K. D. Bonin and T. J. McIlrath: *Two-photon electric-dipole selection rules*, J. Opt. Soc. Am. B: Opt. Phys. **1**(1) (1984) 52–55.
- [Boudam06] M. K. Boudam, M. Moisan, B. Saoudi, C. Popovici, N. Gherardi, and F. Massines: *Bacterial spore inactivation by atmospheric-pressure plasmas in the presence or absence of UV photons as obtained with the same gas mixture*, J. Phys. D: Appl. Phys. **39**(16) (2006) 3494–3507.
- [Brackmann94] U. Brackmann: *Lamdbachrome Laser Dyes*, Lambda Physik GmbH, Göttingen, 2nd edn. (1994).
- [Burle Industries Inc.07] Burle Industries Inc.: *Burle C31034A Manual*, Lancaster, PA (2007).
- [Cardoso06] R. P. Cardoso, T. Belmonte, G. Henrion, and N. Sadeghi: *Influence of trace oxygen on He($2\ ^3S$) density in a He-O₂ microwave discharge at atmospheric pressure: behaviour of the time afterglow*, J. Phys. D: Appl. Phys. **39**(19) (2006) 4178–4185.
- [Cartry99] G. Cartry, L. Magne, and G. Cernogora: *Experimental study and modelling of a low-pressure N₂-O₂ time afterglow*, J. Phys. D: Appl. Phys. **32**(15) (1999) 1894–1907.

- [Chen74] F. F. Chen: *Introduction to Plasma Physics*, Plenum Press, New York (1974).
- [Choi99] S.-C. Choi, W.-K. Choi, H.-J. Jung, J.-G. Park, B.-C. Chung, Y.-S. Yoo, and S.-K. Koh: *Relation between hydrophilicity and cell culturing on polystyrene Petri dish modified by ion-assisted reaction*, J. Appl. Polym. Sci. **73**(1) (1999) 41–46.
- [Clyne79] M. A. Clyne and W. S. Nip: *Generation and Measurement of Atom and Radical Concentrations in Flow Systems*, in: D. Setser (Ed.) *Reactive Intermediates in the Gas Phase*, chap. 1, Academic Press, New York (1979), 1–50.
- [Cole06] A. S. Cole and K. A. Boering: *Mass-dependent and non-mass-dependent isotope effects in ozone photolysis: Resolving theory and experiments*, J. Chem. Phys. **125**(18) (2006) 184301/1–184301/14.
- [Criegee75] R. Criegee: *Mechanism of Ozonolysis*, Angew. Chem. Internat. Edit. **14**(11) (1975) 745–752.
- [Demtröder04] W. Demtröder: *Laserspektroskopie – Grundlagen und Techniken*, vol. 4, Springer-Verlag, Berlin/Heidelberg/New York (2004).
- [Dhayal06] M. Dhayal, M. R. Alexander, and J. W. Bradley: *The surface chemistry resulting from low-pressure plasma treatment of polystyrene: The effect of residual vessel bound oxygen*, Appl. Surf. Sci. **252**(22) (2006) 7957–7963.
- [Diamy05] A.-M. Diamy, J.-C. Legrand, V. V. Rybkin, and S. A. Smirnov: *Experimental Study and Modelling of Formation and Decay of Active Species in an Oxygen Discharge*, Contrib. Plasma Phys. **45**(1) (2005) 5–21.
- [Dilecce00] G. Dilecce, M. Vigliotti, and S. De Benedictis: *A TALIF calibration method for quantitative oxygen atom density measurement in plasma jets*, J. Phys. D: Appl. Phys. **33** (2000) L53–L56.
- [Döbele95] H. F. Döbele: *Methoden der optischen Plasmadiagnostik für technische Plasmen*, in: H. Frey (Ed.) *Vakuumbeschichtung Band 1, Plasmaphysik - Plasmadiagnostik - Analytik*, chap. 2, VDI-Verlag, Düsseldorf (1995), 173–231.
- [Döbele05] H. F. Döbele, T. Mosbach, K. Niemi, and V. Schulz-von der Gathen: *Laser-induced fluorescence measurements of absolute atomic densities: concepts and limitations*, Plasma Sources Sci. Technol. **14**(2) (2005) 31–41.

- [Dockery07] K. P. Dockery, K. D. Sieber, F. A. Knapp, and T. E. Wilson: *Surface acid chemistry associated with dielectric barrier discharge (DBD) treatment of polyethylene*, Plasma Sources Sci. Technol. **16**(1) (2007) 42–49.
- [Drelich97] J. Drelich: *The Effect of Drop (Bubble) Size on Contact Angle at Solid Surfaces*, J. Adhes. **63**(1-3) (1997) 31–51.
- [Ehrich88] H. Ehrich: *The anodic vacuum arc. I. Basic construction and phenomenology*, J. Vac. Sci. Technol., A **6**(1) (1988) 134–138.
- [Engel33] A. von Engel, R. Seeliger, and M. Steenbeck: *Über die Glimmentladung bei hohen Drucken*, Zeitschrift für Physik A Hadrons and Nuclei **85** (1933) 145–160.
- [Faist76] M. B. Faist and R. B. Bernstein: *Computational study of elastic and electronically inelastic scattering of Br by ground state I atoms: Role of potential curve crossing*, J. Chem. Phys. **64**(7) (1976) 2971–2984.
- [Fang03] Q. Fang, J.-Y. Zhang, and I. W. Boyd: *Rapid oxidation of silicon using 126 nm excimer radiation at low pressure*, Appl. Surf. Sci. **208-209** (2003) 369–373.
- [Fantz06] U. Fantz: *Basics of Plasma Spectroscopy*, Plasma Sources Sci. Technol. **15**(4) (2006) 137–147.
- [Flusberg76] A. Flusberg, T. Mossberg, and S. R. Hartmann: *Hyperfine structure, isotopic level shifts, and pressure self-broadening of the 7^2P states of natural thallium by Doppler-free two-photon absorption*, Phys. Rev. A **14**(6) (1976) 2146–2158.
- [Fozza99] A. C. Fozza, J. E. Klemberg-Sapieha, and M. R. Wertheimer: *Vacuum Ultraviolet Irradiation of Polymers*, Plasmas Polym. **4**(2) (1999) 183–206.
- [Francis56] G. Francis: *The Glow Discharge at Low Pressure*, in: S. Flügge (Ed.) Encyclopedia of Physics: Gas Discharges II, vol. XXII, Springer-Verlag, Berlin/Heidelberg/N.Y. (1956), 53–208.
- [Francis97] A. Francis, U. Czarnetzki, H. F. Döbele, and N. Sadeghi: *Quenching of the 750.4 nm argon actinometry line by H_2 and several hydrocarbon molecules*, Appl. Phys. Lett. **71**(26) (1997) 3796–3798.
- [Francis03] A. Francis: *Spektroskopische Untersuchungen zur Struktur und Dynamik der Radikale in einer reaktiven Fluor-Kohlenstoff-Entladung*, Dissertation, Universität Duisburg-Essen (2003).

- [Gejo06] J. L. Gejo, N. Manoj, S. Sumalekshmy, H. Glieman, T. Schimmel, M. Woerner, and A. M. Braun: *Vacuum-ultraviolet photochemically initiated modification of polystyrene surfaces: morphological changes and mechanistic investigations*, Photochem. Photobiol. Sci. **5**(10) (2006) 948–954.
- [Gellert91] B. Gellert and U. Kogelschatz: *Generation of excimer emission in dielectric barrier discharges*, Appl. Phys. B **52**(1) (1991) 14–21.
- [Gencom77] Gencom: EMI Gencom G-26 H315 Datasheet, EMI Gencom Inc., New York (1977).
- [Gennes85] P. G. de Gennes: *Wetting: statics and dynamics*, Rev. Mod. Phys. **57**(3) (1985) 827–863.
- [Gericke02] K. H. Gericke, C. Geßner, and P. Scheffler: *Microstructure electrodes as a means of creating uniform discharges at atmospheric pressure*, Vacuum **65**(3-4) (2002) 291–297.
- [Goehlich98] A. Goehlich, T. Kawetzki, and H. F. Döbele: *On absolute calibration with xenon of laser diagnostic methods based on two-photon absorption*, J. Chem. Phys. **108**(22) (1998) 9362–9370.
- [Goeppert-Mayer31] M. Goeppert-Mayer: *Über Elementarakte mit zwei Quantensprüngen*, Ann. Physik **401**(3) (1931) 273–294.
- [Goldston95] R. J. Goldston and P. H. Rutherford: *Introduction to Plasma Physics*, Institute of Physics Publishing, Bristol/Philadelphia (1995).
- [Griem97] H. R. Griem: *Principles of Plasma Spectroscopy*, Cambridge University Press, Cambridge (1997).
- [Grotrian15] W. Grotrian: *Der Gleichstrom-Lichtbogen großer Bogenlänge*, Ann. Physik **352**(10) (1915) 141–197.
- [Hampson75] R. F. Hampson and D. Garvin: *Chemical kinetic and photochemical data for modelling atmospheric chemistry*, Special publication, Natl. Bur. Stand., Washington D.C. (1975).
- [Hargis et al.94] P. J. Hargis et al.: *The Gaseous Electronics Conference Radiofrequency Reference Cell: A Defined Parallel-Plate Radiofrequency System for Experimental and Theoretical-Studies of Plasma-Processing Discharges*, Rev. Sci. Instrum. **65**(1) (1994) 140–154.
- [Heimann04] B. Heimann, S. Reuter, F. Deuerler, and V. Buck: *Qualitätssicherung durch Schichtdickenmessung von Diamant- und diamantartigen Schichten*, Galvanotechnik **95**(4) (2004) 994–1001.

- [Hicks99] R. F. Hicks and G. S. Selwyn: *Atmospheric-Pressure Plasma Cleaning of Contaminated Surfaces*, Project report, U.S. Department of Energy, Washington D.C. (1999).
- [Holstein47] T. Holstein: *Imprisonment of Resonance Radiation in Gases*, Phys. Rev. **72**(12) (1947) 1212–1233.
- [Holstein51] T. Holstein: *Imprisonment of Resonance Radiation in Gases. II*, Phys. Rev. **83**(6) (1951) 1159–1168.
- [Hozumi04] A. Hozumi, N. Shirahata, Y. Nakanishi, S. Asakura, and A. Fuwa: *Wettability control of a polymer surface through 126 nm vacuum ultraviolet light irradiation*, J. Vac. Sci. Technol., A **22**(4) (2004) 1309–1314.
- [Huddelstone65] R. H. Huddelstone and S. L. Leonard: *Plasma Diagnostic Techniques*, Academic Press, New York (1965).
- [Hughey82] B. J. Hughey and D. A. Santavicca: *A Comparison of Techniques for Reconstructing Axisymmetric Reacting Flow Fields from Absorption Measurements*, Combust. Sci. Technol. **29**(3-6) (1982) 167–190.
- [Hutchinson87] I. H. Hutchinson: *Principles of Plasma Diagnostics*, Cambridge University Press, Cambridge (1987).
- [Jeong98] J. Y. Jeong, S. E. Babayan, V. J. Tu, J. Park, I. Henins, R. F. Hicks, and G. S. Selwyn: *Etching materials with an atmospheric-pressure plasma jet*, Plasma Sources Sci. Technol. **7**(3) (1998) 282–285.
- [Jeong00] J. Y. Jeong, J. Park, I. Henins, S. E. Babayan, V. J. Tu, G. S. Selwyn, G. Ding, and R. F. Hicks: *Reaction Chemistry in the Afterglow of an Oxygen-Helium Atmospheric-Pressure Plasma*, J. Phys. Chem. A **104** (2000) 8027–8032.
- [Joubert89] O. Joubert, J. Pelletier, and Y. Arnal: *The etching of polymers in oxygen-based plasmas: A parametric study*, J. Appl. Phys. **65**(12) (1989) 5096–5100.
- [Kaiser61] W. Kaiser and C. G. B. Garrett: *Two-Photon Excitation in CaF_2 : Eu^{2+}* , Phys. Rev. Lett. **7**(6) (1961) 229–231.
- [Kanazawa88] S. Kanazawa, M. Kogoma, T. Moriwaki, and S. Okazaki: *Stable glow plasma at atmospheric pressure*, J. Phys. D: Appl. Phys. **21**(5) (1988) 838–840.
- [Kaufman58] F. Kaufman and J. R. Kelso: *Vibrationally Excited Ground-State Nitrogen in Active Nitrogen*, J. Chem. Phys. **28**(3) (1958) 510–511.

- [Kieft04] I. E. Kieft, E. P. Van der Laan, and E. Stoffels: *Electrical and optical characterization of the plasma needle*, New Journal of Physics **6** (2004) 149/1–149/14.
- [Kiehlbauch03] M. W. Kiehlbauch and D. B. Graves: *Inductively coupled plasmas in oxygen: Modeling and experiment*, J. Vac. Sci. Technol., A **21**(3) (2003) 660–670.
- [Knake07] N. Knake: Bestimmung der atomaren Sauerstoff-Konzentration in einem Plasmajet zur Oberflächenbehandlung, Diplomarbeit, Universität Duisburg-Essen (2007).
- [Kogelschatz90] U. Kogelschatz: *Silent discharges for the generation of ultraviolet and vacuum ultraviolet excimer radiation*, Pure and Appl. Chem. **62** (1990) 1667–1674.
- [Kogelschatz04] U. Kogelschatz: *Atmospheric-pressure plasma technology*, Plasma Phys. Controlled Fusion **46** (2004) B63–B75.
- [Koinuma92] H. Koinuma, H. Ohkubo, T. Hashimoto, K. Inomata, T. Shiraishi, A. Miyanaga, and S. Hayashi: *Development and application of a microbeam plasma generator*, Appl. Phys. Lett. **60**(7) (1992) 816–817.
- [Kuceroval06] Z. Kuceroval, L. Zajickova, O. Jasek, M. Elias, R. Ficek, R. Vrba, F. Matejka, J. Matejkova, and J. Bursik: *Carbon nanotubes synthesized by plasma enhanced CVD: preparation for measurements of their electrical properties*, Czech. J. Phys. **56**(2) (2006) B1244–B1249.
- [Kurunczi01] P. Kurunczi, J. Lopez, H. Shah, and K. Becker: *Excimer formation in high-pressure microhollow cathode discharge plasmas in helium initiated by low-energy electron collisions*, Int. J. Mass Spectrom. **205**(1-3) (2001) 277–283.
- [Laimer05] J. Laimer, S. Haslinger, W. Meissl, J. Hell, and H. Stori: *Investigation of an atmospheric pressure radio-frequency capacitive plasma jet*, Vacuum **79**(3-4) (2005) 209–214.
- [Laroussi05] M. Laroussi and X. Lu: *Room-temperature atmospheric pressure plasma plume for biomedical applications*, Appl. Phys. Lett. **87**(11) 113902/1–113902/3.
- [Lee77] L. C. Lee, T. G. Slanger, G. Black, and R. L. Sharpless: *Quantum Yields for the Production of $O(^1D)$ from Photodissociation of O_2 at 1160–1770 Å*, J. Chem. Phys. **67**(12) (1977) 5602–5606.
- [Lemmon05] E. W. Lemmon, M. McLinden, and D. Friend: *Thermophysical Properties of Fluid Systems*, in: P. Linstrom and W. Mallard

- (Eds.) NIST Chemistry WebBook, NIST Standard Reference Database No 69, National Institute of Standards and Technology, Gaithersburg MD (2005), <http://webbook.nist.gov>.
- [Levitskii57] M. S. Levitskii: *An Investigation of the Breakdown Potential of a High Frequency Plasma in the Frequency and Pressure Transition Regions*, Sov. Phys. Tech. Phys. **2** (1957) 887–893.
- [Lide00] D. R. Lide: CRC Handbook of Chemistry and Physics, CRC Press - USA, Boca Raton, FL, 81st edn. (2000).
- [Lieberman94] M. A. Lieberman and A. J. Lichtenberg: Principles of plasma discharges and materials processing, John Wiley & Sons Inc., New York (1994).
- [Lochte-Holtgreven68] W. Lochte-Holtgreven: Plasma Diagnostics, North Holland Publishing Company, Amsterdam (1968).
- [Loudon83] R. Loudon: The quantum theory of light, Clarendon Press, Oxford, 2nd edn. (1983).
- [Luque98] J. Luque, W. Juchmann, E. A. Brinkman, and J. B. Jeffries: *Excited state density distributions of H, C, C₂, and CH by spatially resolved optical emission in a diamond depositing dc-arcjet reactor*, J. Vac. Sci. Technol., A **16**(2) (1998) 397–408.
- [Macko04] P. Macko, P. Veis, and G. Cernogora: *Study of oxygen atom recombination on a Pyrex surface at different wall temperatures by means of time-resolved actinometry in a double pulse discharge technique*, Plasma Sources Sci. Technol. **13**(2) (2004) 251–262.
- [Macrossan03] M. N. Macrossan and C. R. Lilley: *Viscosity of argon at temperatures > 2000 K from measured shock thickness*, Physics of Fluids **15**(11) (2003) 3452–3457.
- [Magne93] L. Magne, H. Coitout, G. Cernogora, and G. Gousset: *Atomic oxygen recombination at the wall in a time afterglow*, J. Phys. III France **3** (1993) 1871–1889.
- [Marx78] B. R. Marx, J. Simons, and L. Allen: *The effect of laser linewidth on two-photon absorption rates*, J. Phys. B: At., Mol. Opt. Phys. **11**(8) (1978) L273–L277.
- [Massines98a] F. Massines and G. Gouda: *A comparison of polypropylene-surface treatment by filamentary, homogeneous and glow discharges in helium at atmospheric pressure*, J. Phys. D: Appl. Phys. **31**(24) (1998) 3411–3420.

- [Massines98b] F. Massines, A. Rabehi, P. Decomps, R. B. Gadri, P. Segur, and C. Mayoux: *Experimental and theoretical study of a glow discharge at atmospheric pressure controlled by dielectric barrier*, J. Appl. Phys. **83**(6) (1998) 2950–2957.
- [McWhirter65] R. W. P. McWhirter: *Spectral Intensities*, in: R. H. Huddelstone and S. L. Leonard (Eds.) Plasma Diagnostic Techniques, chap. 5, Academic Press, New York (1965), 201–264.
- [Mitchell71] A. C. G. Mitchell and M. W. Zemansky: Resonance Radiation and Excited Atoms, Cambridge University Press, Cambridge (1971).
- [Müller97] M. Müller: Einfluß von Beimengungen molekularer Gase auf die Elektronenenergieverteilungsfunktion in einem Argon-RF-Plasma, Diplomarbeit, Universität GH Essen (1997).
- [Moon06] S. Y. Moon, J. K. Rhee, D. B. Kim, and W. Choe: α , γ , and normal, abnormal glow discharge modes in radio-frequency capacitively coupled discharges at atmospheric pressure, Phys. Plasmas **13**(3) (2006) 033502/1–033502/6.
- [Moore75] C. E. Moore: Selected Tables of Atomic Spectra, vol. 3, Sect. 7, Natl. Bur. Stand. pub. NSRDS-NBS, Washington D.C. (1975).
- [Moreau07] E. Moreau: *Airflow control by non-thermal plasma actuators*, J. Phys. D: Appl. Phys. **40**(3) (2007) 605–636.
- [Mozeti00] M. Mozeti and A. Zalar: *Recombination of neutral oxygen atoms on stainless steel surface*, Appl. Surf. Sci. **158**(3-4) (2000) 263–267.
- [Nee97] J. B. Nee and P. C. Lee: *Detection of $O(^1D)$ Produced in the Photodissociation of O_2 in the Schumann-Runge Continuum*, J. Phys. Chem. A **101**(36) (1997) 6653–6657.
- [Nersisyan04] G. Nersisyan, T. Morrow, and W. G. Graham: *Measurements of helium metastable density in an atmospheric pressure glow discharge*, Appl. Phys. Lett. **85**(9) (2004) 1487–1489.
- [Niemi03a] K. Niemi: Nachweis leichter Atome in reaktiven Plasmen mittels Zweiphotonen laserinduzierter Fluoreszenzspektroskopie unter besonderer Berücksichtigung der Absolutkalibrierung, Dissertation, Universität Duisburg-Essen (2003).
- [Niemi03b] K. Niemi, T. Mosbach, and H. F. Döbele: *Is the flow tube reactor with NO_2 titration a reliable absolute source for atomic hydrogen?*, Chem. Phys. Lett. **367**(5-6) (2003) 549–555.

- [Niemi04] K. Niemi, S. Reuter, V. Schulz-von der Gathen, and H. F. Döbele: *Quantitative atomic oxygen density measurements in an atmospheric pressure plasma jet by two-photon laser-induced fluorescence*, in: Proceedings of the 17th European Conference on Atomic and Molecular Physics of Ionized Gases (ES-CAMPIG), Constanta (2004), 157–158.
- [Niemi05] K. Niemi, V. Schulz-von der Gathen, and H. F. Döbele: *Absolute Atomic Oxygen Density Measurements by Two-Photon Absorption Laser-Induced Fluorescence Spectroscopy in an Rf-Excited Atmospheric Pressure Plasma Jet*, Plasma Sources Sci. Technol. **14**(2) (2005) 375–386.
- [Niemi07] K. Niemi, S. Reuter, L. Schaper, N. Knake, V. Schulz-von der Gathen, and T. Gans: *Diagnostics on an atmospheric pressure plasma jet*, J. Phys.: Conf. Ser. **71** (2007) 012012/1–012012/9.
- [Norlen73] G. Norlen: *Wavelengths and Energy Levels of Ar I and Ar II based on New Interferometric Measurements in the Region 3400-9800 Å*, Phys. Scr. **8**(6) (1973) 249–268.
- [Normand95] F. Normand, A. Granier, P. Leprince, J. Marec, M. K. Shi, and F. Clouet: *Polymer treatment in the flowing afterglow of an oxygen microwave discharge: Active species profile concentrations and kinetics of the functionalization*, Plasma Chem. Plasma Process. **15**(2) (1995) 173–198.
- [Norström79] H. Norström: *Experimental and design information for calculating impedance matching networks for use in rf sputtering and plasma chemistry*, Vacuum **29**(10) (1979) 381–453.
- [Ogryzlo78] E. A. Ogryzlo: *The Nature of Singlet Oxygen*, in: R. Ranby and J. Rabek (Eds.) Singlet Oxygen Reactions with Organic Compounds and Polymers, John Wiley & Sons Inc., New York (1978), 4–12.
- [Pagnon95] D. Pagnon, J. Amorim, J. Nahorny, M. Touzeau, and M. Vialle: *On the use of actinometry to measure the dissociation in O₂ DC glow discharges: determination of the wall recombination probability*, J. Phys. D: Appl. Phys. **28**(9) (1995) 1856–1868.
- [Parisse96] C. Parisse, J. Brion, and J. Malicet: *UV absorption spectrum of ozone: structure analysis and study of the isotope effect in the Hartley system*, Chem. Phys. Lett. **248**(1-2) (1996) 31–36.
- [Park98] J. Park, H. W. Herrmann, I. Henins, and G. S. Selwyn: *Atmospheric pressure plasma jet applications*, in: Plasma Science, 25th Anniversary IEEE Conference Record - Abstracts (1998), 290.

- [Park00] J. Park, I. Henins, H. W. Herrmann, G. S. Selwyn, J. Y. Jeong, R. F. Hicks, D. Shim, and C. S. Chang: *An atmospheric pressure plasma source*, Appl. Phys. Lett. **76**(3) (2000) 288–290.
- [Park01] J. Park, I. Henins, H. W. Herrmann, and G. S. Selwyn: *Gas breakdown in an atmospheric pressure radio-frequency capacitive plasma source*, J. Appl. Phys. **89**(1) (2001) 15–19.
- [Parker00] D. H. Parker: *Laser Photochemistry of Molecular Oxygen*, Acc. Chem. Res. **33**(8) (2000) 563–571.
- [Paulussen05] S. Paulussen, R. Rego, O. Goossens, D. Vangeneugden, and K. Rose: *Physical and chemical properties of hybrid barrier coatings obtained in an atmospheric pressure dielectric barrier discharge*, J. Phys. D: Appl. Phys. **38**(4) (2005) 568–575.
- [Payne81] M. G. Payne, C. H. Chen, G. S. Hurst, and G. W. Foltz: *Applications of resonance ionization spectroscopy in atomic and molecular physics*, Adv. At. Mol. Phys. **17** (1981) 229–274.
- [Peeling03] J. Peeling and D. T. Clark: *Surface ozonation and photooxidation of polyethylene film*, J. Polym. Sci. Polym. Chem. Ed. **21**(7) (2003) 2047–2055.
- [Raiser06] J. Raiser and M. Zenker: *Argon plasma coagulation for open surgical and endoscopic applications: state of the art*, J. Phys. D: Appl. Phys. **39**(16) (2006) 3520–3523.
- [Raizer95] Y. P. Raizer, M. N. Shneider, and N. A. Yatsenko: *Radio Frequency Capacitive Discharges*, CRC Press - UK, London (1995).
- [Raizer01] Y. P. Raizer: *Gas Discharge Physics*, Springer-Verlag, Berlin/Heidelberg/New York (2001).
- [Rehn03] P. Rehn, A. Wolkenhauer, M. Bente, S. Förster, and W. Viöl: *Wood surface modification in dielectric barrier discharges at atmospheric pressure*, Surf. Coat. Technol. **174–175** (2003) 515–518.
- [Reuter03] S. Reuter: *Spektroskopie an harten Kohlenstoffschichten*, Diplomarbeit, Universität Essen (2003).
- [Reuter05] S. Reuter, K. Niemi, V. Schulz-von der Gathen, and H. F. Döbele: *The Atmospheric Pressure Plasma Jet (APPJ): Characteristics and Diagnostics*, in: Frühjahrstagung der DPG, Berlin (2005).
- [Reuter06] S. Reuter, K. Niemi, V. Schulz-von der Gathen, and H. F. Döbele: *Absolute Atomic Oxygen Density Measurements by Two-Photon Laserinduced Fluorescence (TALIF) Spectroscopy in the*

- Effluent of an Atmospheric Pressure Plasma Jet*, in: 59th Annual Gaseous Electronics Conference, Columbus, OH (2006), 21.
- [Reuter07] S. Reuter, K. Niemi, V. Schulz-von der Gathen, and H. F. Döbele: *The Atmospheric Pressure Plasma Jet as an Atomic Oxygen Source for Polymer Treatment*, in: Proc. 3rd CAPPSA, Ghent (2007).
- [Rhodes74] C. K. Rhodes: *Review of ultraviolet laser physics*, IEEE J. Quantum Electron. **QE-10** (1974) 153–174.
- [Rombola06] G. Rombola, F. Parisi, C. Pavan, and D. Dapra : *On-line Atmospheric Pressure Plasma (APP) treatment of polypropylene fabrics*, Czech. J. Phys. **56**(0) (2006) B1021–B1028.
- [Roth95] J. R. Roth, P. P.-Y. Tsai, C. Liu, M. Laroussi, and P. D. Spence: *One Atmosphere, Uniform Glow Discharge Plasma*, United States Patent No 5414324, Knoxville, TN (1995).
- [Roth01a] J. R. Roth: *Industrial Plasma Engineering, Vol II - Applications to Non-Thermal Plasma Processing*, Institute of Physics Publishing, Bristol/Philadelphia (2001).
- [Roth01b] J. R. Roth, Z. Chen, D. M. Sherman, F. Karakaya, P. P.-Y. Tsai, K. Kelly-Wintenberg, and T. C. Montie: *Increasing the Surface Energy and Sterilization of Nonwoven Fabrics by Exposure to a One Atmosphere Uniform Glow Discharge Plasma (OAUGDP)*, Int. Nonwovens J. **10**(3) (2001) 34–47.
- [Roth04] J. R. Roth, R. C. M. Madhan, M. Yadav, J. R. Stephen, and P. Wilkinson: *Flow Field Measurements of Paraelectric, Peristaltic, and Combined Plasma Actuators based on the One Atmosphere Uniform Glow Discharge Plasma (OAUGDP)*, in: Proc. 42nd AIAA Aerospace Sciences Meeting and Exhibit, Reno, NV (2004).
- [Roth05] J. R. Roth, J. Rahel, X. Dai, and D. M. Sherman: *The physics and phenomenology of One Atmosphere Uniform Glow Discharge Plasma (OAUGDP) reactors for surface treatment applications*, J. Phys. D: Appl. Phys. **38**(4) (2005) 555–567.
- [Roth07] J. R. Roth, S. Nourgostar, and T. A. Bonds: *The One Atmosphere Uniform Glow Discharge Plasma (OAUGDP) - A Platform Technology for the 21st Century*, IEEE Trans. Plasma Sci. **35**(2) (2007) 233–250.
- [Rott90] N. Rott: *Note on the History of the Reynolds Number*, Annu. Rev. Fluid Mech. **22** (1990) 1–12.

- [Sabadil80] H. Sabadil, P. Bachmann, and H. Kastelewicz: *Reaktionskinetik der Ozonbildung in der Sauerstoffglimmentladung*, Beitr. Plasmaphys. **20**(4) (1980) 283–295.
- [Sansonettti01] C. J. Sansonettti and J. Reader: *Spectrum and Energy Levels of Singly-Ionized Mercury (Hg II)*, Phys. Scr. **63**(3) (2001) 219–242.
- [Sarra-Bournet06] C. Sarra-Bournet, S. Turgeon, D. Mantovani, and G. Laroche: *A study of atmospheric pressure plasma discharges for surface functionalization of PTFE used in biomedical applications*, J. Phys. D: Appl. Phys. **39**(16) (2006) 3461–3469.
- [Saxon86] R. P. Saxon and J. Eichler: *Theoretical calculation of two-photon absorption cross sections in atomic oxygen*, Phys. Rev. A **34**(1) (1986) 199–206.
- [Schaper07] L. Schaper: Charakterisierung eines Plasmajets zur Oberflächenbehandlung mit Hilfe von optischer Emissionsspektroskopie, Diplomarbeit, Universität Duisburg-Essen (2007).
- [Schoenbach97] K. H. Schoenbach, A. El-Habachi, W. Shi, and M. Ciocca: *High-pressure hollow cathode discharges*, Plasma Sources Sci. Technol. **6**(4) (1997) 468–477.
- [Schrader92] M. E. Schrader and G. I. Loeb: *Modern Approaches to Wettability - Theory and Applications*, Plenum Press, New York (1992).
- [Schütze98] A. Schütze, J. Y. Jeong, S. E. Babayan, J. Park, G. S. Selwyn, and R. F. Hicks: *The Atmospheric-Pressure Plasma Jet: A Review and Comparison to Other Plasma Sources*, IEEE Trans. Plasma Sci. **26**(6) (1998) 1685–1694.
- [Schulz-von der Gathen05] V. Schulz-von der Gathen, S. Reuter, K. Niemi, and H. F. Döbele: *A ‘cold’ atmospheric pressure plasma jet for treatment of sensitive surfaces with biomedical relevance*, in: 8th Symposium on Biomaterials and Biomechanics, Essen (2005).
- [Schwabl05] F. Schwabl: *Quantenmechanik*, Springer-Verlag, Berlin/Heidelberg/New York, 6th corrected reprint edn. (2005).
- [Selwyn99] G. S. Selwyn: *Atmospheric-pressure plasma jet*, United States Patent No 5961772, Los Angeles, CA (1999).
- [Shi03] J. J. Shi, X. T. Deng, R. Hall, J. D. Punnett, and M. G. Kong: *Three modes in a radio frequency atmospheric pressure glow discharge*, J. Appl. Phys. **94**(10) (2003) 6303–6310.

- [Shi05] J. J. Shi and M. G. Kong: *Expansion of the plasma stability range in radio-frequency atmospheric-pressure glow discharges*, Appl. Phys. Lett. **87**(20) (2005) 201501/1–201501/3.
- [Singh00] H. Singh, J. W. Coburn, and D. B. Graves: *Recombination coefficients of O and N radicals on stainless steel*, J. Appl. Phys. **88**(6) (2000) 3748–3755.
- [Sira05] M. Sira, D. Trunec, P. Stahel, V. Burscaronikova, Z. Navratil, and J. Bursik: *Surface modification of polyethylene and polypropylene in atmospheric pressure glow discharge*, J. Phys. D: Appl. Phys. **38**(4) (2005) 621–627.
- [Sladek03] R. E. J. Sladek, E. Stoffels, R. Walraven, P. J. A. Tielbeek, and R. A. Koolhoven: *Investigation of possibilities of plasma treatment for dental caries*, in: Digest of Technical Papers: 14th IEEE International Pulsed Power Conference, Dallas, TX (2003), 1109.
- [Spelt87] J. K. Spelt, Y. Rotenberg, D. R. Absolom, and A. W. Neumann: *Sessile-drop contact angle measurements using axisymmetric drop shape analysis*, Colloids. Surf. **24**(2-3) (1987) 127–137.
- [Stoffels02] E. Stoffels, A. J. Flikweert, W. W. Stoffels, and G. M. W. Kroesen: *Plasma needle: a non-destructive atmospheric plasma source for fine surface treatment of (bio)materials*, Plasma Sources Sci. Technol. **11**(4) (2002) 383–388.
- [Stoffels06] E. Stoffels, I. E. Kieft, R. E. J. Sladek, L. J. M. van den Bedem, E. P. van der Laan, and M. Steinbuch: *Plasma needle for in vivo medical treatment: recent developments and perspectives*, Plasma Sources Sci. Technol. **15**(4) (2006) 169–180.
- [Stone04] J. A. Stone and A. Stejskal: *Using helium as a standard of refractive index: correcting errors in a gas refractometer*, Metrologia **41**(3) (2004) 189–197.
- [Strobel03] M. Strobel, V. Jones, C. S. Lyons, M. Ulsh, M. J. Kushner, R. Dorai, and M. C. Branch: *A Comparison of Corona-Treated and Flame-Treated Polypropylene Films*, Plasmas Polym. **V8**(1) (2003) 61–95.
- [Stützle06] R. Stützle: *Nicht zerfließende Wellenpakete in imaginären Potentialen*, Dissertation, Universität Heidelberg (2006).
- [Sun07] W.-T. Sun, T.-R. Liang, H.-B. Wang, H.-P. Li, and C.-Y. Bao: *The back-diffusion effect of air on the discharge characteristics of atmospheric-pressure radio-frequency glow discharges using*

- bare metal electrodes*, Plasma Sources Sci. Technol. **16**(2) (2007) 290–296.
- [Svanberg01] S. Svanberg: Atomic and Molecular Spectroscopy: Basic Aspects and Practical Applications, Springer-Verlag, Berlin/Heidelberg/New York, 3rd edn. (2001).
- [Tachibana05] K. Tachibana, Y. Kishimoto, and O. Sakai: *Measurement of metastable $He^*(2^3S_1)$ density in dielectric barrier discharges with two different configurations operating at around atmospheric pressure*, J. Appl. Phys. **97**(12) 123301/1–123301/7.
- [Takahashi98] K. Takahashi, N. Taniguchi, Y. Matsumi, M. Kawasaki, and M. N. R. Ashfold: *Wavelength and temperature dependence of the absolute $O(^1D)$ production yield from the 305–329 nm photodissociation of ozone*, J. Chem. Phys. **108**(17) (1998) 7161–7172.
- [Thomson99] M. Thomson: Nachweis von atomarem Wasserstoff mittels doppeltresonanter Vierwellenmischung, Dissertation, Universität GH Essen (1999).
- [Tosaka05] A. Tosaka, T. Nishiguchi, H. Nonaka, and S. Ichimura: *Low-temperature oxidation of silicon using UV-light-excited ozone*, Jpn. J. Appl. Phys. **44**(33–36) (2005) L1144–L1146.
- [Walsh00] K. T. Walsh, J. Fielding, and M. B. Long: *Effect of light-collection geometry on reconstruction errors in Abel inversions*, Opt. Lett. **25** (2000) 457–459.
- [Wang03] S. Wang, V. Schulz-von der Gathen, and H. F. Döbele: *Discharge comparison of nonequilibrium atmospheric pressure Ar/O₂ and He/O₂ plasma jets*, Appl. Phys. Lett. **83**(16) (2003) 3272–3274.
- [Wang07] H.-X. Wang, X. Chen, K. Cheng, and W. Pan: *Modeling study on the characteristics of laminar and turbulent argon plasma jets impinging normally upon a flat plate in ambient air*, Int. J. Heat Mass Transfer **50**(3–4) (2007) 734–745.
- [Wells99] R. J. Wells: *Rapid approximation to the Voigt/Faddeeva function and its derivatives*, J. Quant. Spectrosc. Radiat. Transfer **62**(1) (1999) 29–48.
- [White59] A. D. White: *New hollow cathode discharge*, J. Appl. Phys. **30** (1959) 711–719.
- [Yang05a] X. Yang, M. Moravej, G. R. Nowling, S. E. Babayan, J. Panelon, J. P. Chang, and R. F. Hicks: *Comparison of an atmospheric*

- pressure, radio-frequency discharge operating in the α and γ modes*, Plasma Sources Sci. Technol. **14**(2) (2005) 314–320.
- [Yang05b] X. Yang, M. Moravej, G. R. Nowling, J. P. Chang, and R. F. Hicks: *Operating modes of an atmospheric pressure radio frequency plasma*, IEEE Trans. Plasma Sci. **33**(2) (2005) 294–295.
- [Yonson06] S. Yonson, S. Coulombe, V. Léveillé, and R. L. Leask: *Cell treatment and surface functionalization using a miniature atmospheric pressure glow discharge plasma torch*, J. Phys. D: Appl. Phys. **39**(16) (2006) 3508–3513.
- [Young05] T. Young: *An Essay on the Cohesion of Fluids*, Phil. Trans. Roy. Soc., London **95** (1805) 65–87.

List of Publications

Parts of this work have already been published. The respective papers are marked with \diamond :

- „Optical Diagnostics on Micro Discharge Jets“, V. Schulz-von der Gathen, V. Buck, T. Gans, N. Knake, K. Niemi, S. Reuter, L. Schaper and J. Winter, in: *Contributions to Plasma Physics* Vol. 47 (2007) 510-519 \diamond
- „Diagnostics on an atmospheric pressure plasma jet“, K. Niemi, S. Reuter, L. Schaper, N. Knake, V. Schulz-von der Gathen, T. Gans, in: *Journal of Physics: Conference Series* Vol. 71 (2007) 012012/1-012021/9 \diamond
- „Correlation of Structural Properties of Commercial DLC Coatings to their Tribological Performance in Biomedical Applications“, S. Reuter, B. Weßkamp, R. Büscher, A. Fischer, B. Barden, F. Lör, V. Buck, in: *Wear* Vol. 261 (2006) 419-425
- „Structural and optical properties of BaTiO₃ thin films prepared by radio-frequency magnetron sputtering at various substrate temperatures“, Y. K. Vayunandana Reddy, D. Mergel, S. Reuter, V. Buck, M. Sulkowski, in: *Journal of Physics D, Applied Physics* Vol. 39 (2006) 1161-1168
- „Deposition of hard carbon coatings using combined inductively and capacitively coupled plasma sources“, G. F. Zhang, S. Reuter, V. Buck, in: *Surface and Coatings Technology* Vol. 190 (2005) 54-59
- Wer war Albert Einstein? – Eine fächerübergreifende Projektmappe zum Einsteinjahr 2005, S. Reuter, D. Sprick, Verlag an der Ruhr, 2005, ISBN 3-86072-990-X (Rezension siehe: Physik Journal 4(12) (2005))
- „Qualitätssicherung durch Schichtdickenmessung von Diamant- und diamantartigen Schichten“, B. Heimann, S. Reuter, F. Deuerler, V. Buck, in: *Galvanotechnik* Vol. 95 (2004) 994-1001

Contributions to Conferences (2006 - 2007)

- 60th Annual Gaseous Electronics Conference (GEC), Arlington, VA, 02.10.-05.10.2007
S. Reuter, V. Schulz-von der Gathen, H. F. Döbele: Atmospheric Pressure Plasma Jet (APPJ) and Homogeneous Dielectric Barrier Discharge (DBD) in Comparison (oral presentation) – *financial support by the DFG is gratefully acknowledged*
- XXVIII International Conference on Phenomena in Ionized Gases (ICPIG), Prag, 15.07.-20.07.2007 S. Reuter, K. Niemi, V. Schulz-von der Gathen, H. F. Döbele: Atomic Oxygen Density in the Effluent of an RF-Excited Atmospheric Pressure Plasma Jet: Measurements, Modelling, Mechanisms (poster presentation) – *the presentation was awarded the „Plasma Processes & Polymers Award – Best Student Poster Price“*
- 3rd International Congress on Cold Atmospheric Pressure Plasmas (CAPPSPA), Gent, 10.7.-13.7.2007 S. Reuter, K. Niemi, V. Schulz-von der Gathen, H. F. Döbele: The Atmospheric Pressure Plasma Jet as an Atomic Oxygen Source for Polymer Treatment (oral presentation)
- 13. Fachtagung Plasmatechnologie (PTXIII), Bochum, 05.03.-07.03.2007 S. Reuter, K. Niemi, V. Schulz-von der Gathen, H. F. Döbele: Der Atmosphärendruck Plasma Jet (APPJ), eine kalte Plasmaquelle für atomaren Sauerstoff (poster presentation)
- 9th Euregional Workshop on the Exploration of Low Temperature Plasma Physics (WELTPP), Kerkrade, 23.11.-24.11.2006 S. Reuter, K. Niemi, V. Schulz-von der Gathen, and H. F. Döbele: Absolute Oxygen Radical Densities in the Effluent of an Atmospheric Pressure Plasma Jet (oral presentation)
- 59th Annual Gaseous Electronics Conference (GEC), Columbus, OH, 10.10.-13.10.2006 S. Reuter, K. Niemi, V. Schulz-von der Gathen, and H. F. Döbele: Absolute Atomic Oxygen Density Measurements by Two-Photon Laser-induced Fluorescence (TALIF) Spectroscopy in the Effluent of an Atmospheric Pressure Plasma Jet (oral presentation) – *financial support by the GEC is gratefully acknowledged*
- DPG Frühjahrstagung 2006, Augsburg, 27.03.-30.03.2006 S. Reuter, K. Niemi, V. Schulz-von der Gathen, H. F. Döbele: Absolute Atomic Oxygen Density Measurements in the Effluent of an Atmospheric Pressure Plasma Jet (APPJ) by Two-Photon Laser-induced Fluorescence Spectroscopy (poster presentation) – *financial support by the „Wilhelm und Else Heraeus - Förderprogramm der DPG“ is gratefully acknowledged*

Danksagung

Diese Arbeit wäre ohne die Unterstützung vieler lieber Menschen nicht in dieser Weise möglich gewesen. Ihnen allen danke ich sehr. Im Folgenden möchte ich den Personen danken, die besonders zum Gelingen beigetragen haben:

- Ganz herzlich möchte ich meinem Doktorvater Prof. Dr. H. F. Döbele danken, insbesondere für die Bereitschaft, meine Arbeit auch aus dem Ruhestand heraus weiter zu betreuen. Seine Hilfestellungen physikalischer, inhaltlicher und auch sprachlicher Natur sind neben den Tipps fürs Leben eine bleibende Bereicherung. Ich bedanke mich vielmals auch für die immer umgehende Erstellung von Gutachten, die mir die Teilnahme an internationalen Tagungen ermöglichten. In der AG Döbele fühlte ich mich gut aufgehoben und bedaure, dass es sie nicht mehr gibt. Vielen Dank!
- Herrn Prof. Dr. V. Buck, der die Zweitkorrektur übernimmt, danke ich sehr für seine Förderung besonders auch im Vorfeld dieser Arbeit. Seine Unterstützung, insbesondere bei den umfangreichen Forderungen der Universität Essen für ein aufbauendes Diplom, war mir eine große Hilfe. Die Forschung in seiner Arbeitsgruppe ermöglichte mir breite Einblicke in die Plasmatechnologie, die mir auch nach dem Wechsel zur Plasmadiagnostik von großem Nutzen waren. Ich bedanke mich für viele interessante und hilfreiche Gespräche und die wertvolle Zeit in der AG Buck!
- Besonders möchte ich mich bei Dr. Volker Schulz-von der Gathen, der diese Arbeit von Anfang bis Ende betreut hat, bedanken, dafür, dass er auf Fragen zu jeder Zeit die Antwort weiß, für seine freundschaftliche Unterstützung im Labor durch sein hohes Fachwissen nicht nur auf dem Gebiet der Plasmadiagnostik, und nicht zuletzt dafür, dass er mir durch seine Mission die Welt von Linux eröffnet hat. Ich danke ihm für die erhellenden, nicht nur fachlichen Diskussionen, die er auch während und nach seinem beruflichen Umzug an die Ruhr-Universität Bochum mit mir geführt hat. – Volkers Gathenparties sind eine Insel der interuniversitären Kommunikation und des spannendsten Salatbuffets (ich freue mich auf nächsten Sommer)!
- Meinem Labornachbarn Dr. Kari Niemi danke ich sehr für seine immer richtigen Ratschläge, die umfassende Einführung in die TALIF-Spektroskopie und die Durchführung der Ozonmessungen an Luft. Ich denke gerne an die freundschaftliche Zusammenarbeit am sich manchmal als recht störrisch erweisenden APPJ. Auf Karis Fragen, die sich nicht selten als Antworten herausstellten, möchte ich auch in Zukunft nicht verzichten.

- Für die hilfreiche und ermunternde Unterstützung gegen Ende dieser Arbeit danke ich Herrn Dr. Michael Katsch, letzte Bastion der AG Döbele. Abgesehen von der unermüdlichen Suche nach freien Büros der Universität Essen, in denen ich mir einen Schreibtisch aufbauen durfte, danke ich ihm besonders für Diskussionen über die Modellrechnungen und sein aufmerksames Zuhören bei meinen Probenvorträgen. Dr. Timo Gans danke ich für seine wertvollen Hinweise, die dieser Arbeit mit zum guten Ende verholfen haben, für seine universitätsübergreifende Unterstützung und für alles Weitere.
- Meinen Mitstreitern, die es soweit haben kommen lassen, danke ich von ganzem Herzen: Nicolas Wöhrle, mit dem zusammen ich diesen einzigartigen Weg der zwei Diplome beschritten habe, für die langjährige tiefe Freundschaft. Unvergessen bleiben die Infrastrukturmaßnahmen im Keller und in der vierten Etage. Unsere nächtlichen Diskussionen bei einer Flasche Rotwein nach erfolgreichen Tagungen gehören mit zu den wichtigsten Momenten meines Studiums. Alex Wagner für die lockere und kreative Atmosphäre und die Hotline von Labor zu Labor. Ich bin froh über die Freundschaft und die unzähligen Debatten über Plasmadiagnostik, Plasmamodellierung, LyX und den Ernst des Lebens. Das Räumen des Labors und die Büro-Umzüge hätten ohne ihn keinen Spaß gemacht. Wir waren die letzten unserer Art.
- Den guten Seelen der AG Döbele: Carola Fischer für die Scotty-ähnliche Bewältigung jeder Aufgabe, Jürgen Leistikow, dem unverzichtbaren Fachmann für Elektronikfragen, dafür, dass er die Elektronen in meinen Experimenten in Schwung gebracht hat. Claudia Besecke für das Bezwingen jeder bürokratischen Hürde. Die Zuverlässigkeit und stete Hilfsbereitschaft, sowie das „einfach-mal-quatschen“, auch ‘nach’ der AG Döbele, haben mir so sehr geholfen.
- Den ehemaligen Mitarbeitern der AG Döbele und der AG Buck möchte ich für die gute und freundschaftliche Atmosphäre im Labor danken. Im Besonderen Dr. Mohamed Abdalla, Christian Amann, Markus Degenhard, Oleksiy Filipov, Dr. Anne Franzis, Irene Langner, Marcus Lartz, Dr. Thomas Mosbach.
- Ich danke den Mitarbeitern der mechanischen, feinmechanischen und optischen Werkstatt des Campus Essen für ihre hervorragende und schnelle Arbeit.

Ich danke allen meinen hier nicht genannten Freunden, auch dafür, dass ich ihnen immer wieder erklären durfte, was man eigentlich mit einem Plasmajet macht. Mein größter Dank gilt meinen Eltern Inge und Christian Reuter und meiner Freundin Diana Sprick für ihre Unterstützung jeder Art. Meine Eltern haben mit ihrem Vertrauen und nicht zuletzt durch ihre außergewöhnliche finanzielle Unterstützung diese Arbeit ermöglicht. Diana danke ich fürs intensive Korrekturlesen und dafür, dass man mit ihr auch am Ende noch so viel lachen kann.

